POLITECNICO DI MILANO

Scuola di Ingegneria Industriale e dell'Informazione

Corso di Laurea Magistrale in Ingegneria Energetica

Numerical analysis of a solar tower receiver tube operated with liquid metals

Relatore: Prof. Luca Davide MAROCCO

Tesi di Laurea di:

Giorgia CAMMI Matr. 801563

Anno Accademico 2014 - 2015

Politecnico di Milano:
www.polimi.it

Scuola di Ingegneria Industriale e dell'Informazione:
www.ingindinf.polimi.it

Acknowledgements
Ringraziamenti

Il primo e più grande ringraziamento va alla mia famiglia che mi ha sempre supportato e sopportato:

- a mia madre che mi ha sempre spronato a dare il meglio e a non gettare mai la spugna,
- a mio padre che mi ha insegnato a parlare soprattutto quando si ha qualcosa di intelligente da dire,
- a mio fratello che mi insegna ogni giorno a sdrammatizzare le difficoltà con una risata.

Un ringraziamento speciale va al mio relatore Luca Marocco. Grazie per avermi guidato ed aver creduto in me, spero che la nostra preziosa collaborazione possa continuare in futuro.

This thesis work would not be possible without the support of all the people at the KALLA labor. I want to thank professor Wetzel for the opportunity he gave me to work at KALLA for six months.

Infine un ringraziamento va a tutte quelle persone che hanno reso speciali gli ultimi cinque anni:

- a Marco che non ha mai smesso di amarmi neanche durante le peggiori sessioni di esame,
- a Barbara e Selene su cui posso sempre contare fin da quando ero nella culla,
- agli irriducibili della 5° scientifico A che sento sempre vicini anche quando sono sparsi per il mondo,
- a Federico che ormai è come un fratello maggiore,
- a Paolo prezioso compagno di studi e a tutti gli altri "colleghi" conosciuti al Politecnico che ormai sono amici di cui non potrò più fare a meno,
- a Antonio, Andrea e Francesca che più che coinquilini sono stati una seconda famiglia,
- ai colleghi ed ex-colleghi del Sottomura che hanno sempre reso fantastiche le mie estati, e anche i miei inverni,
- to Meli and Patric, without you maybe my thesis would be longer but my life would be emptier. Meli, I went to Germany and I found a Mexican sister, thank you for all.

Contents

Abstract

Lots of investments have been recently made in developing concentrating solar power systems (CSP) [1]. In particular central receiver power plants are expected to become soon competitive with respect to fossil-fuels ones [2].

In order to increase the power cycle efficiency of CSP plants, higher operating temperature and heat flux densities beyond state-of-the-art systems are needed. An important step towards this goal is the selection of an efficient heat transfer fluid, as it has a large effect on the overall performance.

Therefore, the development of new solar receiver concepts using liquid metals as heat transfer fluids is a promising way of reaching higher temperatures and lowering costs [3–5].

The heat flux applied on a receiver tube is circumferentially and longitudinally non-uniform. This creates doubts about the applicability of the available Nusselt correlations, in principle valid for uniform imposed heat fluxes, and it determines high thermal stresses in the tube walls. Thus, for a proper thermo-hydraulic, as well as mechanical design of the receiver, good knowledge of the local wall temperatures and convective heat transfer coefficients is required.

Computational fluid dynamics is then used in the present work to analyze the conjugate heat transfer in the receiver tube of a solar thermal tower operated with a liquid metal, to the purpose of comparing the numerical results with the Nusselt numbers provided by the available correlations for liquid metals.

The numerical analysis is complicated by the fact that the heat transfer mechanism of liquid metals differs from that of ordinary fluids. Consequently, the Reynolds analogy cannot be applied to these fluid flows.

The performances of different approaches of computing the turbulent heat flux have been evaluated by comparisons against DNS data, suitable Nusselt correlations and semi-analytical solutions provided in [6, 7].

A recently proposed four-equation turbulence model [8], considering the thermal turbulence effects and the dissimilarities between the thermal and dynamical turbulence fields has been selected to perform the numerical analysis.

Therefore, two additional equations, namely one for the temperature variance and one for its dissipation rate, have been solved, in order to determine the turbulent thermal diffusivity. The turbulence model has been implemented through User Defined Functions (UDFs) and coupled to the CFD code (Fluent v.15).

Simulations have been performed first for a circumferentially uneven and longitudinally uniform heat flux and then for the circumferentially and longitudinally non-uniform heat flux present on a central receiver tube. A parametric study has been done for different combinations of the governing parameters: wall thickness

ratio, solid-to-fluid thermal conductivity ratio, Peclet number, diameter-to-length ratio.

Detailed results for the inner, outer, fluid bulk temperature, Pr_t and Nusselt number have been reported. The calculated average Nusselt numbers closely agree with those evaluated with appropriate correlations for liquid metals, valid for uniformly distributed heat flux. Nonetheless, these correlations are not suited to evaluate the local Nusselt number and wall temperature distribution.

Keywords: Liquid Metals, CFD, Turbulent convection, Conjugate heat transfer, Pipe flow, Solar receiver, Non-uniform heat flux.

Sommario

Nel presente lavoro di tesi è illustrata l'analisi numerica dello scambio termico in un tubo di un ricevitore di una torre solare operato con metalli liquidi. Il flusso termico presente è fortemente non uniforme sia in direzione assiale che circonferenziale; questo comporta la presenza di alti stress termici e la necessità, in fase di progettazione, di disporre di stime accurate della temperatura a parete e del coefficiente di scambio termico. Lo scopo di questo lavoro è quindi quello di confrontare i risultati numerici ottenuti con le correlazioni disponibili per il calcolo di Nu nei metalli liquidi.

Il meccanismo di scambio termico dei metalli liquidi è peculiare e differisce da quello di altri fluidi comuni aventi Pr vicini o superiori all'unità. L'analogia di Reynolds non è valida per i metalli liquidi e, di conseguenza, diversi metodi per modellizzare il numero di Prandtl turbolento Pr_t sono stati utilizzati e confrontati in questa tesi. Un modello a quattro equazioni recentemente proposto in [8] e specificatamente calibrato per metalli liquidi è stato scelto per effettuare l'analisi numerica.

Le simulazioni svolte hanno considerato dapprima un flusso termico longitudinalmente costante e circonferenzialmente non uniforme e in seguito un flusso termico longitudinalmente e circonferenzialemnte non uniforme modellizzato al fine di riprodurre quello presente in un ricevitore di una torre solare.

Uno studio parametrico al variare di 4 parametri adimensionali ($\lambda*$, r^*, L/D, Pe) significativi è stato effettuato. I risultati in termini di temperature a parete sia esterna sia interna, temperatura di bulk, Pr_t, e Nu sia locali che globali sono diffusivamente presentati e commentati.

In paricolare si evince che il numero di Nusselt globale calcolato dalle simulazioni è in accordo con quello fornito da correlazioni appropriate per metalli liquidi valide per flussi termici uniformi; tuttavia, le stesse correlazioni, non sono utilizzabili per calcolare i profili di temperatura a parete o il Nu locale.

Parole Chiave: Metalli liquidi, CFD, Convezione turbulenta, Scambio termico coniugato, Ricevitore solare, Flusso termico non uniforme.

Riassunto esteso

Le centrali solari a concentrazione sono una tecnologia promettente per il futuro della generazione elettrica. Esse infatti sfruttano una delle fonti energetiche rinnovabili per eccellenza e, grazie alla possibilità di integrare un serbatoio termico, risolvono il problema dell'aleatorietà della fonte solare e i conseguenti problemi di dispacciamento. Per questi motivi gli investimenti volti a studiare, progettare e costruire nuove centrali solari a concetrazione sono esponenzialmente aumentati negli ultimi anni [1].

In particolare le torri solari a concentrazione sono la tecnologia più promettente in termini di prospettive di riduzione di costo dell'energia prodotta. Le proiezioni disponibili mostrano che esse possono diventare competitive rispetto alle centrali tradizionali in pochi anni [2].

Per aumentare l'efficienza delle centrali a torre solare e diminuire il costo dell'energia prodotta, è cruciale raggiungere temperature operative più alte e quindi avere flussi termici maggiori sul ricevitore [9]. La scelta del fluido di scambio termico influenza molto questi parametri e nuove configurazioni in cui il fluido di scambio termico impiegato è un metallo liquido sono attualmente allo studio con risultati promettenti [3–5].

Questa tesi è stata svolta presso il Laboratorio di Metalli Liquidi dell'Istituto per le Tecnologie Nucleari ed Energetiche del Karlsruhe Institute of Technology (Germania), dove un ricevitore solare operato con metalli liquidi con una potenza termica di $10\,kW$ è in costruzione. Lo scopo è quello di riacquisire esperienza nell'operare sistemi a concentrazione che adottano metalli liquidi come fluido di scambio termico, validare una metodologia di progettazione adottabile per centrali di grossa taglia e valutarne i costi.

In questo scenario si inserisce il presente lavoro di tesi che si propone di valuatre, attraverso simulazioni numeriche, l'applicabilità delle correlazioni per il numero di Nusselt in teoria valide solo per flussi termici imposti uniformi, a casi in cui il flusso termico sia non uniforme.

Il flusso termico a cui sono sottoposti i tubi che compongono un ricevitore di una torre solare è infatti fortemente non uniforme, sia in direzione tangenziale sia lungo la circonferenza. Questo provoca alti stress termici e la necessità, in fase di progettazione, di disporre di stime accurate della temperatura a parete e del coefficiente di scambio termico.

L'analisi numerica è complicata dal fatto che il meccanismo di scambio termico dei metalli liquidi è peculiare a causa del loro basso numero di Prandtl. Questo comporta la non validità dell'analogia di Reynolds e la non applicabilità dei consueti

metodi di modellizzazione del flusso termico turbolento utilizzati per i più comuni fluidi di scambio termico.

Diversi metodi per il calcolo del numero di Prandtl turbolento Pr_t sono quindi illustrati (Sez.3.1.2) e confrontati (Cap.4). Il confronto è stato effettuato utilizzando dati provenienti da simulazioni DNS[1], correlazioni e soluzioni semi-analitiche proposte in [6, 7] per un flusso completamente sviluppato sottoposto ad un flusso termico che varia cosinusodialmente lungo la circonferenza del tubo.

In particolare un modello a quattro equazioni recentemente proposto in [8] è stato poi scelto per effettuare l'analisi numerica vera e propria. La peculiarità di questo modello risiede nel fatto che tiene conto delle diverse scale temporali di turbolenza presenti nei fluidi a basso numero di Prandtl. Nei metalli liquidi infatti le scale di turbolenza relative alla quantità di moto differiscono sensibilmente da quelle relative all'energia termica (vedi Sez.2.2).

Oltre alle equazioni di trasporto per k ed ε due equazioni di trasporto aggiuntive, una per la varianza della temperatura k_θ, e una per il suo tasso di dissipazione ε_θ, sono state implementate tramite UDF[2]s, accoppiate con il codice FLUENT v.15 e quindi risolte per ottenere il valore di α_t in ogni simulazione.

In primo luogo sono state effettuate simulazioni, a diversi Pe, per un flusso completamente sviluppato sia dinamicamente sia termicamente sottoposto ad un flusso termico circonferenzialmente non uniforme. I risultati, in termini di profili di temperatura a parete e Nu, sono stati confrontati con quelli che si otterrebbero utilizzando una correlazione per Nu valida per metalli liquidi sottoposti ad un flusso termico uniforme consigliata in [15].

Dai risultati si evince che la correlazione (Eq.(4.1)) fornisce un stima del Nusselt globale in linea con il valore riscontrato nelle simulazioni, tuttavia i profili di temperatura a parete estrapolati analiticamente a partire dallo stesso Nu, differiscono sensibilmenete con quelli ottenuti nelle simulazioni numeriche (Sez.5.1).

Successivamente l'analisi completa dello scambio termico coniugato in un tubo di un ricevitore solare operato con metalli liquidi è stata effettuata. Sono state effettuate simulazioni per diversi valori dei parametri adimensionali che influenzano il problema (λ^*, r^*, L/D, Pe).

Il flusso termico applicato in questi casi è non uniforme sia circonferenzialmente sia logitudinalmente ed è stato modellizzato in modo da ricalcare quello realmente presente in un ricevitore di una torre solare (Sez.2.1).

Il fatto che il flusso termico vari lungo la direzione assiale impedisce il raggiungimento di una condizione di completo sviluppo dal punto di vista termico, almeno non con le implicazioni che si avrebbero nel caso di un flusso termico uniforme. I risultati ottenuti sono stati confrontati con una correlazione, in teoria valida solo per un flusso termico imposto uniforme, che tenesse conto della regione di sviluppo termico.

Grafici che mostrano l'andamento dei profili di temperatura di parete esterna e interna, temperatura di bulk, Pr_t e Nu sia locale che globale al variare dei parametri ($\lambda*$, r^*, L/D, Pe) si possono trovare in Sezione 5.2.2. Si può concludere che la correlazione scelta, nel range di variabilità dei parametri adimensionali

[1] Direct Numerical Simulation
[2] User Defined Functions

considerato, fornisce risultati in accordo con quelli delle simulazioni numeriche per quanto riguarda il Nu globale, mentre quello locale $Nu(x)$ differisce sensibilmente da quello stimato. Inoltre i valori di Nu globale calcolati si allontanano da quelli predetti dalla correlazione all'aumentare di Pe e di L/D.

In definitiva, è possibile affermare che le correlazioni consigliate per il calcolo del Nu globale per i metalli liquidi, in teoria valide per un flusso termico imposto uniforme, possono essere applicate in caso di flusso termico non uniforme, prestando però particolare attenzione nel caso in cui l'assenza di uniformità riguardi anche la direzione assiale. In ogni caso, tuttavia, i valori di temperatura a parete cos' come il Nusselt locale, non sono estrapolabili a partire dai coefficienti di scambio termico forniti dalle correlazioni.

Chapter 1

Introduction

1.1 Concentrating Solar Power

Figure 1.1: Sketch of a solar tower

The demand for a more balanced and sustainable energy mix is worldwide boosting the research in the solar energy field. Increasing the share of electrical energy coming from renewable sources means both to tackle the climate change problem and to reduce the energy dependence on fossil fuels. The second point is extremely important, especially for those countries that are importing fossil fuels, often from politically unstable regions. For these reasons, over the past decade, almost 80% of European investments in power generation went to renewables, especially to wind and solar technologies (`http://www.iea.org/`).

CSP[1] plant solutions are among the more promising power production technologies based on a renewable source. One of the reasons has to be found in the possibility to integrate a thermal storage, overcoming dispatchability issues affecting other solutions based on wind or sun power.

CSP plants are made by a solar collector field concentrating the solar radiation on a receiver. In the receiver a heat transfer fluid (HTF[2]) stores up the solar power as thermal energy. This energy can be transferred to a power conversion system or be stored in a thermal storage system.

CSP plants can be classified according to the way they focus the sun's rays. There are four big categories of CSP plants: parabolic trough, solar tower or central receiver, linear Fresnel and dish Stirling. Parabolic trough and linear Fresnel

[1] Concetrating Solar Power
[2] Heat Transfer Fluid

systems adopt linear collectors while dish Stirling and solar tower systems are based on point focus collectors. The main difference is that linear collectors are single-axis tracking while point focus collectors are two-axis tracking. Parabolic trough and dish Stirling systems adopt a continuous system of concentration while linear Fresnel and solar tower systems are based on a discrete one. Continuous concentrators are mirrors in the form of a parabola, which reflect the solar energy at the focus of the parabola. The parabolic shape is made by a rigid metallic structure. Discrete concentration is achieved by several mirrors, which move independently in order to collect the solar energy at the same focus point. A more detailed description of CSP systems can be found in [10].

An important parameter to consider when it comes to characterize CSP systems is the concentration ratio.

$$CR = \frac{AbsorberArea}{ApertureArea} = \frac{A_a}{A_p} \tag{1.1}$$

In equation (1.1) A_a is proportional to the surface of the mirrors while A_p is proportional to the surface of the receiver. The highest CR is reached in solar tower systems where hundreds of mirrors concentrate the solar radiation on a single central receiver (Fig.1.2).

Analyzing the future potentialities of the previous mentioned CSP technologies, according to [2], on one hand, parabolic troughs technology is the most mature and shows the lowest development risk. On the other hand, solar towers power plants are the most promising in terms of reducing their capital costs and improving their performances.

1.2 Solar tower technologies

1.2.1 Components and operation

In a solar tower system, there are four macro-components:

- **The heliostat field**, consisting in several two axis tracking mirrors ground based that reflect the solar radiation onto a receiver located at the top of a tower (Fig.1.1).

- **The receiver**, absorbing the solar radiation and transforming it into thermal energy. There are several kinds of receivers and a good review of current researches on receiver concepts can be found in [1]. A heat transfer fluid HTF flow in the receiver, it can be gaseous, liquid and even concepts with solid particles directly absorbing the radiation are under evaluation.

- **The power block**, converting thermal energy in to electricity. Usually a Rankine Cycle is adopted; however concepts adopting close or open Brayton cycles and combined cycles are currently under research. The fluid performing the thermodynamic cycle is called working fluid (WF[3]).

[3]Working Fluid

- **The thermal storage**, storing part of the thermal energy coming from the receiver. This energy can be used to compensate the drop of solar energy due to passing clouds or, accordingly to the size of the storage, even to produce electricity at night. Thermal energy can be stored as sensible heat using liquids or solids, as latent heat using phase-change materials and as chemical energy. Sensible thermal energy storage using liquids represent the mature technology, the fluids adopted are called thermal storage fluids (TSF[4]s).

Depending on the HTF and its integration with the thermal storage system and the power block, different configurations are possible. In Fig.1.3 three possible configurations of central receiver power plants are illustrated.

Most of the solar tower power plants currently in operation adopt the configuration B; they are operated with molten salt both as HTF and as TSF. The power block is usually a Rankine water-steam cycle so water is the WF.

Configuration A involves a direct steam generation, it is a technology still in the concept phase but it aims at reducing costs and enhancing the thermal efficiency by eliminating one heat exchanger.

Configuration C has two different fluids for the heat transfer and for the thermal storage, this configuration is useful when the HTF is expensive or has a low specific thermal capacity (c_p).

Since 1980 there have been several pilot projects proving the feasibility and the economic potential of central receiver technologies. One good example is Gemasolar power plant located in Spain. It is a 20 MWe central receiver power plant operated with molten salt. It adopts configuration B and, thanks to its 15 hours storage system, it is able to deliver power around the clock (`http://www.torresolenergy.com/TORRESOL/gemasolar-plant/en`). Alongside with this project many others, already in operation or under construction, are moving forward the maturity of this technology. A lot of investments have been carried on lately on solar tower systems; in USA 1.2 GW power installation are under construction and worldwide 10.135 GW power installation are announced mainly in USA, Spain and China [1].

1.2.2 Potential

The raising interest in central receiver technologies is due mainly to the fact that the levelised cost of energy (LCOE[5]) of these power plants is supposed to lower in few years, making them competitive with traditional power plants [2] .

The reason is mainly that central receivers arrangements lead to higher concentration ratios than other CSP technologies. A higher number of sun rays are concentrated on a smaller surface so higher temperatures can be reached (see Fig. 1.2). From the thermodynamic point of view this feature is crucial since the efficiency of the thermodynamic cycle, used in the power block, is highly dependent on the maximum reachable temperature.

In fact, the overall ideal conversion efficiency of a CSP plant can be seen as:

$$\eta_{CSP} = \eta_{th}\eta_{cycle} \tag{1.2}$$

[4]Thermal Storage Fluid
[5]Levelised Cost of Energy

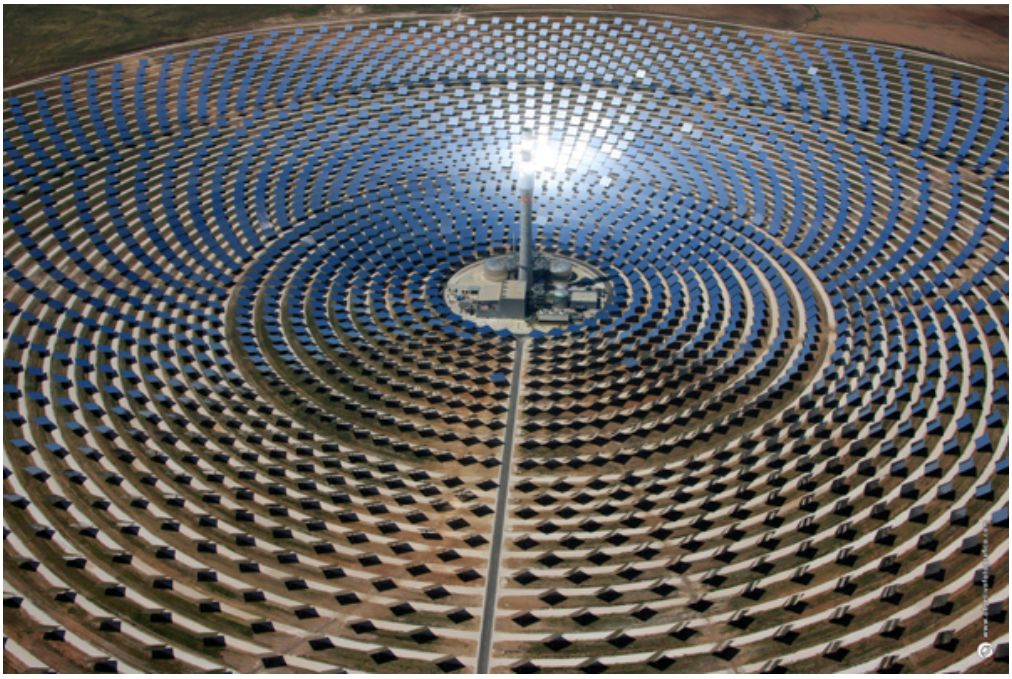

Figure 1.2: Photo of Gemasolar power plant (figure taken from `http://www.torresolenergy.com/TORRESOL/gemasolar-plant/en`)

In equation (1.2) η_{cycle} is the efficiency of the thermodynamic cycle adopted in the power block. It is directly dependent on the higher temperature reachable within the power block T_{max}. In fact, $\eta_{carnot} = 1 - \frac{T_{amb}}{T_{max}}$ and η_{cycle} is always a fraction of η_{carnot}.

Higher temperatures mean also more compact heat storage systems. However reaching higher temperature affects also the other components of the system. In equation (1.2) η_{th} represents the ratio between the net heat absorbed by the receiver and the energy concentrated on the receiver itself. Thus, η_{th} is affected by the thermal losses at the receiver surface. Radiative and convective heat losses increase with the surface temperature of the receiver and decrease with its area. Moreover, the surface temperature reached and the area required are themselves dependent on the HTF properties.

Thus reaching higher temperatures does not necessarily mean higher efficiencies, to exploit this potential the whole system has to be designed accordingly. Solar tower power plants are complex systems. Their design is highly dependent on the thermodynamic cycle used (Brayton, Rankine), on the receiver specifications and on the heat transfers fluid properties. Despite this complexity some fixed point can be derived from [1, 2, 4, 9, 11, 12].

First, the winning configuration among all the possible solar tower systems is not yet defined. Both from the technical and the economical point of view further researches are required. In this context, operating pilot power plants is important in order to gain operation experience, validate design methodologies, evaluate costs and test production capacities.

Second, even though efforts are required in order to make central receiver technology mature enough to compete on the market, there are encouraging forecasts

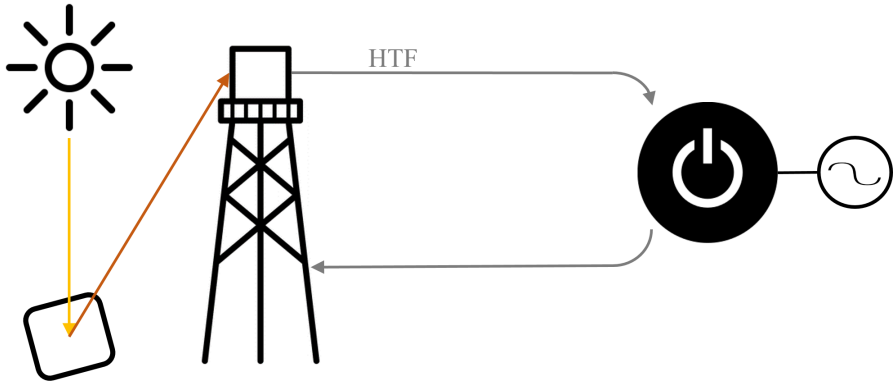

(a) *Configuration A.*

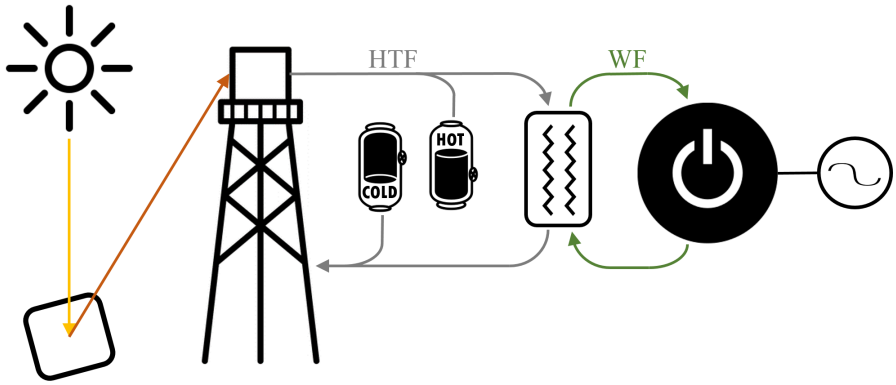

(b) *Configuration B.*

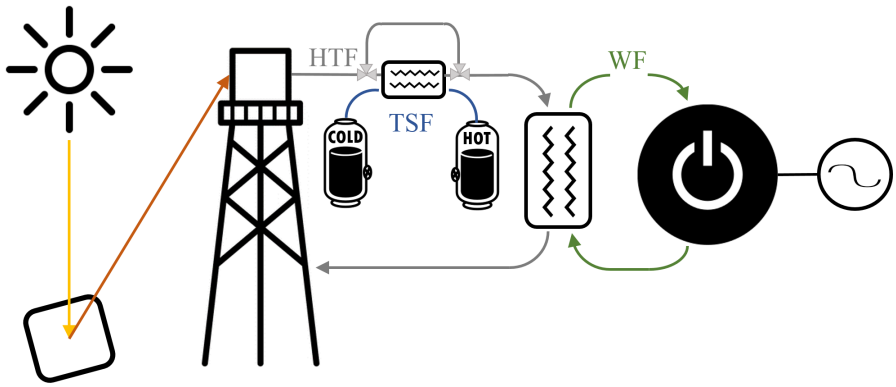

(c) *Configuration C.*

Figure 1.3: Examples of possible solar tower power plant configurations

about the LCOE. In [2] some projections are presented stating that the LCOE of solar tower power plants will decline by between 30% and 50% by 2020. In particular new solar tower concepts reaching higher temperatures and adopting ultra-supercritical steam cycles (USC[6]) are supposed to reach higher efficiencies and lower the LCOE.

In conclusion, despite the fact that efficiency and costs are affected by multiple design choices, future researches must focus on central receiver concepts adopting thermodynamic cycles with and increased T_{max}.

1.2.3 Heat transfer fluid selection

The selection of the HTF is crucial in designing a solar tower system. The perfect HTF has to fulfill several requirements:

- *Low melting point*, because during nights and cloudy cold days freezing should be avoided.
- *High upper temperature limit*, in order to reach higher T_{max}. The upper temperature limit can be set by the boiling point or by the point where the fluid loses its chemical stability and starts to degrade.
- *Large thermal conductivity* $\lambda\,[W/mK]$, which leads to a more efficient heat transfer.
- *Low viscosity* $\mu\,[kg/ms]$, in order to limit the pressure drop.
- *Large specific heat capacity* $c_p\,[J/kgK]$, which allows the introduction of a direct thermal storage where the HTF is also the TSF.
- *Low cost*
- *Non-polluting and non-flammable*, which means that small leakages do not affect the surrounding environment and the integrity of the power plant.
- *Easy to operate*, which is related to its compatibility with other materials in term of corrosion.

The solar tower power plants currently in operation adopt mainly molten salts (Hitec[7]) both as HTF and as TSF. However molten salts show some disadvantages; their upper temperature limit is about $600°C$ and their melting point is high (around $200°C$). The chemical instability of molten salt beyond $600°C$ sets a limit for T_{max} and it prevents them from being adopted in central receiver systems that exploit USC cycles.

In order to overcome these limits and increase T_{max}, different HTF have been proposed and a promising solution seems to be the adoption of liquid metals. Liquid metals present large thermal conductivity λ, small kinematic viscosity ν and a wide temperature range over which they remain in the liquid phase. They are efficient heat transfer media in processes with limited heat exchange surfaces and high thermal loads. For these reasons they were proposed as high temperature heat transfer media in CSP systems in 1980's. Tests were carried out on a demonstration plant (Plataforma Solar de Almeria) operated with a liquid sodium-cooled central receiver [13]. Experiments were stopped after a fire caused by a sodium leakage during improper maintenance works.

[6] Ultrasupercritical Steam Cycles
[7] Trade name of a ternary molten salt

Later, liquid metals have been widely exploited as HTF in fast fission nuclear reactors so now the operational experience in exploiting liquid metals in complex systems is much more solid than in the 1980's. The potentialities of liquid metals as HTF in central receiver systems have been assessed, indeed, in several recent researches.

In [9] different solar tower power plant adopting a tubular central receiver and driving USC cycles are compared. The figure of merit is the LCOE and the alternatives differ because of the HTF adopted. The analyzed HTFs are a molten nitrate salt eutectic and several liquid metals; tin, sodium, LBE[8] and LiCl-KCl eutectic. Parameters characterizing the central receiver are optimized considering the physical and thermodynamic properties of the different HTFs. The reference case considered is a $50 MW_{el}$ molten salt solar tower power plant with an 8 hours heat storage adopting configuration B shown in Fig. 1.3. The configurations compared are type B or C depending on the characteristic in term of price and c_p of the HTF. Results show a significant LCOE reduction potential of about 15% if an USC steam cycle and a tubular receiver operated with liquid metals with an optimum storage size are assumed.

Reaching higher temperatures is crucial and in order to achieve this goal a proper HTF has to be chosen. According to [4, 9, 11, 12] liquid metals, in particular sodium (Na) and LBE, are very promising options.

1.3 Scope and content

Given this scenario of increased interest in CSP technologies and the potentialities of solar tower power plants, the Karlsruhe Institute of Technology (KIT) in collaboration with the Solar Institute of the German Aerospace Center (DLR) have launched a project whose goals are planning, designing, constructing and operating a small CSP system in the $10\,kW$ thermal range using liquid metals as HTF [5].

The project involves the KALLA[9] team of the Institute for Nuclear and Energy Technologies IKET[10]. The facility has been named SOMMER[11] and the purposes of its operation are gaining operation experience, validating a design methodology for bigger plants and evaluating O&M costs and LCOE for solar tower concepts with increased T_{max}.

The central receiver is a key component and accounts for about 15 % of the total investment costs [14]. Therefore its design is crucial in order to reach good operational and economic performances.

Because of the extremely high concentration ratio that characterizes a CSP system adopting a central receiver configuration, the receiver undergoes severe thermal stresses. In order to optimize its size and to guarantee operational safety and long-lasting high performances, heat transfer coefficients and temperature profiles have to be carefully foreseen during the design phase.

Moreover, the more T_{max} increases the more a wrong prediction of local Nusselt

[8] Lead-Bismut (Pb- Bi) Eutectic
[9] KArlsruhe Liquid Metal Laboratory
[10] Institute for Nuclear and Energy Technologies
[11] SOlar Molten MEtal Receiver

numbers and wall temperatures can result in unexpected thermal stresses mining the structural integrity of the receiver.

The design of a central receiver operated with liquid metals is complicated by the extremely non-uniform boundary conditions present and by the peculiar heat transfer mechanism of the HTF chosen.

Common Nusselt correlations, such as the Dittus-Boelter correlation or the Gnielinsky correlation, widely used to compute Nusselt numbers in pipe geometries are not suitable when liquid metals are involved.

A review of Nusselt correlations suitable for liquid metals can be found in [15]. Nevertheless, all the correlations suggested in [15] consider the heat transfer occurring in a pipe undergoing a uniform thermal boundary condition (i.e. constant imposed heat flux) and their applicability to the case of a central receiver tube, undergoing an extremely non-uniform heat flux, is questionable.

The goals of this work are then:

- to assess whether the available Nusselt correlations for liquid metals, valid in principle for a uniformly distributed heat flux, can be applied in order to evaluate the heat transfer coefficients in a solar receiver tube;
- to define the governing parameters influencing the conjugate heat transfer problem of a solar receiver tube and assess their influence on the most important physical values (e.g. wall temperature profiles).

This will give also useful insights for the design of SOMMER.

The present work is organized as following.

In Chapter 2 the boundary conditions present on a solar receiver tube are presented and modeled and a description of the heat transfer mechanism of liquid metals is given.

The numerical approach adopted is presented in Chapter 3 together with the turbulence models used. Because of the peculiar heat transfer mechanism of liquid metals different approaches for computing the turbulent heat flux are presented (Sec.3.1.2) and assessed.

In particular a recently proposed four equation k-ε-k_θ-ε_θ turbulence model specifically calibrated for liquid metals has been implemented through UDFs. The implementation is validated in Sec.4.1.1. Moreover in Chapter 4 the performances of the different thermal turbulence models presented in Sec.3.1.2 are evaluated by comparisons with DNS data, suitable Nusselt correlations and semi-analytical solutions found in [6, 7].

Finally in chapter 5 results from simulations first for a circumferentially uneven and longitudinally uniform heat flux and then for the circumferentially and longitudinally non-uniform heat flux present on a central receiver tube are presented. A parametric study has been done for different combinations of the governing parameters: wall thickness ratio, solid-to-fluid thermal conductivity ratio, Peclét number, diameter-to-length ratio and detailed results for the inner, outer, fluid bulk temperature, Pr_t and Nusselt number are reported.

Chapter 2

Problem Description

2.1 The receiver and its boundary conditions

Even though, as explained in section 1.2.1, several receiver concepts are under research, the most used and proven is the external tube receiver. It is based on arrays of parallel tubes, which are cooled from the inside by the HTF and heated from the outside by the concentrated sunlight. The tubes are arranged in order to form a cylinder, a good example is shown in Fig.2.1a . Adopting this design, only half of the surface of the tubes is exposed to solar irradiance, while the other half, facing the inside of the receiver, can be considered as insulated.

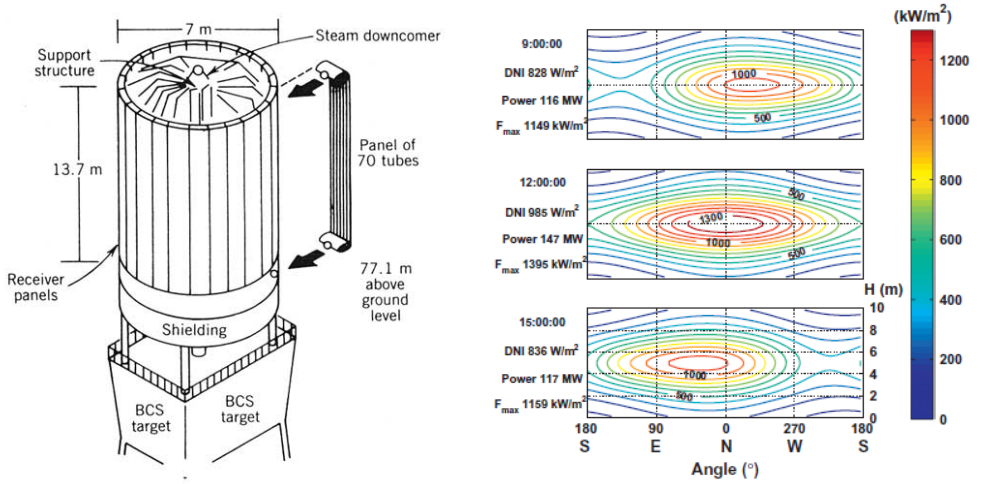

(a) *Sketch of the external tube receiver of Solar One power plant (figure taken from* `http://www.powerfromthesun.net/Book/chapter10/chapter10.html` *).*

(b) *Gemasolar-like heat flux distribution on the receiver on* 20^{th} *March (figure taken from [16]).*

Figure 2.1: Example of an external tubular receiver and the heat flux on it

The concentration of sun rays on the receiver is not uniform. Every mirror in the heliostat field is designed in order to track the sun and reflect the direct radiation on a target point located on the receiver itself. This process is affected by several losses such as shadowing, cosine, reflectivity, cleanliness, blocking, atmospheric and

spillage losses. Assessing these losses and predicting the heat flux distribution on the receiver is not the purpose of the present work. What is important to know is that the resulting heat flux is non uniform and it can be modeled as a circular Gaussian distribution over the entire receiver area.

Examples of heat flux distributions on a central tubular receiver can be found in [16]. In Fig.2.1b is shown the heat flux distribution on the receiver surface computed with a model reproducing the radiation reflected by the heliostat field of Gemasolar power plant on the 20^{th} of March.

Since the tubes are arranged in a parallel configuration, the boundary conditions are the same on each tube. Thus, within the present work, just one of the several parallel tubes is considered. The imposed heat flux on the surface of a single tube can be modeled as following:

- *Longitudinally* the heat flux follow a Gaussian law having its peak in the middle of the tube length (Fig.2.2) ;
- *Circumferentially* half of the tube perimeter is considered as insulated while on the other half the heat flux can be modeled with a sinusoidal distribution (Fig.2.2).

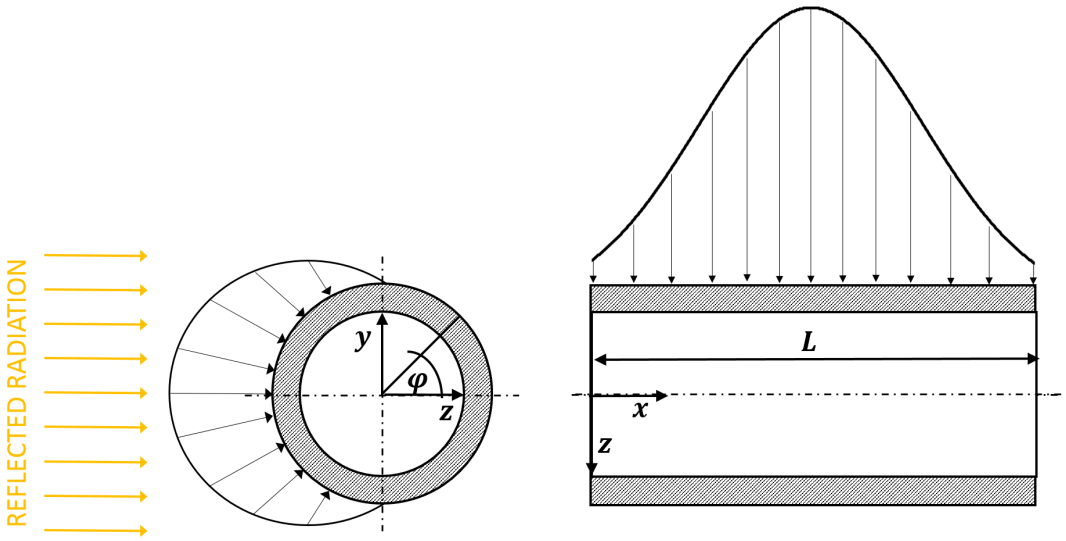

Figure 2.2: Heat flux variability over the length and the axial coordinate of the tube.

The hat flux variability over the axial coordinate is a direct consequence of the central Gaussian distribution of the heat flux over the receiver surface (Fig. 2.1b). On the other hand, to model the heat flux variability over the perimeter of the tube, the reflected radiation is considered constant with y and composed of perfectly parallel beams, as shown in Fig.2.2 .

Actually, it is a simplification since the beams are not perfectly parallel, because of the disposition of the heliostats, and the radiation is not constant, because of the Gaussian distribution. However, since the tube diameter is small if compared to the receiver diameter (a plausible ratio could be $D_{rec}/D_{tube} \geq 500$), the assumption of the reflected radiation being constant and perpendicular to y is valid.

Nonetheless, since the surface of the tube is curved, the cosine effect causes a variability of the heat flux over the tube circumference. The cosine effect consists in the reduction of radiation by the cosine of the angle between solar radiation and a surface normal. In Fig.2.2 is shown that the reflected radiation is normal to the surface of the tube only in $\varphi = 180°$. Thus, when $\varphi \neq 180°$ the cosine effect intervenes and the resulting heat flux distribution is sinusoidally varying (Fig.2.2).

In conclusion, the heat flux distribution presents on the external surface of a tube in a tubular central receiver can be modeled through (2.1).

$$\begin{cases} q''(\tilde{x},\varphi) = -q''_{max} \cdot \cos(\varphi) \cdot f(\tilde{x}) & \text{if} \quad 90° \leq \varphi \leq 270° \\ q''(\tilde{x},\varphi) = 0 & \text{if} \quad 0° \leq \varphi \leq 90° \wedge 270° \leq \varphi \leq 360° \end{cases} \tag{2.1}$$

$$f(\tilde{x}) = \exp\left[-\frac{1}{2}\left(\frac{\tilde{x}L - \mu}{\sigma}\right)^2\right] \tag{2.2}$$

$$\mu = L/2 \tag{2.3}$$

$$\sigma = L/5 \tag{2.4}$$

$$\tilde{\tilde{x}} = x/L \tag{2.5}$$

In the equations above L is the pipe length so $\tilde{x}$ is the non-dimensional axial coordinate. The term $f(\tilde{x})$ reproduces the Gaussian variability of the heat flux over the pipe length while the term $\cos(\varphi)$ accounts for the cosine effect. The factor q''_{max} is the maximum value of the heat flux reached in $\varphi = 180°$ and $\tilde{x} = 0.5$.

The resulting heat flux distribution keeps the same form independently from the pipe length and the q''_{max} chosen. The values at both ends are always 5 % of the maximum at the center; this because usually central receivers dimensions are designed in order to catch 90 % of the reflected radiation and this leads to the fact that, at the pipe ends, the heat flux assumes a value near to 5 % of q''_{max}. The non-dimensional profile of the heat flux is shown in Fig. 2.3a.

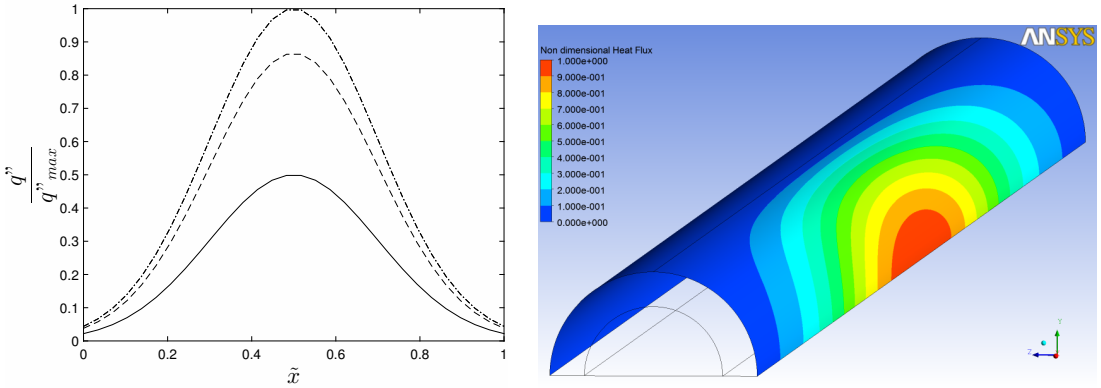

(a) *Non-dimensional profile of the heat flux. At $\varphi = 120°$ (solid line), $\varphi = 150°$ (dashed line),$\varphi = 150°$ (dot-dashed line) .*

(b) *Contour of the heat flux imposed computing the simulations presented in Sec.5.2.2.*

Figure 2.3: Heat flux on a central receiver tube

Table 2.1: Properties of Mercury, Air and Water at $20°C$

		Mercury	Air	Water
ρ	kg/m^3	13 579	1,205	998,3
c_p	kJ/kgK	0,139	1,005	4,183
λ	W/mK	8,69	0,026	0,598
ν	$(m^2/s) \cdot 10^{-6}$	0,114	15,11	1,004
Pr		0,0249	0,71	7,02

The thermal boundary conditions presented within this section have been applied to the numerical cases analyzed in Sec.5.2.2 through an UDF (Appendix A Listing A.1). In Fig.2.3b a contour of the imposed heat flux is shown.

In conclusion, the thermal boundary conditions present on a tube in a solar receiver are circumferentially and longitudinally uneven. This creates doubts about the applicability of correlations developed for uniformly heated tubes.

Moreover, the high unevenness of the heat flux can result in high thermal stresses in the tube walls, whose magnitude depends on the cooling effect of the heat transfer fluid. Thus, for a proper thermo-hydraulic design, as well as mechanical design of the receiver, good knowledge of the local wall temperatures and convective heat transfer coefficients is required.

2.2 Heat transfer mechanism of liquid metals

Liquid metals differ from the other heat transfer media because of their extremely high thermal conductivity ($\lambda\,[W/mK]$) and their lower specific heat capacity ($c_p\,[J/kgK]$). On one hand, their first peculiarity assures higher heat transfer coefficients and makes liquid metals appealing high efficient heat transfer media.

On the other hand, their low specific heat capacity, prevents them from being adopted as TSF. Thus, a solar tower power plant adopting liquid metals as HTF cannot adopt configuration B, configuration C is more suitable (see Fig.1.3). Actually there are exceptions, sodium has a specific heat capacity that is equal to that of other HTFs such as molten salt, and direct storage concepts are feasible if sodium is the HTF.

In table 2.1 properties of mercury, air and water are reported, mercury has been chosen as representative of liquid metals because the table refers properties at $20°C$ and mercury is liquid at that temperature. The table shows that the peculiarities of liquid metals affect their Prandtl number, which is much lower than that of water or air. The extremely low Prandtl number is a characteristic encompassing all liquid metals. They belong to the so-called category of low-Prandtl number fluids, (for a more comprehensive description of low-Prandtl number fluids thermal hydraulics see [17]).

$$Pr = \frac{c_p \cdot \mu}{\lambda} = \frac{\nu}{\alpha} \tag{2.6}$$

The Prandlt number is a non-dimensional parameter, Eq.(2.6), it is the ratio

between the momentum diffusivity and the thermal diffusivity. It appears in the non-dimensional form of the energy equation.

The energy equation is one of the conservation equations together with the continuity equation and the momentum equation. The conservation equations are the basis of fluid dynamics since they model the behavior of fluids resolving the flow and the temperature fields.

Liquid metals are Newtonian fluids that can be considered incompressible, supposing their properties constant with the temperature, their conservation equations take the form (2.7), (2.8), (2.9). They can be non-dimensionalized as (2.11), (2.12), (2.13), where * indicates non-dimensional quantities obtained using a characteristic length, velocity and temperature.

In these equations Φ^* is the dissipation functions that accounts for the dissipation due to shear stresses. Ec is the Eckert number, it is the ratio between the flow kinetic energy and enthalpy. It is quite small for incompressible fluids like liquid metals.

$$\vec{\nabla} \cdot \vec{U} = 0 \tag{2.7}$$

$$\frac{D\vec{U}}{Dt} = \vec{f} - \frac{1}{\rho}\vec{\nabla}p + \nu\nabla^2\vec{U} \tag{2.8}$$

$$\rho c_p \frac{DT}{Dt} = \lambda\nabla^2 T + \mu\Phi \tag{2.9}$$

$$\tag{2.10}$$

$$\Phi = 2\left[\left(\frac{\partial u}{\partial x}\right)^2 + \left(\frac{\partial v}{\partial y}\right)^2 + \left(\frac{\partial w}{\partial z}\right)^2\right] + \left(\frac{\partial v}{\partial x} + \frac{\partial u}{\partial y}\right)^2 + \left(\frac{\partial w}{\partial y} + \frac{\partial v}{\partial z}\right)^2 + \left(\frac{\partial u}{\partial z} + \frac{\partial w}{\partial x}\right)^2$$

$$\vec{\nabla}^* \cdot \vec{U}^* = 0 \tag{2.11}$$

$$\frac{D\vec{U}^*}{Dt} = -\vec{\nabla}^* p^* + \frac{1}{Re}\nabla^{*\,2}\vec{U}^* \tag{2.12}$$

$$\frac{DT^*}{Dt} = \frac{1}{RePr}\nabla^{*\,2}T^* + \frac{Ec}{Re}\Phi^* \tag{2.13}$$

$$\tag{2.14}$$

Looking at the non-dimensional form of the conservation equations it is clear that, if the pressure gradients and the Eckert number are negligible, the momentum equation and the energy equation assume the same form except for the presence of the Prandtl number. If $Pr = 1$ then the solutions for the dimensionless velocity and temperature fields are similar.

If a flow over a flat plate is considered, the boundary layer thicknesses of velocity and temperature are almost the same when the Prandtl number is close to unity. On the other hand, if $Pr << 1$, as for liquid metals, temperature and velocity profiles differ considerably and the thermal boundary layer thickness is much greater than the velocity boundary layer thickness (See Fig.2.4).

The dissimilarities existing between dimensionless profile of velocity and temperature in low-Prandtl number fluids point out that their heat transfer mechanism

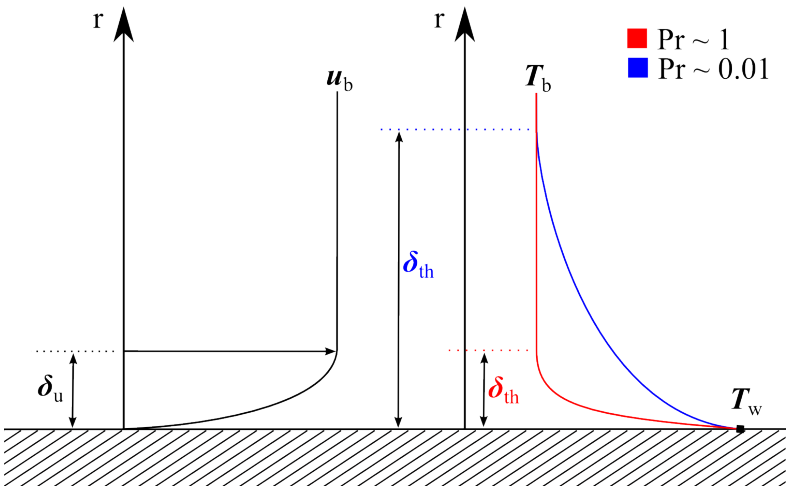

Figure 2.4: Comparison between velocity and temperature boundary layers at different Pr numbers

differs from that of other common HTF, as water or air. The most important consequence is that the turbulent momentum exchange and the turbulent heat transfer are not similar and the Reynolds analogy does not hold any more.

2.2.1 The Reynolds analogy

The goal of any CFD analysis is that of solving the conservation equations in order to obtain the flow and the temperature fields. These equations present non-linear terms and solving them analytically is possible only in few cases under strong hypothesis.

Thus, CFD analysis are based on numerical solutions of the conservation equations. In order to obtain a numerical solution time and space must be discretized, a time step must be chosen and a mesh of the geometry is needed.

Unfortunately, if the flow is turbulent, as it is in a solar receiver tube, the time step and the spatial discretization required, in order to obtain a reliable numerical solution, are extremely small. Turbulent flows are characterized by the presence of rotational flow structures called turbulent eddies. These eddies makes the flow unsteady with high frequency fluctuations of the flow properties.

The time step must be smaller enough to catch these fluctuations and the spatial discretization fine enough to resolve the smallest eddy. These scales of time and space are called Kolmogorov microscales and their order of magnitude is inversely proportional to the Re number. Turbulent flows are characterized by high Reynolds numbers so extremely fine spatial and time discretizations are required. This implies a too high computational effort.

To overcome this problem the conservation equations are not solved in their original form. The CFD analysis performed within this work follows the so-called RANS[1] approach. Averaged conservation equations are solved. These equations are derived from (2.7), (2.8), (2.9) by decomposing the flow properties in to a mean

[1]Reynolds Averaged Navier Stokes

value and a fluctuation (Eq. (2.15)). Afterwards a time average of the conservation equations is performed and the results take the form (2.16), (2.17), (2.18).

$$\varphi(\vec{x},t) = \overline{\Phi}(\vec{x}) + \varphi'(\vec{x},t) \tag{2.15}$$
$$\overline{\Phi}(\vec{x}) = \frac{1}{\Delta t}\int_t^{t+\Delta t} \varphi(\vec{x},t)$$

$$\frac{\partial \overline{U}_i}{\partial x_i} = 0 \tag{2.16}$$

$$\frac{\partial \overline{U}_i}{\partial t} + \overline{U}_j \frac{\partial \overline{U}_i}{\partial x_j} = -\frac{1}{\rho}\frac{\partial \overline{p}}{\partial x_i} + \frac{\partial}{\partial x_j}\left(\nu \frac{\partial \overline{U}_i}{\partial x_j} - \overline{u_i' u_j'}\right) \tag{2.17}$$

$$\frac{\partial \overline{T}}{\partial t} + \overline{U_i}\frac{\partial \overline{T}}{\partial x_i} = \frac{\partial}{\partial x_j}\left(\alpha \frac{\partial \overline{T}}{\partial x_j} - \overline{u_j' T'}\right) \tag{2.18}$$

The averaged conservation equations can be solved using much coarser time and spatial discretization, because they refer to the properties of the mean flow. Nevertheless, new unknown terms appear. They are the turbulent stresses or Reynolds stresses (Eq.(2.19)) and the turbulent heat flux (Eq.(2.20)).

$$\tau_{ij}^t = -\rho\, \overline{u_i' u_j'} \tag{2.19}$$
$$q_t'' = -\rho\, c_p\, \overline{u_j' T'} \tag{2.20}$$

Turbulence models are necessary in order to compute these unknown terms and make possible the numerical solution of the conservation equations. Many turbulence models, including the ones used within this work, compute the turbulent stresses and heat flux through the Boussinesq hypothesis

The Boussinesq hypothesis states that the turbulent stresses are proportional to the mean rates of deformation and the turbulent heat flux is proportional to the gradient of the mean temperature (See Eq.(2.21), (2.22)). The constants of proportionality are the turbulent viscosity μ_t and the turbulent thermal diffusivity α_t; they are the unknown quantities that are computed by turbulence models.

$$\frac{\tau_{ij}}{\rho} = \nu\left(\frac{\partial \overline{U}_i}{\partial x_j} + \frac{\partial \overline{U}_j}{\partial x_i}\right) \quad \longrightarrow \quad \frac{\tau_{ij}^t}{\rho} = \nu_t\left(\frac{\partial \overline{U}_i}{\partial x_j} + \frac{\partial \overline{U}_j}{\partial x_i}\right) - \frac{2}{3}k\delta_{ij} \tag{2.21}$$

$$\frac{q_j''}{\rho\, c_p} = \alpha \frac{\partial \overline{T}}{\partial x_j} \quad \longrightarrow \quad \frac{q_{j\,t}''}{\rho\, c_p} = \alpha_t \frac{\partial \overline{T}}{\partial x_j} \tag{2.22}$$

A comprehensive explanation of the turbulence models used within this work and their methods of computing the turbulent viscosity μ_t and the turbulent thermal diffusivity α_t is given in the following Chapter.

The Reynolds analogy states that $\nu_t = \alpha_t$. A turbulent Prandtl number can be defined as (2.23) . The turbulent Prandtl number of the most common HTF, is close to unity proving the validity of the Reynolds analogy, when it differs from precisely

1 it is always lesser than 1. On the contrary, the turbulent Prandtl number of liquid metals is greater than 1, showing that their heat transfer mechanism is different.

$$Pr_t = \frac{\nu_t}{\alpha_t} \tag{2.23}$$

The Reynolds analogy implies the existence of a similarity between the turbulent transport features of momentum and heat. The turbulent viscosity is linked to time and space scales of the turbulent transport of momentum, while the turbulent thermal diffusivity is related to the time and space scales of the turbulent transport of heat. These scales are not similar in low-Prandtl number fluids.

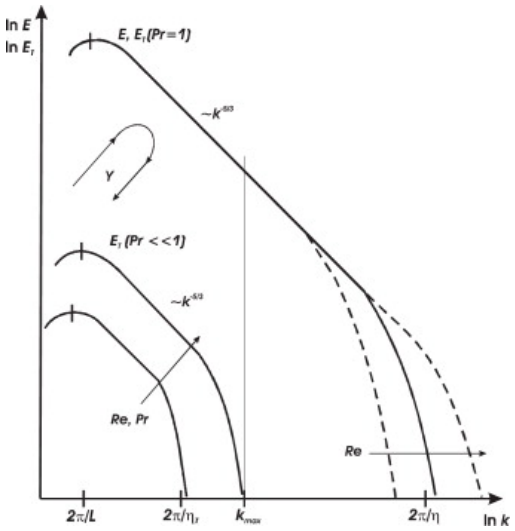

(a) *Sketch of 3D energy spectra $E(k)$ for velocity fluctuations and $E_T(k)$ for temperature fluctuations in forced channel flows (Fig. taken from [18]).*

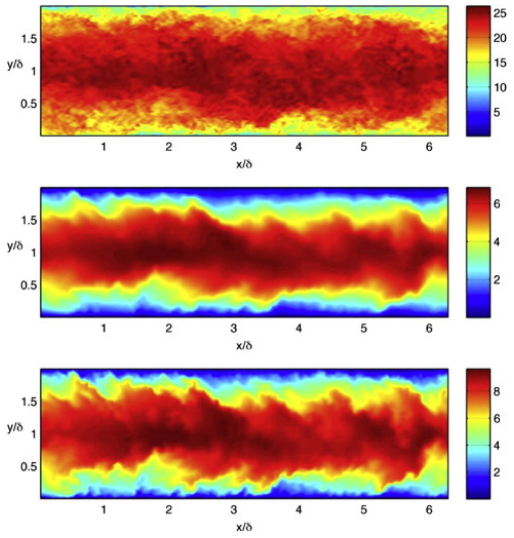

(b) *Instantaneous non-dimensional velocity field (top), non-dimensional temperature field at $Pr = 0.01$ (middle) and $Pr = 0.025$ (bottom). Computed through LES at $Re_\tau = 2000$. (Fig. taken from [19]).*

Figure 2.5: Evidences of the dissimilarities between momentum and heat turbulent scales at low Pr numbers

Evidences of these dissimilarities can be found analyzing Fig.2.5. In Fig.2.5a energy spectra for velocity and temperature fluctuations at different Prandtl numbers are plotted. Energy spectra are derived performing Fourier transforms, so they give information about the turbulence structures in terms of frequencies and wavenumbers.

Energy spectra for velocity fluctuations $E(\kappa)$ give information about the turbulent kinetic energy contained in turbulent structures having wavenumber κ (see [20] for further explanation). The maximum wavenumber indicates the smallest eddy. Energy spectra for temperature fluctuations $E_T(\kappa)$ are related to the temperature variance and give information about the turbulent thermal energy contained in turbulent structures having wavenumber κ.

From this figure it is clear that temperature fluctuations at low-Prandtl number are damped strongly at small scales because of the increased thermal diffusivity. The biggest wavenumber at which $E_T(\kappa)$ is still significant is much smaller than the

maximum wavenumber at which $E(\kappa)$ is still significant; showing that the smallest spatial scale of momentum turbulence is much lower than that of thermal energy turbulence.

Fig. 2.5b shows instantaneous non-dimensional velocity and temperature fields at low Prandtl numbers in a turbulent channel. The dissimilarities between the two fields are evident. The velocity field is much more complex and shows smaller turbulent structures. Further explanations about the peculiar heat transfer mechanism of liquid metals can be found in [18, 19] article from witch the figures have been taken.

A simplified explanation of this phenomenon is given by considering a 2D shear flow having $\overline{U}_2 = 0$ (see Fig.2.6). If a fluid packet δm is considered, it will move along the x_2 direction because of the turbulent fluctuations of velocity $\overline{u_2'^2}$. Moving from point A to point B it will exchange momentum and energy so that in B it will be in equilibrium with the surrounding fluid. In B the velocity of δm will be $\overline{U}_{1\,B}^{\delta m} = \overline{U}_1^A + \delta\overline{U}_1$ and the temperature will be $\overline{T}_B^{\delta m} = \overline{T}^A + \delta\overline{T}$.

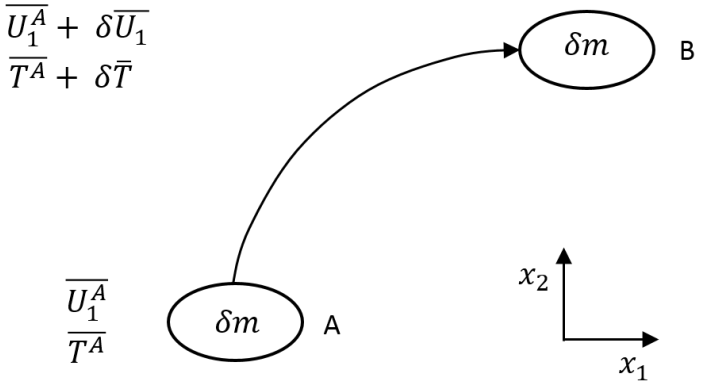

Figure 2.6: Fluid packet moving in a 2D flow with $\overline{U}_2 = 0$

By assuming that the process takes place continuously, the effective velocity in the x_2 direction is proportional to $\overline{u_2'^2}$, $(C\sqrt{\overline{u_2'^2}})$. The turbulent shear stress and heat flux are equal to the net rate of x_1-momentum and energy across an area parallel to the x_1 direction, respectively:

$$\tau_t = C\sqrt{\overline{u_2'^2}}\rho\delta\overline{U}_1$$
$$q_t'' = C\sqrt{\overline{u_2'^2}}\rho c\delta\overline{T}$$

Considering l_{mix} small compared to other dimensions of the system, only the first term can be retained in the Taylor expansion of $\delta\overline{U}_1$ and $\delta\overline{T}$, obtaining then:

$$\frac{\tau_t}{\rho} = C\sqrt{\overline{u_2'^2}}l_{mix}\frac{d\overline{U}_1}{dx_2}$$
$$\frac{q_t''}{c_p\,\rho} = C\sqrt{\overline{u_2'^2}}l_{mix}\frac{d\overline{T}}{dx_2}$$

By comparing the above equations with Eq.(2.21) and Eq.(2.22) it immediately appears that $\nu_t = \alpha_t$ and thus, from the definition of the turbulent Prandtl number of Eq.(2.23), that $Pr_t = 1$.

This approach relies on the assumption that the transfer mechanism for momentum and energy is the same. Neither the molecular viscosity nor the thermal molecular diffusivity play a role because they are considered as negligible with respect to their turbulent counterparts.

However, the turbulent eddies can transfer momentum not only by effect of viscous forces but also by effect of the pressure forces. On the other hand there is no mechanism other than molecular conduction whereby energy can be transferred to or from an eddy. Therefore the two transfer mechanism are not the same.

Thus, it is not surprising that for liquid metals $Pr_t \neq 1$. Indeed, due to the high thermal conductivity of these fluids, an eddy could lose a substantial amount of energy by conduction before having traveled a distance l_{mix}. In this case the turbulent heat transfer is less effective than the turbulent momentum transfer, resulting in $Pr_t > 1$.

On the other hand for fluids with $Pr > 1$ it is possible for an eddy to lose a substantial amount of x_1-momentum before having traveled the whole l_{mix} distance, so while still having a velocity in the x_2-direction. In this case heat is carried to a greater distance than momentum. The turbulent momentum transfer is less effective than the turbulent heat transfer, resulting in $Pr_t < 1$.

Indeed, the common approach of adapting the Reynolds analogy for fluids with Pr around or greater than one, is setting $Pr_t = 0.85$. This approach is not suitable for liquid metals since they usually have $Pt_t > 1$.

In conclusion, the Reynolds analogy does not hold for low-Prandtl number fluids such as liquid metals. Momentum and energy have different turbulent scales. The smallest scales of the velocity field are much smaller than the smallest scales of the temperature field and the turbulence model adopted must take it in to account.

2.3 Problem outline

The numerical analysis of a solar tower receiver tube operated with liquid metals is relevant because it is subject to peculiar boundary conditions. These boundary conditions are extremely uneven both circumferentially and longitudinally causing high thermal stresses that have to be taken in to account while designing the central receiver system.

The thermo-hydraulics design of the receiver is based on correlations predicting the heat transfer coefficient $h(W/m^2K)$. Wall temperature profiles are then derived using that heat transfer coefficient. These correlations have been developed starting from experimental data of uniformly heated tubes. Thus, their applicability to solar receiver tubes is questionable, especially if they are used to compute the temperatures at the wall. A numerical analysis can help in assessing the validity of the correlations.

Nevertheless, it is complicated by the fact that the heat transfer mechanism of liquid metals differs from that of other common fluids. Usually, the turbulent heat flux in the energy averaged equation is modeled by setting a constant turbulent

Prandtl number close to unity by virtue of the validity of the Reynolds analogy. This approach is no more suitable in modeling the thermal turbulence of liquid metals. Different turbulence models, taking in to account the peculiarities of low-Prandtl number fluids, are needed.

Chapter 3

Methodology Adopted

3.1 Turbulence modeling

The numerical analysis performed within this work follows a RANS approach. This approach consists in solving the Reynolds averaged conservation equations (2.16), (2.17), (2.18). The results are velocity and temperature fields of the mean flow. The effects of the turbulence on the mean flow are represented by the turbulent stresses and the turbulent heat flux Eq. (2.19), (2.20) that are modeled as (2.21), (2.22), following Boussinesq hypothesis. The Reynolds stresses than take the form (3.1), where $k = 1/2\,(\overline{u'^2} + \overline{v'^2} + \overline{w'^2})$ is the turbulent kinetic energy.

$$\overline{\overline{\tau}}_t = \begin{bmatrix} \left(2\mu_t \dfrac{\partial \overline{U}_x}{\partial x} - \dfrac{2}{3}k\rho\right) & \mu_t\left(\dfrac{\partial \overline{U}_x}{\partial y} + \dfrac{\partial \overline{U}_y}{\partial x}\right) & \mu_t\left(\dfrac{\partial \overline{U}_x}{\partial z} + \dfrac{\partial \overline{U}_z}{\partial x}\right) \\ \mu_t\left(\dfrac{\partial \overline{U}_x}{\partial y} + \dfrac{\partial \overline{U}_y}{\partial x}\right) & \left(2\mu_t \dfrac{\partial \overline{U}_y}{\partial y} - \dfrac{2}{3}k\rho\right) & \mu_t\left(\dfrac{\partial \overline{U}_y}{\partial z} + \dfrac{\partial \overline{U}_z}{\partial y}\right) \\ \mu_t\left(\dfrac{\partial \overline{U}_x}{\partial z} + \dfrac{\partial \overline{U}_z}{\partial x}\right) & \mu_t\left(\dfrac{\partial \overline{U}_y}{\partial z} + d\frac{\partial \overline{U}_z}{\partial y}\right) & \left(2\mu_t \dfrac{\partial \overline{U}_z}{\partial z} - \dfrac{2}{3}k\rho\right) \end{bmatrix} \tag{3.1}$$

The Boussinesq hypothesis imply some approximations. The term $\left[(2/3)\,k\rho\right]$ is necessary to ensure the correct result for the normal Reynolds stresses. In fact, the trace of $\overline{\overline{\tau}}_t$ is $-(\overline{u'^2} + \overline{v'^2} + \overline{w'^2})$ so it must be equal to $-2k\rho$. If the flow is incompressible the continuity equation gives $\dfrac{\partial \overline{U}_i}{\partial x_i} = 0$. In this case without the term $\dfrac{2}{3}k\rho$, the trace of $\overline{\overline{\tau}}_t$ would be 0. To ensure that the normal Reynolds stresses sum has always the correct physical value, an equal third of $-2k\rho$ is allocated to each normal stress component. This implies an isotropic assumption for the normal Reynolds stresses.

Moreover, the turbulent viscosity is considered as a scalar so the ratio between Reynolds stresses and the mean rate of deformation is assumed to be the same in all directions. A further explanation about the assumptions underlying the Boussinesq approximation can be found in [20]. For the purposes of this work, since the flow analyzed is a simple shear flow in a pipe, the Boussinesq approximations are quite accurate.

Turbulence modeling intervenes to compute the turbulent viscosity ν_t and the turbulent thermal diffusivity α_t. Usually, the most common turbulence models are focused on computing the turbulent viscosity, while the turbulent thermal diffusivity is derived from ν_t by assuming a constant value for the turbulent Prandtl number.

This approach is well proven for fluids subjected to the Reynolds analogy. A typical value is $Pr_t = 0.85$, since it fits very well experimental data for the most common fluids such as air or water [21]. In section 2.2.1, it is explained that this approach is not suitable for liquid metals.

Because of the peculiar heat transfer mechanism of liquid metals several turbulence models focused on computing α_t are used and compared within this work. In particular, a recent published two equations (k_θ-ε_θ) turbulence model for the temperature field (ref.[8]), specifically thought for liquid metals, is assessed.

3.1.1 Flow field turbulence model

The two equation k_θ-ε_θ turbulence model for the temperature field that is assessed within this work requires a specific turbulence model for computing the flow field (ref. [22]) called AKN[1] model. Therefore, the choice of the turbulence model to compute the Reynolds stresses has been forced by compatibility issues with the turbulence model chosen to compute the turbulent heat flux.

AKN k-ε turbulence model

The turbulence model used within this work to compute the turbulent viscosity is the AKN model. This model has been presented by K. Abe, T. Kondoh and Y. Nagano in [22].

It is a two-equations turbulence model belonging to the class of low-Reynolds k-ε models. It requires to solve two additional transport equation; one for the turbulent kinetic energy $k\,[m^2/s^2]$ (3.2) and one for its dissipation rate $\varepsilon\,[m^2/s^3]$ (3.3) .

$$k = \frac{1}{2}\left(\overline{u'^2} + \overline{v'^2} + \overline{w'^2}\right) \tag{3.2}$$

$$\varepsilon = 2\nu\overline{\frac{\partial u_i'}{\partial x_j}\frac{\partial u_i'}{\partial x_j}} \tag{3.3}$$

Turbulence models based on the Boussinesq assumptions usually define a velocity scale ϑ and a length scale l representative of the large scale turbulence. These quantities are used to determine the turbulent viscosity ν_t.

Since ν_t has dimensions $[m^2/s]$, performing a dimensional analysis one finds that the turbulent viscosity can be expresses as a product of the turbulent velocity scale and the turbulent length scale (3.4). In k-ε models these scales are computed

[1] Abe Kondoh Nagano

from the values of the turbulent kinetic energy and its dissipation rate (3.5).

$$\nu_t = C\vartheta l \quad \left[\frac{m^2}{s}\right] \tag{3.4}$$

$$\vartheta = k^{1/2}\left[\frac{m}{s}\right] \quad l = \frac{k^{3/2}}{\varepsilon}\,[m] \longrightarrow \quad \nu_t = C_\nu \frac{k^2}{\varepsilon} \tag{3.5}$$

The peculiarity of AKN turbulence model is that it is a low-Reynolds model. Low-Reynolds models differ from the high-Reynolds ones because the transport equation for k and ε that they implement can be integrated down to the walls.

Near to the wall the velocity tend to zero and the local Reynolds number decreases as well. In this region appropriate non-dimensional quantities can be defined as u^+ (3.6), y^+ (3.7), θ^+ (3.8). Moreover, it is well proven that, close to the walls, the dimensionless velocity u^+ depends only from y^+ ($u^+ = f(y^+)$), following the so-called universal velocity profile.

The profile is linear in the region closest to the wall ($y^+ < 5$), where the behavior of the fluid is dominated by the viscous stresses ($u^+ = y^+$). This region is called viscous sub-layer.

Moving from the wall turbulent stresses gain importance and, first, there is a so-called buffer layer where viscous and turbulent effects are of similar magnitude. Then, a region where turbulent stresses are dominant called log-law layer is found. Within this region, where $30 < y^+ < 500$, $f(y^+)$ is logarithmic.

In Fig.3.1 the profile of u^+ against y^+ in a channel with $Re_\tau = \left(u_\tau \delta/\nu\right) = 640$ is reported. This profile, computed through a direct numerical simulation DNS, has been taken from the DNS database of Kawamura lab `http://murasun.me.noda.tus.ac.jp/turbulence/menu.html` ([23] [24]).

$$u^+ = \frac{u}{u_\tau} \quad ; \quad u_\tau = \sqrt{\frac{\tau_w}{\rho}} \tag{3.6}$$

$$y^+ = \frac{u_\tau\, y}{\nu} \tag{3.7}$$

$$\theta^+ = \frac{T_w - T}{T_\tau} \quad ; \quad T_\tau = \frac{q''}{u_\tau\, \rho\, c_p} \tag{3.8}$$

Turbulence models must be able to reproduce the universal velocity profile, thus, the value of ν_t that they provide must be consistent. High Reynolds turbulence models are based on wall-functions, so that the velocity profile at the wall is not solved and the one presented above is assumed valid. The idea of the wall function approach is to impose the boundary conditions in a location placed inside the log-law layer, so that the turbulence model equations are not solved near to the wall.

Thanks to the known universal behavior of u^+ within the log-region, values for k and ε can be derived and used to create wall functions providing robust boundary conditions to the additional transport equations; resulting in a ν_t consistent with the universal velocity profile at the walls.

If a fluid with a Prandtl number close to unity is considered, the profile of T^+ close to the wall, will be similar to that of u^+. Thus, three sub-layers can be defined in the same range of y^+ used to describe the behavior of u^+, in order to similarly

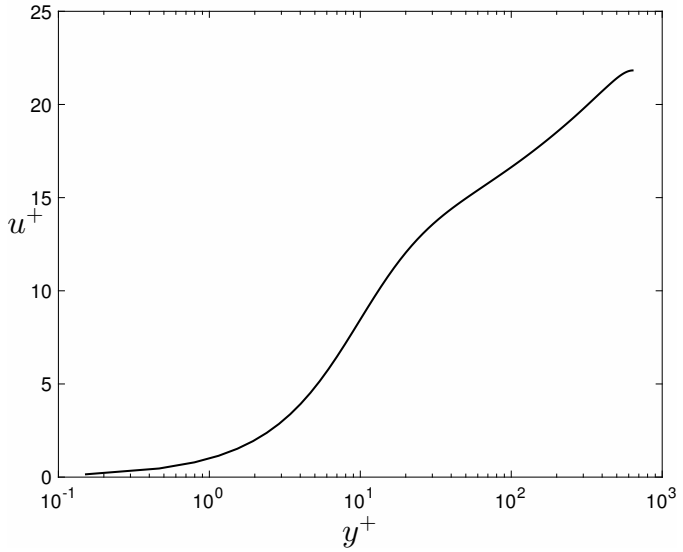

Figure 3.1: DNS data of u^+ against y^+ in a channel flow with $Re_\tau = 640$

describe the behavior of T^+. In the region closest to the wall ($y^+ < 5$) the thermal energy transport is dominated by the molecular diffusivity α and θ^+ is a linear function of y^+ ($\theta^+ = Pry^+$).

Within the buffer layer the turbulent thermal diffusivity α_t grows and both turbulent and molecular thermal energy transports affect the flow. The value of the turbulent diffusivity becomes preponderant within the log layer ($30 < y^+ < 500$). There the profile of θ^+ is logarithmic and the value of α is negligible if compared to α_t. Turbulence models adopting wall-functions consider valid this profile of θ^+ at the wall.

Nevertheless, the profile of θ^+ near to the wall for a low-Prandtl number fluid is different. The molecular diffusivity is greater, so it influences the temperature profile also in regions where fluids, following the Reynolds analogy, are influenced only by the turbulent diffusivity. The extension of the linear sub-layer is bigger. Where u^+ start following a logarithmic function of y^+, θ^+ still shows a linear behavior.

In Fig.3.2 two profiles of θ^+ are reported, one at $Pr = 0.025$ typical of liquid metals Fig.3.2b and one at $Pr = 0.71$ typical of air Fig.3.2a. The profiles have been taken from the DNS database of Kawamura lab `http://murasun.me.noda.tus.ac.jp/turbulence/menu.html` ([23] [24]), and they are referred to a channel with $Re_\tau = 640$ with constant imposed heat flux. The differences are evident; while at $Pr = 0.71$ the logarithmic law is well visible starting from $y^+ \simeq 30$, at $Pr = 0.025$ the linear sub-layer and the buffer layer dominate the profile up to $y^+ \simeq 300$.

For these reasons common wall-functions are not suitable for low-Prandtl number fluids and wall-function specifically thought for these fluids are needed. An attempt to develop appropriate wall-functions for low-Prandtl number fluids can be found in [19]. Nonetheless, since the wall-function approach is still not well proven for liquid metals, the adoption of a low-Reynolds turbulence model as the AKN one, is well suitable.

Low-Reynolds turbulence models adopt damping functions in order to make possible the integration of the transport equations of k and ε down to the wall.

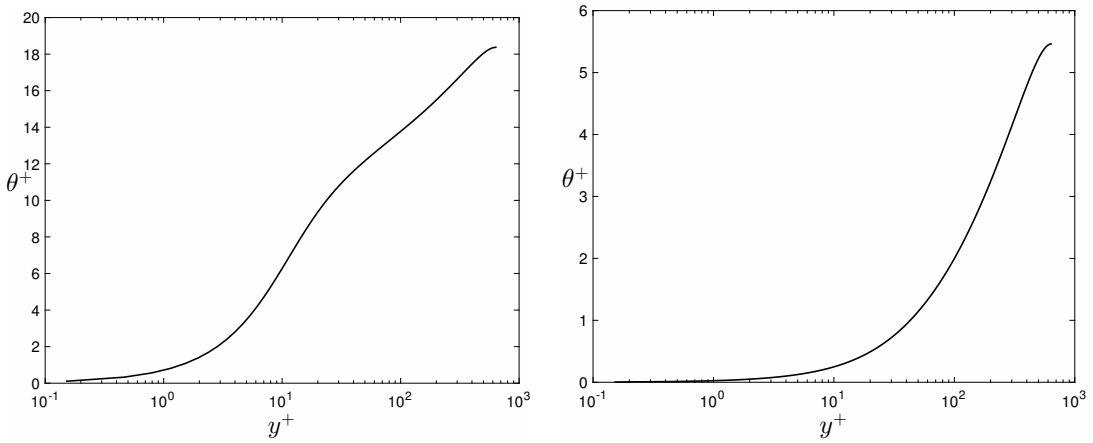

(a) *DNS data of* θ^+ *against* y^+ *in a channel flow with* $Pr = 0.71$ *and* $Re_\tau = 640$.

(b) *DNS data of* θ^+ *against* y^+ *in a channel flow with* $Pr = 0.025$ *and* $Re_\tau = 640$.

Figure 3.2: Near wall profiles of θ^+ at different Prandtl numbers

These wall functions must be consistent with the behavior of the flow next to the wall.

The peculiarity of AKN model is that its damping functions are derived considering the Kolmogorov velocity scale $u_\varepsilon = (\nu\varepsilon)^{1/4}$ instead of the friction velocity u_τ. This because the friction velocity is zero at separating and reattaching points where $\tau_w = 0$, creating singularity points.

The Kolmogorov velocity, instead, has a finite value on the wall surface and permits to avoid the presence of singularities at separating and reattaching points. Thus, the damping functions in the AKN model contain quantities that are referred to the Kolmogorov velocity scale and that are appropriate to model the near wall behavior of the flow. These quantities are defined in (3.9), (3.10) where τ_u is the time scale of the momentum turbulence.

$$R_t = \frac{k^2}{\nu\,\varepsilon} \qquad R_\delta = \frac{y\,u_\varepsilon}{\nu} \tag{3.9}$$

$$\tau_u = \frac{k}{\varepsilon} \tag{3.10}$$

The two additional transport equations proposed by K. Abe, T. Kondoh and Y. Nagano in [22] are reported in (3.11), (3.12) where $-\overline{u_i u_j}$ is modeled using the expression of τ_t defined in (2.21).

$$\frac{\partial k}{\partial t} + \bar{U}_j \frac{\partial k}{\partial x_j} = \frac{\partial}{\partial x_j}\left\{\left(\nu + \frac{\nu_t}{\sigma_k}\right)\frac{\partial k}{\partial x_j}\right\} + P_k - \varepsilon \tag{3.11}$$

$$\frac{\partial \varepsilon}{\partial t} + \bar{U}_j \frac{\partial \varepsilon}{\partial x_j} = \frac{\partial}{\partial x_j}\left\{\left(\nu + \frac{\nu_t}{\sigma_\varepsilon}\right)\frac{\partial \varepsilon}{\partial x_j}\right\} - C_{\varepsilon 1}\frac{\varepsilon}{k}P_k - C_{\varepsilon 2} f_\varepsilon \frac{\varepsilon^2}{k} \tag{3.12}$$

$$P_k = -\overline{u_i u_j}\frac{\partial \overline{U_j}}{\partial x_j}$$

The value of the turbulent viscosity is then computed as (3.13).

$$\nu_t = C_\mu k \tau_{lu} \tag{3.13}$$

$$\tau_{lu} = \Big(f_{1\mu} A_{1\mu} + f_{2\mu} A_{2\mu} \Big)$$

$$f_{1\mu} = \left\{ 1 - \exp\left(- \frac{R_\delta}{14} \right) \right\}^2$$

$$A_{1\mu} = \tau_u \tag{3.14}$$

$$f_{2\mu} = f_{1\mu} \exp\left\{ \left(- \frac{R_t}{200} \right)^2 \right\}$$

$$A_{2\mu} = \tau_u \frac{5}{R_t^{3/4}}$$

$$f_\varepsilon = \left\{ 1 - \exp\left(- \frac{R_\delta}{3.1} \right) \right\}^2 \left[1 - 0.3 \exp\left\{ \left(- \frac{R_t}{6.5} \right)^2 \right\} \right]$$

The values of the model constants are:

$$\begin{aligned} C_\mu &= 0.09, & \sigma_k &= 1.4, & \sigma_\varepsilon &= 1.4, \\ C_{\varepsilon 1} &= 1.5, & C_{\varepsilon 2} &= 1.9 \end{aligned} \tag{3.15}$$

The numerical code used within this work to solve the conservation equations and the two additional k-ε transport equations is FLUENT v.15. This code provides some turbulence models that are already implemented. The AKN model is one of these. It can be found among the low-Prandtl number turbulence models once they have been enabled (for further details see [25]).

The model constants set by the code differ from that presented in [22], so they have been modified according to (3.15).

The proper boundary conditions to be set at the wall are reported in (3.16).

$$\left. \frac{d\,k}{d\,y} \right|_w = \frac{2\,k}{y} \qquad \varepsilon\big|_w = \nu \frac{2\,k}{y^2} \tag{3.16}$$

3.1.2 Temperature field turbulence models

The peculiar heat transfer mechanism of liquid metals explained in section 2.2 affects the choice of the suitable turbulence models to compute the turbulent Prandtl number. There are three possible approaches:

1. *Definition of a constant turbulent Prandtl number*

   This approach introduces the highest level of approximation. It implies not only that turbulent viscosity and the turbulent thermal diffusivity are proportional, but also that the proportionality constant is the same independently from the position and from the other local properties of the flow.

   Nevertheless, this approach is well proven and it gives quite accurate results in many cases; especially if fluids having a Prandtl number close to unity or greater are considered. For example the Pr number of air at room temperature

and pressure is around 0.71 and that of water at the same conditions is around 7. For these fluids experiments shows that the average Pr_t measured is 0.85 and it ranges between 0.7 to 0.9 [21].

When liquid metals are considered these values of turbulent Prandtl number are no more suitable. Correlations based on global values characterizing the flow as Reynolds and Prandtl numbers, can be used in order to compute an appropriate constant value of Pr_t. Within this work the correlation assessed is the one presented by X. Cheng and N. Tak in [26].

2. *Semi-empirical equation providing Pr_t as a function of global and local flow properties*

   This approach still considers the turbulent thermal diffusivity proportional to the turbulent viscosity, however, it sets the proportionality constant accordingly to local flow properties. This results in a variable Pr_t with the coordinates. The correlation used within this work is that proposed by W. M. Kays in [21].

3. *Two equation k_θ-ε_θ turbulence model*

   As many turbulence models used to compute the Reynolds stresses relate the turbulent viscosity to the turbulent kinetic energy and its dissipation rate, the turbulent thermal diffusivity can be related to the temperature variance and its dissipation rate. This approach is based on the solution of two additional transport equations, one for k_θ and one for ε_θ, whose values are than used to model directly α_t. The turbulent thermal diffusivity is not considered proportional to the turbulent viscosity.

   Among the three approaches proposed this one introduces the minor level of approximation, and it requires the maximum computational cost. The k_θ-ε_θ model assessed within this work is the one presented by S. Manservisi and F. Menghini in [8].

Cheng and Tak Pr_t correlation

Cheng and Tak Pr_t correlation is presented in [26], it relates the turbulent Prandtl number to the Peclét number (3.17). The Peclét number, defined as $Pe = Re\,Pr$ is extremely important in describing the heat transfer of liquid metals. Indeed, many correlations show that the Nusselt number can be consider as a function of Pe and not of Re and Pr separately, as it is for fluids with higher Prandtl numbers.

$$Pr_t = \begin{cases} 4.12 & Pe \leq 1000 \\ \dfrac{0.01\,Pe}{\left[0.018 Pe^{0.8} - (7.0 - A)\right]^{1.25}} & 1000 < Pe \leq 6000 \end{cases} \tag{3.17}$$

$$A = \begin{cases} 4.5 & Pe \leq 1000 \\ 5.4 - 9 \cdot 10^{-4} Pe & 1000 < Pe < 2000 \\ 3.6 & Pe \geq 2000 \end{cases}$$

This correlation is specifically thought for LBE whose Prandtl number is around 0.025. This is exactly the Prandtl number used to compute the results in Chapter 5. Moreover, it is based on experimental data and CFD calculations of thermally and hydrodynamically fully developed turbulent convection in tube geometries with constant heat flux. Of course, the boundary conditions studied within this work are different from these ones.

However, it can be inferred that this correlation may be suitable for pipe geometries with an imposed heat flux in general, that is exactly the problem analyzed here. For these reasons the Cheng and Tak correlation is chosen, among many other Pr_t correlations, to be assessed within this work.

Regarding the numerical calculations performed within this work, the value of Pr_t provided by this correlation is known a priori. Buoyancy effects are avoided and flow properties are considered constant with the temperature, so the value of Pr is known once the flow properties are chosen.

The flow field is considered as fully developed and the mass flow rate is fixed. This implies that the Reynolds number is known. Thus, Pr_t is calculated and imposed without any additional computation effort.

Kays Pr_t correlation

Kays Pr_t correlation (3.18) is presented in [21]. It is an empirical correlation derived from the fitting of an analytical solution for Pr_t in pipe flows proposed in [27], which presumably covers all Prandtl numbers. It depends only on local quantities through ν_t and, according to the recent analysis of [19], among three well established correlations for Pr_t, it shows the best agreement with DNS data of liquid metala uniformly heated channel flow.

$$Pr_t = 0.85 + \frac{0.7}{Pr\,\dfrac{\nu_t}{\nu}} \tag{3.18}$$

Actually, also a modified version of (3.18), where the value 0.7 is substituted with 2.0, is proposed in [21]. This seems to better fit with some available experimental data for liquid metals. However, the same author does not exclude possible consistent experimental errors, also because of the large data scatter for these fluids. Thus, Kays Pr_t correlation is used within this work in its original form (3.18).

Since Kays Pr_t correlation is based on local quantities that are computed at every iteration, the value of Pr_t changes accordingly. A UDF function is coupled to the code FLUENT v.15 in order to set the correct value of Pr_t in every point at every iteration (Appendix A Listing A.2).

Kays Pr_t correlation considers the turbulent thermal diffusivity proportional to the turbulent viscosity as the Cheng and Tak Pr_t correlation does. Nevertheless, the proportionality constant varies accordingly to the values of ν_t. Thus, this correlation introduce a minor level of approximation that leads to a greater computational effort. In fact, it requires the solution of a scalar equation at each iteration.

Manservisi k_θ-ε_θ turbulence model

Manservisi k_θ-ε_θ model differs from the previous approaches because it defines turbulence scales for the energy equations different from that of the momentum equation. On one hand, the turbulent length and time scales for the momentum equation are derived from the values of the turbulent kinetic energy k and its dissipation rate ε (3.5), (3.10) .

On the other hand, two additional transport equations are defined for the temperature variance (3.19) and its dissipation rate (3.20). Following this approach the turbulent scales for the temperature equation can be derived from k_θ and ε_θ, instead of being considered equal to that of the momentum.

$$k_\theta = \frac{1}{2}\overline{(T')^2} \tag{3.19}$$

$$\varepsilon_\theta = \alpha\overline{\left(\frac{\partial T'}{\partial x_i}\right)^2} \tag{3.20}$$

The turbulent viscosity and the turbulent thermal diffusivity are no more proportional. This model introduce the minor level of approximation in respect to the two presented above, on the other side it requires a greater computational effort since two additional differential equations must be solved.

K. Abe, T. Kondoh and Y. Nagano presented a two equations k_θ-ε_θ model for the temperature field in [28]. This model was calibrated for air ($Pr = 0.71$) and for a flow field computed with the AKN model presented in section 3.1.1. Manservisi k_θ-ε_θ model [8] originates from this k_θ-ε_θ model by AKN and for this reason it requires the flow field to be computed through the AKN model.

However, it is specifically calibrated for liquid metals. In fact, the model constants are derived from another two equation turbulence model for the temperature field presented in [29], which is specifically thought to be suitable at different Prandtl numbers including the very low ones. Moreover, the damping function in α_t are different from the one presented in [28], accordingly to the near wall behavior of low-Prandtl number fluids presented in section 3.1.1.

The resulting additional transport equations take the form (3.21), (3.22), where $-\overline{u_i T'}$ is modeled using the expression of q_t'' defined in (2.22).

$$\frac{\partial k_\theta}{\partial t} + \bar{U}_j\frac{\partial k_\theta}{\partial x_j} = \frac{\partial}{\partial x_j}\left\{\left(\alpha + \frac{\alpha_t}{\sigma_{k_\theta}}\right)\frac{\partial k_\theta}{\partial x_j}\right\} + P_\theta - \varepsilon_\theta \tag{3.21}$$

$$\frac{\partial \varepsilon_\theta}{\partial t} + \bar{U}_j\frac{\partial \varepsilon_\theta}{\partial x_j} = \frac{\partial}{\partial x_j}\left\{\left(\alpha + \frac{\alpha_t}{\sigma_{\varepsilon_\theta}}\right)\frac{\partial \varepsilon_\theta}{\partial x_j}\right\} - \frac{\varepsilon_\theta}{k_\theta}\left(C_{p1}P_\theta - C_{d1}\varepsilon_\theta\right) + \frac{\varepsilon_\theta}{k}\left(C_{p2}P_K - C_{d2}\varepsilon\right) \tag{3.22}$$

$$P_\theta = -\overline{u_i T'}\frac{\partial \bar{T}}{\partial x_j}$$

The value of the turbulent thermal diffusivity α_t is then computed as (3.23).

$$\begin{gathered}\alpha_t = C_\theta k \tau_{l\theta} \\ \tau_{l\theta} = \Big(f_{1\theta} B_{1\theta} + f_{2\theta} B_{2\theta}\Big) \\ f_{1\theta} = \big[1 - \exp\left(-0.0526\sqrt{Pr}\, R_\delta\right)\big]\big[1 - \exp\left(-0.0714 R_\delta\right)\big] \\ B_{1\theta} = \tau_u Pr_{t\infty} \\ f_{2\theta} B_{2\theta} = \tau_u \left(f_{2a\theta} \frac{2R}{R + C_\gamma} + f_{2b\theta} \sqrt{\frac{2R}{Pr}} \frac{1.3}{\sqrt{Pr} R_t^{3/4}} \right) \\ f_{2a\theta} = f_{1\theta}\, exp\big(-4 \times 10^{-6} R_t^2\big) \\ f_{2b\theta} = f_{1\theta}\, exp\big(-2.5 \times 10^{-5} R_t^2\big)\end{gathered} \tag{3.23}$$

The values of the model constants are:

$$\begin{array}{llll} C_\theta = 0.1, & \sigma_{k\theta} = 1.4, & \sigma_{\varepsilon\theta} = 1.4, & C_\gamma = 0.3, \\ Pr_{t\infty} = 0.9, & C_{p1} = 0.925, & C_{d1} = 1, & C_{p2} = 0.9, \end{array}$$

$$C_{d2} = \Big[1.9(1 - 0.3 \exp\left(-0.0237 R_t^2\right))\Big]\Big[1 - \exp\left(-0.1754 R_\delta\right)\Big]^2$$

The damping functions in the Manservisi k_θ-ε_θ model contain quantities that are referred both to the turbulent scales of velocity and of temperature. These quantities are defined in (3.24), (3.25). Three characteristic times are used within this model: τ_u the dynamical time, τ_θ the thermal time and τ_m the mixed time. The dynamical time is the one used to compute the turbulent viscosity (3.10). R is the ratio between the thermal time and the dynamical time and it appears in the damping function to model the behavior of the turbulent thermal diffusivity within the linear sub-layer and the buffer layer.

$$\tau_u = \frac{k}{\varepsilon} \qquad \tau_\theta = \frac{k_\theta}{\varepsilon_\theta} \qquad \tau_m = \frac{\tau_u 2R}{R + C_\gamma} \tag{3.24}$$

$$R_t = \frac{k^2}{\nu\, \varepsilon} \qquad R_\delta = \frac{y\, u_\varepsilon}{\nu} \qquad R = \frac{\tau_\theta}{\tau_u} \tag{3.25}$$

The proper boundary conditions to be set at the wall for an imposed heat flux are reported in (3.26).

$$k_\theta\big|_w = 0 \qquad \varepsilon_\theta\big|_w = \alpha \frac{2\, k_\theta}{y^2} \tag{3.26}$$

Manservisi k_θ-ε_θ turbulence model is not available as already implemented in the code FLUENT v.15. Thus, it has been coupled to the code through UDFs. The UDF code has been implemented within this work and it is reported in Appendix A listing A.3.

3.2 Inlet and outlet boundary conditions

The velocity and temperature profile of a flow inside a tube changes from the inlet until the fully developed region. The development of the profiles is due to the growth of the boundary layer thickness, which, in a confined flow, ends up occupying the whole section. Once the boundary layer reaches the maximum extension the flow is fully developed.

In Fig.3.3 a sketch of the development of a turbulent velocity profile in a pipe is reported. In turbulent flows the fully developed hydrodynamic condition (3.27) is generally reached for $10 < x/D < 30$.

$$\frac{\partial u}{\partial x} = 0 \tag{3.27}$$

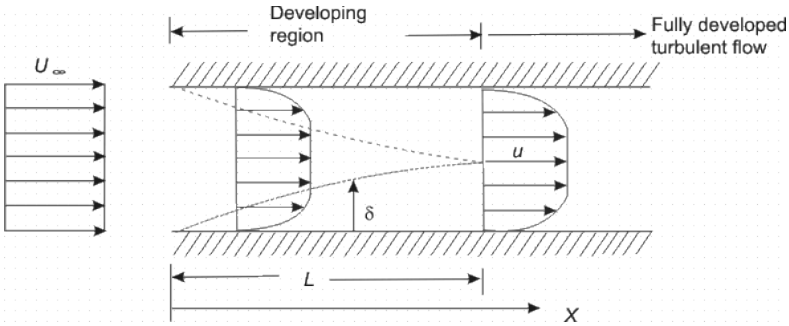

Figure 3.3: Development of the turbulent velocity profile in a tube

From the thermal standpoint a flow is fully developed when Eq.(3.28) is verified; if the boundary condition at the wall is an imposed constant heat flux this implies Eq.(3.29).

$$\frac{\partial}{\partial x}\left(\frac{T_w - T}{T_w - T_b}\right) = 0 \tag{3.28}$$

$$\frac{dT}{dx} = \frac{dT_b}{dx} = \frac{dT_w}{dx} = const \qquad ; \qquad Nu_D = f\big(Re, Pr\big) \tag{3.29}$$

In the equations above T_b is the bulk temperature Eq.(3.30).

$$T_b = \frac{\int_{A_c} \rho c_p \vec{u} \cdot \vec{n} T dA_c}{\dot{m} c_p} \tag{3.30}$$

In Fig.3.4 the behavior of a thermally developed flow in tubes with a uniform heat flux is shown. The figure is taken from [30] and it shows a laminar profile for a fluid with $Pr \simeq 1$, where T_∞ is the bulk temperature at the inlet.

Usually turbulent and laminar fully developed profiles can be distinguished because in turbulent flows the temperature assume almost a constant value with varying r because of the turbulent mixing. The profile is then less smooth with greater gradients at the wall and with the value at the pipe center being almost equal to the cross averaged one.

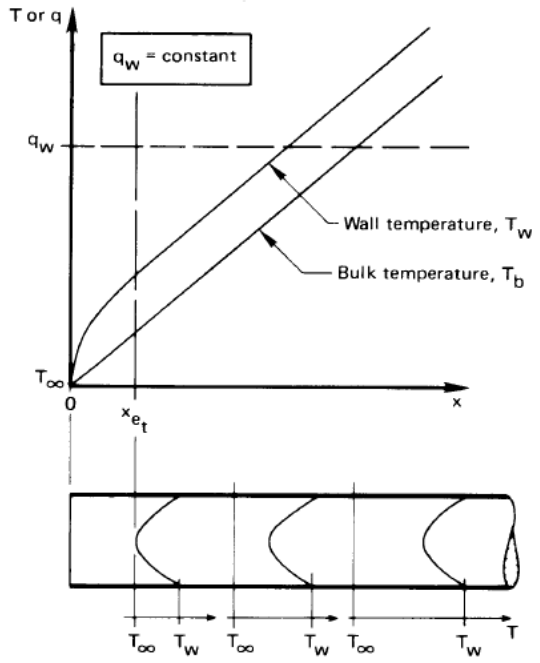

Figure 3.4: Behavior of a thermally developed region in a laminar flow in tubes with a uniform heat flux (Fig. taken from [30])

The lack of turbulent mixing makes laminar profiles smoother and with a shape similar to that of a parabola.

Nevertheless, low-Prandtl number fluids show turbulent temperature profiles similar to the laminar profiles of fluids with $Pr \geq 1$. The higher α implies a higher importance of the conductive heat transfer with respect to the turbulent mixing, resulting in smoother temperature profiles Fig.3.5.

The behavior of a fully developed flow is numerically reproduced by applying cyclic boundary conditions at inlet and outlet sections. The code FLUENT v.15 treats the flow at cyclic boundary as though the opposing periodic plane is a direct neighbor to the cells adjacent to the first cyclic boundary. Thus, when calculating the flow through the cyclic boundary adjacent to a fluid cell, the flow conditions at the fluid cell adjacent to the opposite cyclic plane are used [25].

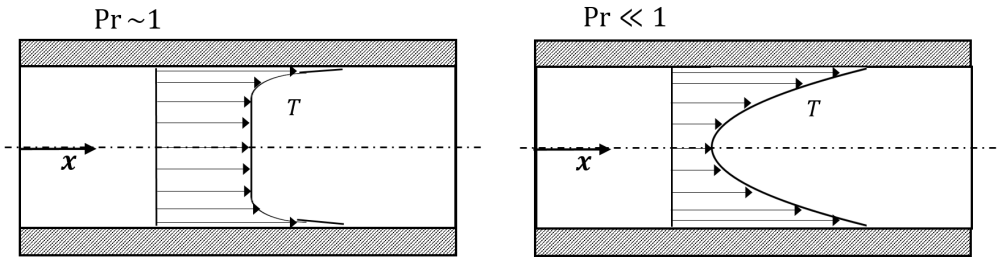

Figure 3.5: Fully developed turbulent temperature profile at different Pr.

Setting the cyclic boundary conditions at the inlet and outlet sections means that when calculating the flow at the inlet plane, the flow conditions at the outlet plane are used.

Getting back to the specific problem that this work is addressing, it has to be analyzed whether the flow inside a tube of a solar central receiver can be considered as fully developed or not.

The pipe of a central receiver is part of a complex hydraulic system, the flow arriving at this portion of the system has already a hydrodynamically well developed boundary layer. Even though the receiver can be placed after curved pipes the fully developed condition is reached again after few pipe diameters.

Being the diameter of a tube in a central receiver always one or two orders of magnitude smaller than the pipe length, the flow field inside can be considered always as hydrodynamically fully developed, given also the fact that the flow is always turbulent.

The proper boundary conditions to be set at the inlet and outlet sections for the momentum equation are then cyclic.

From the thermal point of view things are more complicated. The heat flux imposed on a receiver tube is far from being constant (see Sec. 2.1). The variability of the heat flux over the longitudinal axes prevents the temperature profile from reaching the fully developed condition (3.31) at least with the implications shown in Eq.(3.29).

$$\frac{\partial q}{\partial x} \neq 0 \quad \longrightarrow \quad \frac{\partial T}{\partial x} \neq const \tag{3.31}$$

The boundary conditions imposed at the inlet and outlet sections for the energy equation cannot be cyclic when a heat flux longitudinally varying is imposed. The suitable boundary conditions are then a uniform value of the temperature at the inlet and a zero temperature gradient at the outlet.

Actually the proper treatment at the outlet would be the one represented in Fig. 3.6. The zero gradient conditions should be applied on a section downstream of the last section of the receiver. This assure the simulation to reproduce the behavior of a tube portion included in a bigger hydraulic system.

Two simulations with $Re = 100000$, $Pr = 0.025$, the same fluid and solid properties, the same pipe thickness and the imposed heat flux (2.1) on $L = 30D$ have been computed.

In the first case the zero gradient condition has been imposed at $x/D = 30$ so at the last section of the tube portion simulated. In the second one the zero gradient condition has been imposed at $x/D = 50$, following the approach shown in Fig.3.6.

The results, in term of Nusselt numbers local and global and non-dimensional profiles of wall temperature, differ so little (less then 3.5%) that the first approach is considered appropriate.

In conclusion, when a longitudinally varying heat flux is imposed, as it happens on a tube in a central solar receiver, the suitable boundary conditions are a uniform value of the temperature at the inlet and a zero temperature gradient at the outlet.

Nevertheless, in Sec.5.1 results computed with a circumferentially varying and longitudinally constant heat flux are presented. In these cases a fully developed temperature profile is analyzed. These profile has been simulated by applying cyclic boundary conditions at the inlet and outlet sections even for the energy equation.

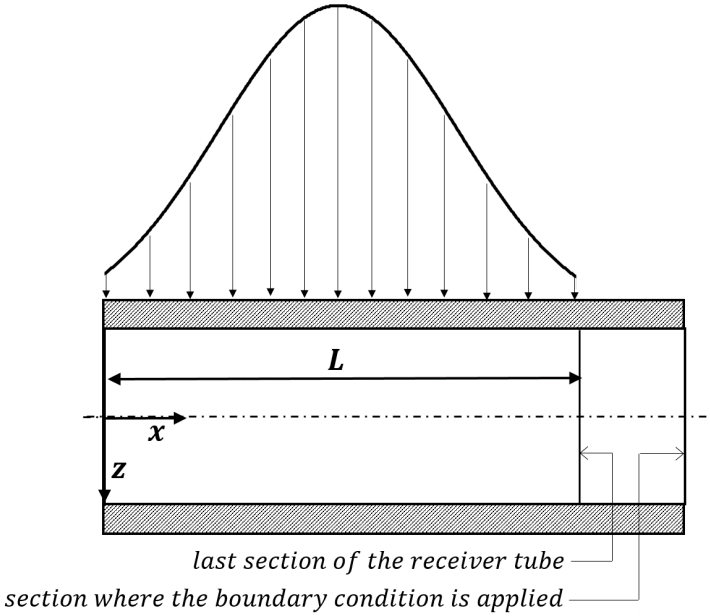

Figure 3.6: Proper position for the zero gradient boundary condition

3.3 Numerical set up

All the numerical simulations performed within this work have been computed assuming a steady-state flow. The predictor-corrector SIMPLE algorithm [31] has been used for the pressure-velocity coupling. The diffusion terms are discretized with a central-difference scheme while a second-order upwind scheme is used for the convective terms [25, 32]. The gradients at the cell center, necessary for the computation of the scalar values at the cell faces, are computed with the so-called least-squares method [25]. The pressure values at cell faces are evaluated according to the method of Rhie and Chow [33] and described in [25].

Buoyancy forces have been neglected and constant thermo physical properties have been considered. This allows to decouple the energy equation from the momentum equations. Therefore, first the latter, together with the turbulence equations of Section 3.1.1, has been numerically solved. Once a converged solution had been reached, the energy equation, together with the heat turbulence equations of Section 3.1.2, has been separately solved, keeping the velocity field, k and ε "frozen".

In the subsequently described simulations, a convergent solution has been assumed when all the following conditions are satisfied:

- constant average drag coefficient on the walls;
- constant average convective heat transfer coefficient on the walls;
- scaled residuals [25] of continuity, momentum and turbulence parameters below 10^{-6}.

Recalling the description of the receiver tube and its boundary conditions made in section 2.1 one finds that there is a symmetry. Thus, only half of the domain needs to be simulated.

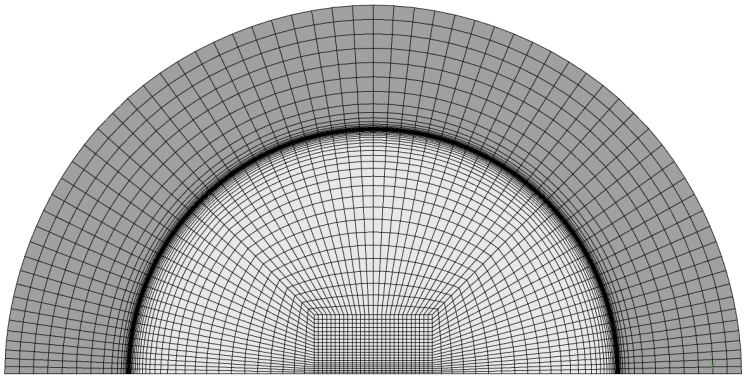

Figure 3.7: Example of the mesh used to compute the results presented in Chapter 5. (Light gray identifies the fluid zone while the dark gray is the solid one)

The geometry has been discretized using block-structured non-uniform hexahedral elements, as for example shown in Fig. 3.7. It must be emphasized that all the meshes used within this work assures that every solution computed has several points within a non-dimensional wall distance, y^+, less than one.

This characteristic is essential when a low-Reynolds turbulence model is adopted. Since the transport equations are integrated down to the walls, the first grid point needs to be placed within $y^+ < 1$, and the near wall region requires a finer spatial discretization in the direction normal to the wall. In Fig. 3.7 it can be noticed that this requirement is fulfilled. The near wall region is located within the light gray zone, where the mesh lines are so fine that they are hard to distinguish and they seem a thick dark line.

Both velocity and temperature fields have been considered as being fully developed in the simulations of Sec.5.1. Therefore cyclic boundary conditions have been imposed at the inlet and outlet sections of the simulated domains.

For the simulations of Sec.5.2.2 only the flow has been considered as fully developed, while for the temperature a uniform value has been specified at the inlet section and a zero gradient at the outlet. In all simulations the mass flow rate has been imposed in order to obtain the specified Reynolds number.

Chapter 4

Methodology Validation

Within this chapter the implemented Manservisi k_θ-ε_θ turbulence model is validated by comparison with the DNS data of [24, 34]. Moreover, simulations are performed in order to compare the results obtained using the Manservisi k_θ-ε_θ model with those obtained using the other ways of computing Pr_t presented in Sec.3.1.2.

4.1 Validation against DNS data

4.1.1 Channel flow

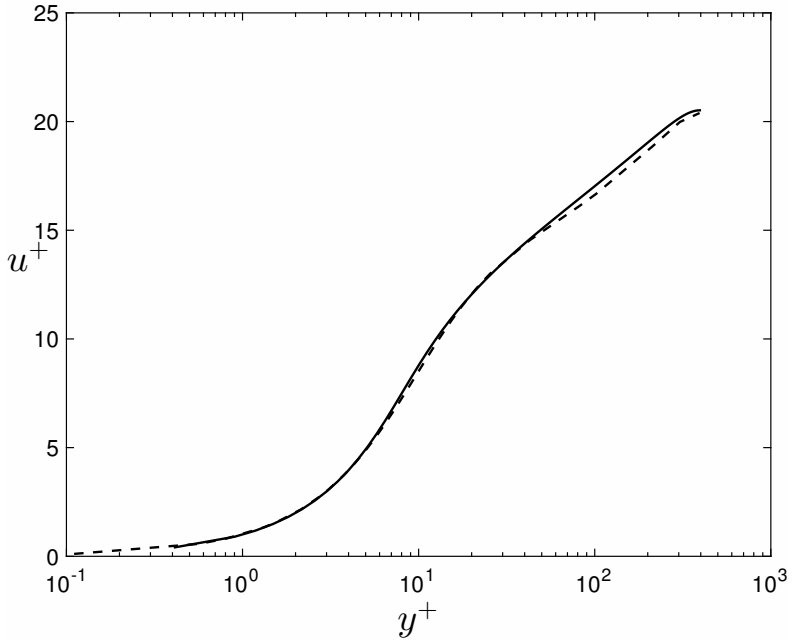

Figure 4.1: Non-dimensional velocity profiles of a channel flow at $Re_\tau = 395$. Comparison between DNS data (dashed line) from [24] and RANS simulation with AKN model (solid line).

DNS database of Kawamura lab (`http://murasun.me.noda.tus.ac.jp/turbulence/menu.html`) provides detailed DNS data of turbulent channel flows. These data

have been used to validate the implementation of the Manservisi k_θ-ε_θ turbulence model and to assess its performances in comparison with the other approaches suitable to compute Pr_t presented in Sec.3.1.2.

The channel flow considered is fully developed both from the hydrodynamic and from the thermal point of view. The mass flow rate has been imposed in order to obtain a $Re_\tau = 395$.

The flow field has been computed with the AKN turbulence model (Sec.3.1.1). The resulting non-dimensional profile of the velocity is compared with the DNS data in Fig.4.1. The two profiles are almost perfectly overlapping; proving that the AKN turbulence model provides quite accurate values of the Reynolds stresses for this flow.

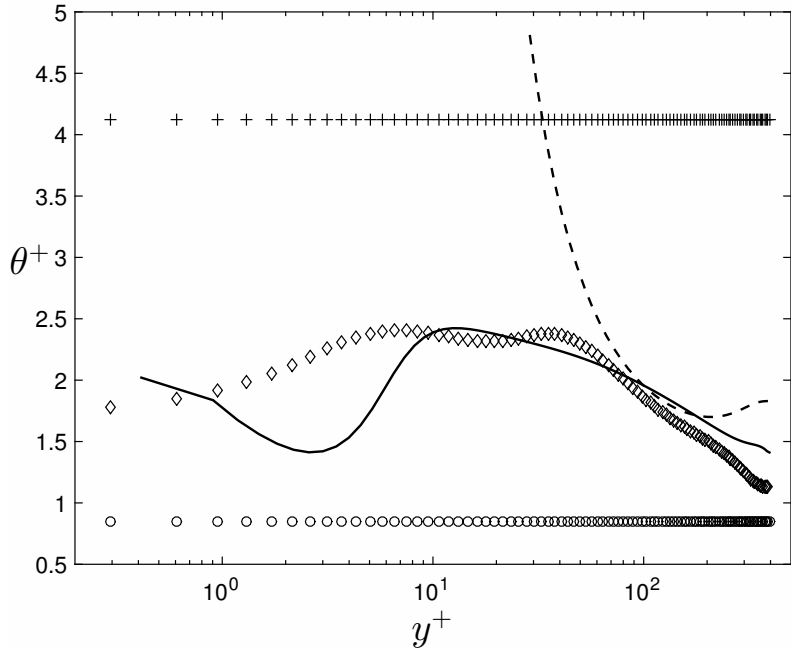

Figure 4.2: Pr_t profiles in a channel flow at $Re_\tau = 395$ with $Pr = 0.025$.Comparison between DNS data ($\Diamond$) from [24], RANS simulation with Manservisi k_θ-ε_θ model (solid line), Pr_t from Eq.(3.18) (dashed line), $Pr_t = 0.85$ ($\circ$), Pr_t from Eq. (3.17) (+).

The thermal boundary condition applied is a constant imposed heat flux. The turbulent Prandtl number has been computed following the approaches presented in Sec.3.1.2, resulting in four different temperature fields. All the temperature fields have been calculated starting from the flow field computed with the AKN model.

The profiles of Pr_t are reported in Fig.4.2. The best agreement with the DNS data is reached with the Manservisi k_θ-ε_θ model. The Kays Pr_t correlation tends to infinity at the wall. Nevertheless, this singularity does not affect the validity of the correlation. High values of Pr_t imply a very small α_t and, in the region next to the wall α_t is in any case negligible if compared to α, thus the resulting temperature profile is not affected by the very high values of the turbulent thermal diffusivity at the wall.

In Fig.4.3 the non-dimensional temperature profiles are plotted together with the DNS data. It can be noticed that both the profiles computed with a constant Pr_t number fail in reproducing the temperature at the channel center.

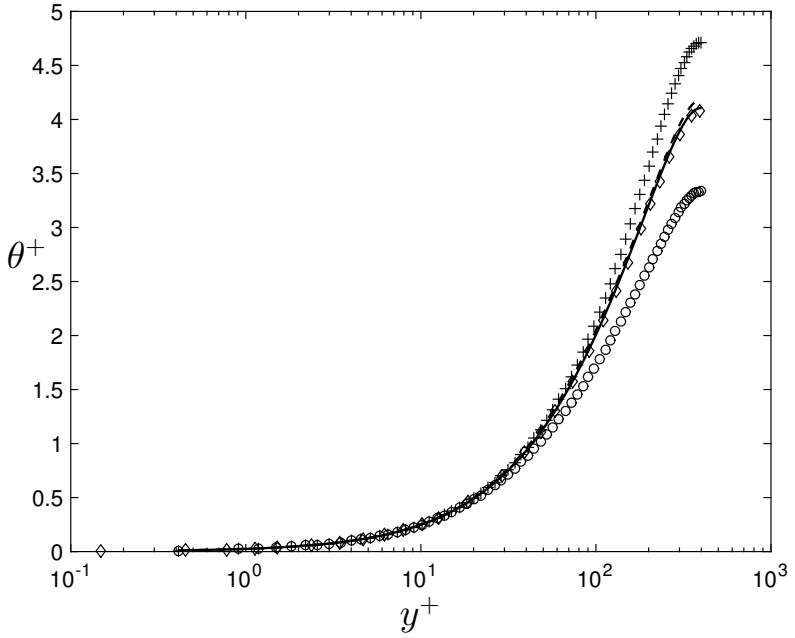

(a)

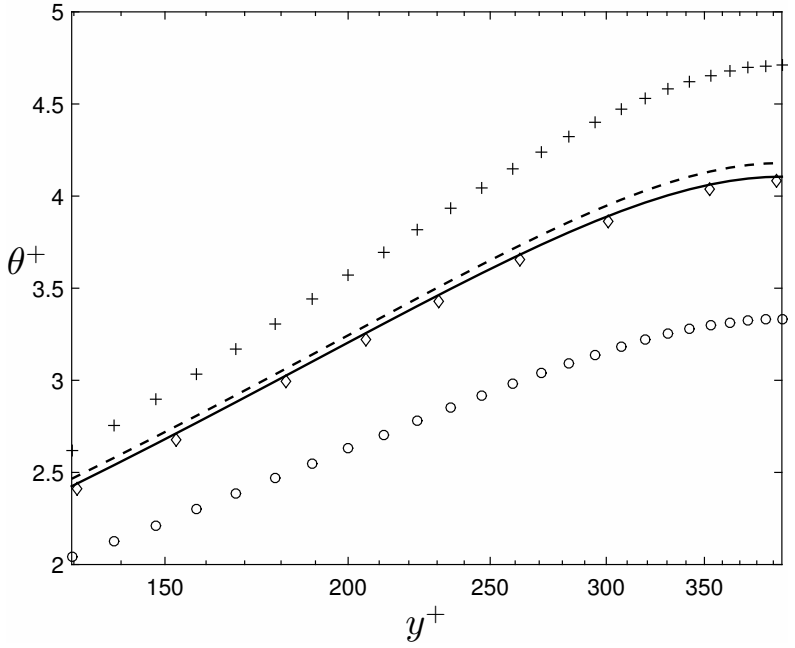

(b) *Zooming at channel center.*

Figure 4.3: Non-dimensional temperature profiles in a channel flow at $Re_\tau = 395$ with $Pr = 0.025$. Comparison between DNS data ($\Diamond$) from [24], RANS simulation with Manservisi k_θ-ε_θ model (solid line), Pr_t from Eq. (3.18) (dashed line), $Pr_t = 0.85$ ($\circ$), Pr_t from Eq. (3.17) ($+$).

The temperature profiles are affected by the values of Pr_t since higher values of the turbulent Prandtl number implies smaller values of α_t. Being smaller the turbulent heat diffusivity and consequently the turbulent mixing, the differences between the wall and the local temperatures inside the channel are higher resulting in higher non-dimensional temperatures.

The Cheng and Tak correlation provides a too high value for Pr_t while a value of Pr_t of 0.85 is too small. The resulting temperature profiles are quite different from the DNS data.

Both the temperature profiles computed through the Manservisi k_θ-ε_θ model and the Kays correlation are in well agreement with the DNS data. Only a zoom at the channel center (Fig.4.3b) highlights the better performance of the Manservisi model.

In conclusion the implementation of the Manservisi model is validated since the comparison with the DNS data shows the same results presented by the model authors in [8]. The Manservisi k_θ-ε_θ turbulence model, in combination with the AKN model, shows the best agreement with the DNS data, among the other models assessed, even though the Kays correlation gives also quite satisfactory results.

4.1.2 Pipe flow

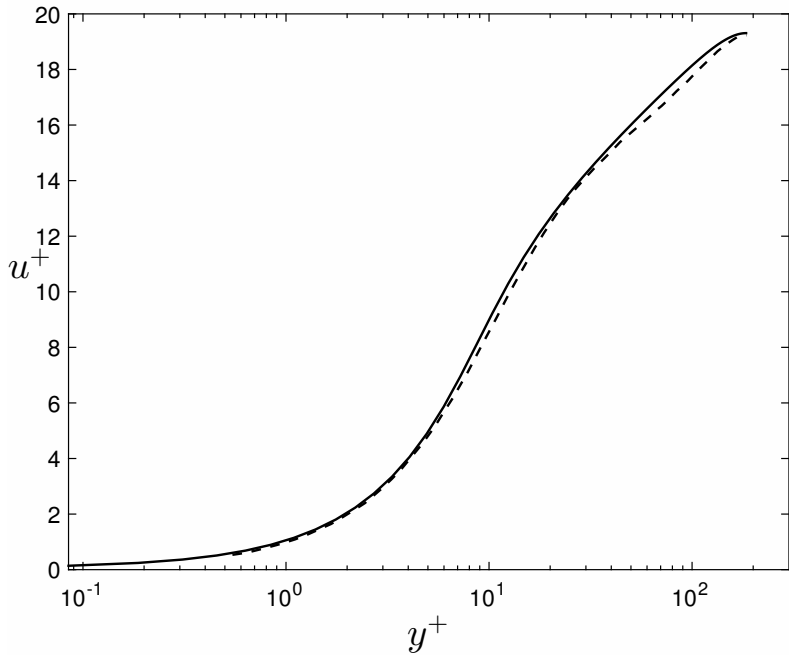

Figure 4.4: Non-dimensional velocity profiles of a pipe flow at $Re_D = 5500$. Comparison between DNS data (dashed line) from [34] and RANS simulation with AKN model (solid line).

Since the problem addressed in this work concerns the flow in a pipe, the behavior of the models when simulating this geometry has to be assessed. Unfortunately the available DNS data computed at low-Prandtl numbers in pipes are few and they all refer to very low Reynolds numbers.

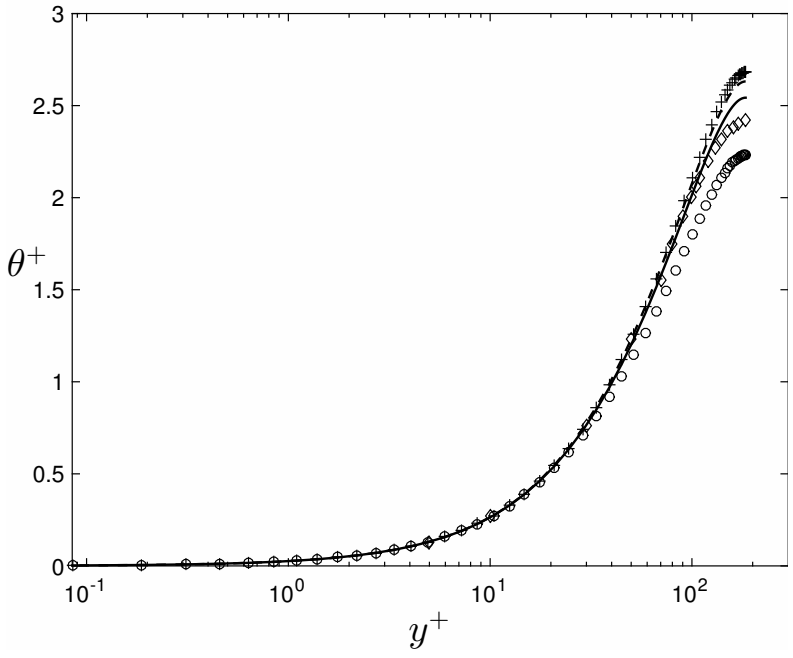

(a)

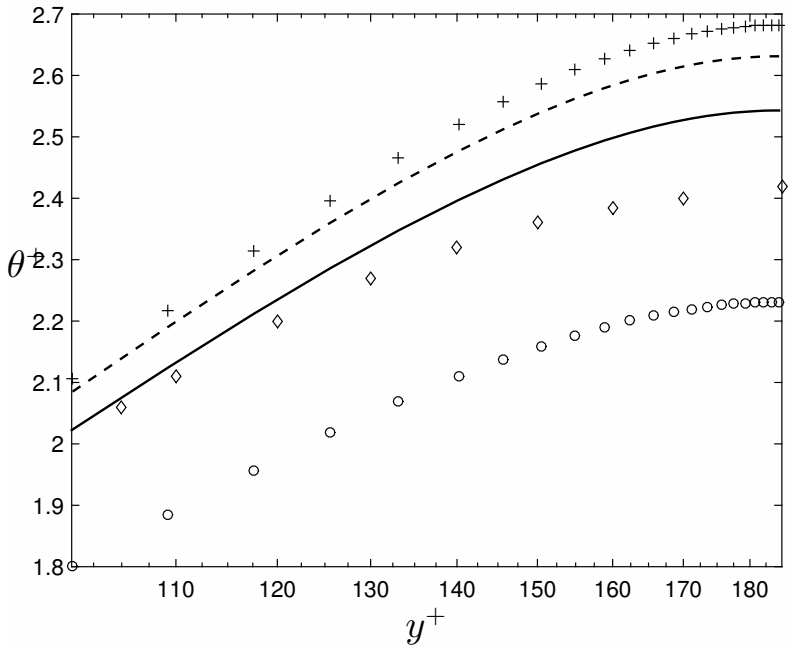

(b) *Zooming at pipe center.*

Figure 4.5: Non-dimensional temperature profiles in a pipe flow at $Re_D = 5500$ with $Pr = 0.026$. Comparison between DNS data (◊) from [24], RANS simulation with Manservisi k_θ-ε_θ model (solid line), Pr_t from Eq. (3.18) (dashed line), $Pr_t = 0.85$ (○), Pr_t from Eq. (3.17) (+).

A numerical analysis of a turbulent pipe flow ($Re_D = 5500$) with a uniform imposed heat flux at $Pr = 0.026$ performed through DNS can be found in [34]. The data taken from this article has been used to assess the performance of the different turbulence models in pipes geometry.

The flow has been considered as fully developed both from the hydrodynamic and from the thermal point of view. The mass flow rate has been imposed in order to obtain a $Re_D = 5500$. The flow field has been computed with the AKN turbulence model and the resulting non-dimensional profile of the velocity matches very well the DNS data (Fig.4.4).

The temperature profiles have been computed through the different approaches presented in Section 3.1.2 and they are plotted in their non-dimensional form together with the DNS data in Fig.4.5. As for the channel flow both the profiles computed with a constant Pr_t number are quite different from the DNS data at the pipe center.

A zoom at the pipe center (Fig.4.5b)highlights that the differences between the non-dimensional temperature profiles computed with the Manservisi k_θ-ε_θ model and the Kays correlation are bigger than the ones detected for the channel flow. The model reaching the best agreement with the DNS data is the Manservisi k_θ-ε_θ one.

It can be noticed that both the non-dimensional temperature profiles in the channel and in the pipe are composed entirely by the linear and the buffer layer. The logarithmic dependence of T^+ from y^+ is not visible while it is well visible the logarithmic dependence of u^+ from y^+ (see Sec.3.1.1).

4.2 Validation against correlation data

In order to assess the performances of the different thermal turbulence models in pipe geometries at high Reynolds number, a comparison with the data provided by a suitable Nusselt correlation is here presented. In [15] a review of the available Nusselt correlations for liquid metals is performed. Considering all the experimental data of liquid metals flowing in pipes with a constant imposed heat flux, the best fitting is given by the Skupinski correlation [35] (Eq.(4.1)).

$$Nu = 4.82 + 0.0185\, Pe^{0.827} \tag{4.1}$$

Simulations adopting the four different approaches to compute the turbulent Prandtl number have been done at $Pe = 2435$ and $Pr = 0.025$ with a constant imposed heat flux in a pipe geometry. The flow has been considered as fully developed both from the hydrodynamic and from the thermal point of view.

The Nusselt numbers derived from these simulations have been compared with the one given by the Skupinski correlation. The results of the comparison are summarized in table 4.1. The Manservisi k_θ-ε_θ model shows the best agreement with the correlation with a percentage error of only -3.4%; while none of the results obtained using any of the other Pr_t correlations are within $\pm 10\%$.

This result, together with the one presented in Sec.4.1, confirms the remarks given in Chapter3. The Manservisi k_θ-ε_θ is the only model, among the ones assessed

Table 4.1: Nusselt numbers obtained adopting different Pr_t models with $Pe = 2435$ and percentual differences between them and the Nu_D resulting from Skupinski correlation Eq.(4.1).

	k_θ-ε_θ	Eq. (3.18)	Eq. (3.17)	$Pr_t = 0.85$
Nu_D	15,96	18,66	12,75	22,72
$\Delta Nu\%$ from Eq.(4.1)	−3,4%	13%	−30%	37%

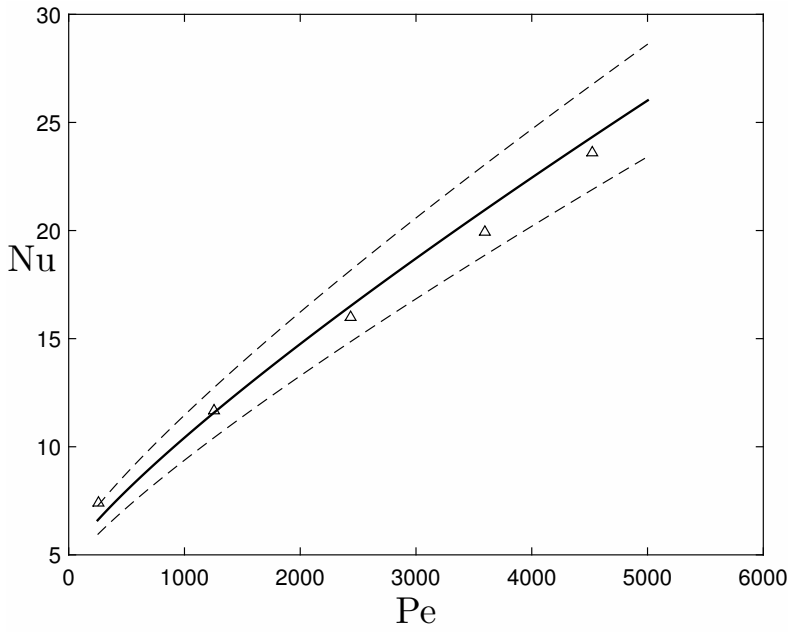

Figure 4.6: Nu_D at different Peclét numbers from Skupinski correlation [35] (solid line) and from simulations with Manservisi k_θ-ε_θ model (△). Dashed lines are ±10% from Skupinski correlation

here, providing a time scale for the thermal turbulence different from the one provided for the momentum turbulence.

This peculiarity is crucial in modeling the heat transfer of liquid metals and the comparisons with DNS data and proper Nusselt correlations confirm the better performance of the Manservisi k_θ-ε_θ model. In particular it can be noticed that the Manservisi k_θ-ε_θ model gives results in better agreement with the DNS data with respect to the other models especially at the pipe and channel center, where the value of α_t gains importance. Therefore, this shows that the turbulent heat flux is more precisely computed by the Manservisi k_θ-ε_θ model.

Models adopting a constant turbulent Prandtl number show poor performances not only when Pr_t is set equal to 0.85 but also when it is computed using the Cheng and Tak correlation (3.17) that is specifically thought for liquid metals.

The Kays correlation gives acceptable results and by virtue of the little additional computational effort that it requires it can be a viable option in computing thermal fields of liquid metals, even though further assessments on its performances are required.

In conclusion the Manservisi k_θ-ε_θ model seems the more reliable option to compute thermal fields of low-Prandtl number fluids.

4.3 Comparison with a semi-analytical solution for uneven imposed heat flux

To assess the performances of the different thermal models when an uneven heat flux is applied, DNS or experimental data adopting this kind of boundary conditions are needed. Unfortunately, according to the author's knowledge, there are no data available for liquid metals flowing in pipe undergoing to an uneven imposed heat flux.

There is, in general, a limited number of experimental investigations for these boundary conditions, probably because of the difficulties in the experimental setup. The most comprehensive work is still the old one of [36] for air. Two others, recently appeared for molten salts [37, 38], are not as complete in the description of the experimental loop and test conditions as well as in the presented experimental results.

Nonetheless, a semi-analytical solution for a longitudinally constant and cosinusoidally varying heat flux distribution over the whole tube's periphery, in principle valid for all Prandtl numbers, has been first given by Reynolds [6] and successively refined by Gärtner et al. [7]. These semi-analytical solutions are here compared with the results of RANS simulations adopting the thermal models presented in Sec.3.1.2.

The semi-analytical solutions proposed consider the case of a hydrodynamically fully developed flow of a fluid having constant properties. The solutions supply the fully developed temperature profile in a circular tube with an imposed wall heat flux having form (4.2).

$$q''_w(\varphi) = q''_0 + F(\varphi) = q''_0 + \sum_{n=1}^{\infty} \left[a_n \sin(n\varphi) + b_n \cos(n\varphi) \right] \tag{4.2}$$

Therefore, the simulations performed consider a case with hydrodynamically and thermally fully developed flow with a cosinusoidally varying heat flux over the perimeter having equation (4.2). The properties of the fluid have been considered constant resulting in a $Pr = 0.03$. The mass flow rate has been imposed in order to obtain $Re_D = 10^5$.

The differential equation governing the temperature field take the form (4.3).

$$u\frac{\partial T}{\partial x} = \frac{1}{r}\frac{\partial}{\partial r}\left[r\left(\alpha + \alpha_t\right)_r \frac{\partial T}{\partial r} \right] + \frac{1}{r^2}\frac{\partial}{\partial \varphi}\left[\left(\alpha + \alpha_t\right)_\varphi \frac{\partial T}{\partial \varphi} \right] \tag{4.3}$$

The semi-analytical solutions to this equation provided in [6, 7] differ in the way they compute the term $(\alpha + \alpha_t)$. Reynolds [6] states that $(\alpha_t)_r = (\alpha_t)_\varphi$, while the solution by Gärtner [7] accounts for the anisotropy of the turbulent thermal diffusivity by using two different values of α_t ($(\alpha_t)_r \neq (\alpha_t)_\varphi$).

Both the solutions provided are semi-analytical because they adopt models to compute the value of the turbulent thermal diffusivity. Here the solution by Reynolds is extensively described, in any case the complete description of the solution provided by Gärtner et al. can be found in [7].

The local temperature can be expressed as (4.4) where the bulk temperature can be determined from an overall energy balance. Splitting the temperature difference in two parts (4.5) and linking it to the imposed heat flux one finds that ΔT_0 can be considered as dependent only on q''_0 while $g(r, \varphi)$ is dependent only on $F(\varphi)$.

Eq.(4.3) can be expressed as (4.8) and since $g(r, \varphi)$ does not contribute to bulk temperature rise, it has to satisfied the elliptic equation (4.9).

$$T(r, x, \varphi) = T_b(x) - \Delta T(r, \varphi) \tag{4.4}$$

$$\Delta T(r, \varphi) = \Delta T_0(r) + g(r, \varphi) \tag{4.5}$$

$$q''_w(\varphi) = \lambda \left(\frac{\partial T}{\partial r} \right)_{r=r_0} = \lambda \left(\frac{\partial g}{\partial r} \right)_{r=r_0} = F(\varphi) \tag{4.6}$$

$$g(r, \varphi) = \frac{r_0}{\lambda} \sum_{n=1}^{\infty} R_n(r) \left[a_n \sin(n\varphi) + b_n \sin(n\varphi) \right] \tag{4.7}$$

$$u\frac{\partial T_b}{\partial x} = \frac{1}{r}\frac{\partial}{\partial r}\left[r\left(\alpha + \alpha_t\right)_r \frac{\partial \Delta T_0}{\partial r} \right] + \frac{1}{r}\frac{\partial}{\partial r}\left[r\left(\alpha + \alpha_t\right)_r \frac{\partial g}{\partial r} \right] + \frac{1}{r^2}\frac{\partial}{\partial \varphi}\left[\left(\alpha + \alpha_t\right)_\varphi \frac{\partial g}{\partial \varphi} \right] \tag{4.8}$$

$$\frac{1}{r}\frac{\partial}{\partial r}\left[r\left(\alpha + \alpha_t\right)_r \frac{\partial g}{\partial r} \right] + \frac{1}{r^2}\frac{\partial}{\partial \varphi}\left[\left(\alpha + \alpha_t\right)_\varphi \frac{\partial g}{\partial \varphi} \right] = 0 \tag{4.9}$$

The final differential equation to be solved take the form (4.10).

$$\frac{d}{dr^*}\left(r^* E \frac{dR_n}{dr^*}\right) - n^2 \frac{E}{r^*} R_n = 0 \tag{4.10}$$
$$E(r^*) = \left(1 + \frac{\nu_t}{\nu}\frac{Pr}{Pr_t}\right) \quad ; \quad r^* = \frac{r}{r_0}$$

Once $R_n(r)$ are known even $g(r, \varphi)$ is known and the non-dimensional temperature at the wall can be calculated through (4.11).

$$\frac{T_w(\varphi, x) - Tb(x)}{\langle q''_w \rangle r \lambda_f} = \frac{r_0}{\langle q''_w \rangle r}\left[S_0\, q''_0 + \sum_{n=1}^{\infty} S_n (a_n \sin n\varphi + b_n \cos n\varphi)\right] \tag{4.11}$$
$$S_n = R_n(1) \quad ; \quad S_0 = \frac{\lambda \Delta T_{w\,0}}{q''_0 r_0} = \frac{2}{Nu_0}$$

S_0 depends on the Nusselt number that is computed using a correlation. It should be noticed that in the paper of Reynolds [6], the Nusselt number correlation of Gnielinski [39] has been used to evaluate the wall temperature functions for the mean harmonic also for low-Pr number fluids. Since this correlation is not suitable for liquid-metals here the correlation used to compute Nu_0 is the Skupinski one (4.1).

The heat flux imposed has Eq.(4.12) so that a_n is always 0 and b_n is $q''_0/2$ when $n = 1$ otherwise is always 0.

$$q''(\varphi) = q''_0 \left(1 + 0.5\, \cos(\varphi)\right) \tag{4.12}$$

The numerically computed non-dimensional temperature profiles obtained with the different thermal turbulence model, are compared in Fig. 4.7 with the semi-analytical results. These results have been computed using the first five harmonics.

A crucial point for the semi-analytical results is the computation of E. In Reynolds' article [6] it is modeled assuming a constant value for the Pr_t and computing the turbulent viscosity with a zero-equation model proposed by Cess (see [6]). In [7] the authors used for their calculations a separate expression for the radial as well as for the tangential turbulent Prandtl number, accounting then for the anisotropy of the heat flux.

These two semi-analytical results are plotted together with another one computed using the same expression of [6] for the ν_t and the Kays correlation Eq.(3.18) for the Pr_t.

The non-dimensional temperature profile obtained with Manservisi k_θ-ε_θ model differs markedly from the semi-analytical ones. The differences are more pronounced in the region of higher heat flux, i.e. $0° < \varphi < 90°$.

As shown in Fig.4.8, the difference in the radial profile of (ν_t/ν) adopted by [6] and that resulting from the simulation cannot account for the discrepancy in the values of the non-dimensional temperature profile. Indeed, the results of the simulations with the AKN turbulence model and Pr_t evaluated from the Kays correlation (3.18) are very close to the semi-analytical ones obtained with the same correlation for Pr_t.

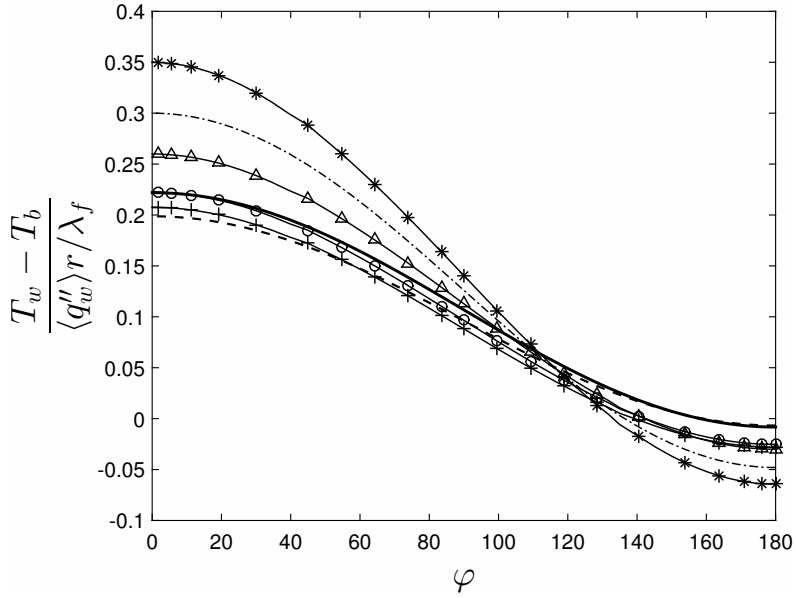

Figure 4.7: Non-dimensional wall temperature profiles at $Re = 10^5$, $Pr = 0.03$. Semi-analytical solutions from [6] (dashed dotted line), [7] (dashed line), E computed with Cess and Kays correlations (solid). RANS simulations with AKN model and k_θ-ε_θ model ($\triangle$), Kays correlation (o), $Pr_t = 0.85$ ($+$) and Pr_t from (3.17) ($*$).

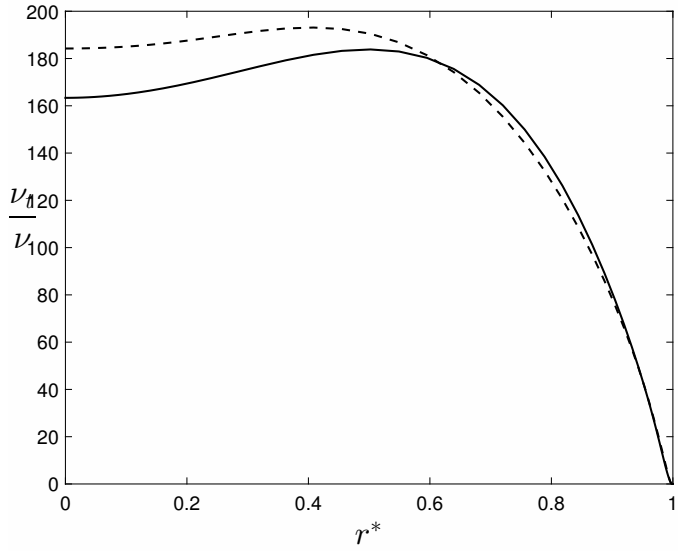

Figure 4.8: ν_t/ν profiles at $Re = 10^5$ from Cess equation (solid line) [6] and AKN model (dashed line).

Therefore, the main source of discrepancy resides in the different values between the turbulent Prandtl number calculated with the Manservisi model from those adopted to compute the semi-analytical profiles.

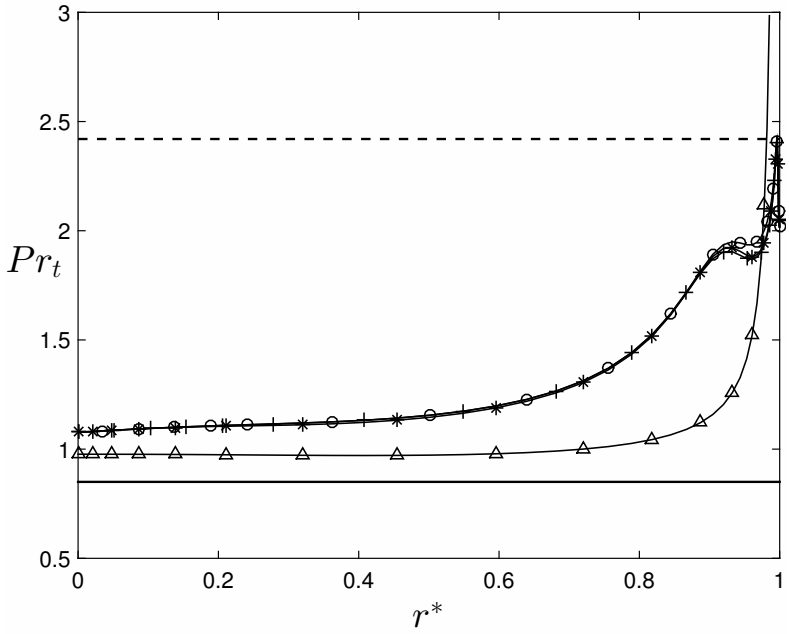

Figure 4.9: Pr_t profiles at $Re = 10^5$, $Pr = 0.03$ with cosinusoidally varying heat flux from RANS simulations with AKN model and k_θ-ε_θ model at $\varphi = 0°$ (o), $\varphi = 90°$ (∗), $\varphi = 180°$ (+), Kays correlation (△), $Pr_t = 0.85$ (solid line) and Pr_t from (3.17) (dashed line).

The Pr_t profiles are plotted versus the radial coordinate in Fig. 4.9. The values of Pr_t from Eq. (3.18) tend to infinity when approaching the wall, because ν_t tends to zero. Due to the thicker thermal viscous sublayer of liquid metals compared to medium-to-high Pr number fluids, these high Prt values might not be an issue since they imply small values of α_t in a region where molecular conduction effectively dominates.

Moreover, even though the profiles of k_θ and ε_θ vary with the radial coordinate for different angular coordinates, φ, the turbulent Prandtl number profiles only show a radial dependency.

The wall temperature predicted with the k_θ-ε_θ model is higher than the other ones in the region of high heat flux and is slightly lower where the non-dimensional temperature assumes negative values, thus where the heat flux is directed from the fluid towards the wall. The only exception is the wall temperature predicted adopting Eq. (3.17) that is higher in $0 < \varphi < 90$ and lower in $\varphi > 90$.

The reason can be found again in the higher predicted Prt, as shown in Fig.4.9, and therefore in a lower turbulent thermal diffusivity. The latter causes a reduced energy mixing and consequently higher differences between wall and bulk temperatures.

Quite surprisingly, the semi-analytical results from [7] show poor agreement, not only with those obtained with the Manservisi k_θ-ε_θ turbulence model but also with the ones evaluated with the AKN model with Pr_t from Eq. (3.18). It can be

argued that the correlations used within this article to compute $(\alpha_t)_r$ and $(\alpha_t)_\varphi$ seem not appropriate, at least for liquid metal flows.

In conclusion, the semi-analytical results of [6, 7] are affected by the fact that they adopt models to compute the values of Pr_t and ν_t. In particular they change considerably with the value of Pr_t and they can be considered reliable only as much as the adopted Pr_t correlation.

4.4 Results of the thermal models assessment

Within this chapter the thermal turbulence models presented in Sec.3.1.2 have been used to compute different cases. The scope has been to compare the obtained results with data coming from DNS, suitable correlations and semi-analytical solutions.

Thanks to the comparison with DNS data of channel flow (Sec.4.1.1) the implementation of the Manservisi k_θ-ε_θ model has been validated. Moreover, being DNS data more precise than RANS ones, they have been used to assess the performances of the different thermal turbulence models.

The model giving results in better agreement with the DNS data is the Manservisi k_θ-ε_θ model. Its better performances are confirmed even at higher Reynolds number since the cases simulating uniformly heated pipe flows computed with this model have Nu numbers that are in better agreement with the Skupinski correlation, with respect to the cases computed adopting other models.

Unfortunately the performances of the thermal models when a non-uniform heat flux is applied cannot be tested because of the lack of DNS and experimental data adopting this configuration.

The semi-analytical solutions found for a cosinusoidally varying heat flux over the perimeter of the tube are affected by the poor reliability of the Pr_t correlation they adopt; thus they are not suitable as a basis for comparison.

Nevertheless, it can be concluded that the best suitable and reliable way of computing the turbulent heat flux for liquid metals is adopting the Manservisi k_θ-ε_θ model in combination with the AKN model. For this reason these models have been used to compute the results that are presented within the following chapter.

Chapter 5

Results

Now that the suitable turbulence model to compute velocity and temperature fields of a liquid metal flowing in a pipe has been chosen; the heat transfer problem regarding a tube in a solar tower receiver operated with liquid metals can be finally addressed.

As already said in Sec.1.3 while designing a central receiver system a proper and reliable prediction of local and global Nusselt numbers and wall temperatures is required. This prediction is made using Nusselt correlations. In particular considering liquid metals the suitable correlations can be: the Skupinski correlation Eq.(4.1) for a fully developed pipe flow and the Ching-Jen and Chiou correlation Eq.(5.14) for a developing flow.

Are these correlations, in principle valid only when a uniform heat flux is imposed, applicable and trustworthy when an extremely uneven heat flux is applied? In order to answer to this question the results of several RANS simulations are presented within this Chapter.

Firstly, a circumferentially varying and longitudinally constant heat flux has been considered and the results are commented in Sec.5.1.

Secondly, in Sec.5.2, a complete analysis of the conjugate turbulent forced convection of a liquid metal flowing in a tube undergoing the boundary conditions present in a central receiver system is presented.

5.1 Longitudinally constant and circumferentially non uniform heat flux

The boundary conditions present on a central solar receiver tube are both circumferentially and longitudinally uneven as seen in Sec.2.1. Nevertheless, first, a simplified problem is considered by analyzing cases with an imposed heat flux circumferentially varying and longitudinally constant.

In particular simulations have been performed for two profiles of circumferentially uneven heat fluxes. Profile "A" has equation (5.1) and it is reported in Fig.5.1, while profile "B" is sketched in Fig.5.2 and it has the form (5.2). Profile "B" has been chosen because it reproduces the heat flux variability, due to the cosine effect (See Sec.2.1), over the circumference of a pipe in a central receiver.

$$A \begin{cases} q''(\varphi) = +q''_{max} & \text{if} \quad 90° \leq \varphi \leq 270° \\ q''(\varphi) = 0 & \text{if} \quad 0° \leq \varphi \leq 90° \wedge 270° \leq \varphi \leq 360° \end{cases} \tag{5.1}$$

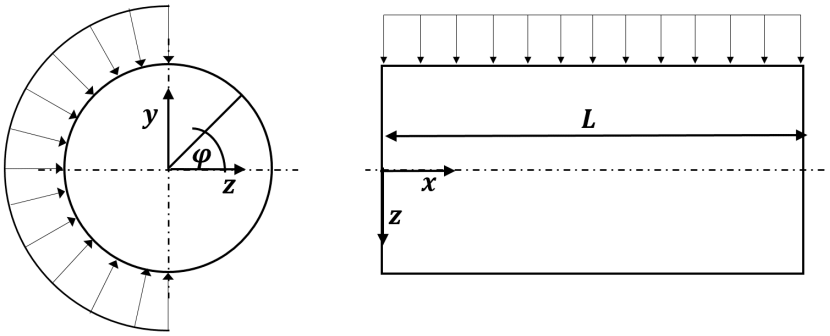

Figure 5.1: Boundary condition "A".

$$B \begin{cases} q''(\varphi) = -q''_{max} \cdot \cos(\varphi) & \text{if} \quad 90° \leq \varphi \leq 270° \\ q''(\varphi) = 0 & \text{if} \quad 0° \leq \varphi \leq 90° \wedge 270° \leq \varphi \leq 360° \end{cases} \tag{5.2}$$

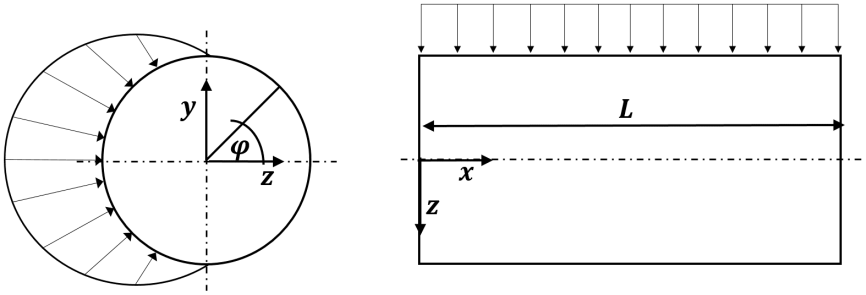

Figure 5.2: Boundary condition "B".

Thanks to the fact that the heat flux profiles considered are longitudinally constant, the temperature field can reach the fully developed condition characterized by:

$$\frac{\partial T}{\partial x} = \frac{\partial T_b}{\partial x} = \frac{\partial T_w}{\partial x} = const \qquad ; \qquad Nu_D = f\big(Re, Pr\big)$$

Consequently the flow has been considered as fully developed both from the hydrodynamic and from the thermal point of view. The mass flow rate has been imposed in order to obtain five different Re_D distributed in between $10^4 < Re_D < 2 \cdot 10^5$ with $Pr = 0.025$.

Circumferentially averaged Nusselt numbers have been derived from the temperature fields computed, as shown in Eq.(5.3). They have been compared with

the Nusselt numbers provided by the Skupinski correlation within the same range of Re_D. The comparison is shown in Fig.5.3.

$$\langle Nu \rangle = \frac{\langle q''_w \rangle \, D}{|\langle T_w \rangle - T_b| \, \lambda_f} \tag{5.3}$$

$$\langle A \rangle = \frac{1}{2\pi \, R} \int_{\varphi=0}^{\varphi=2\pi} A(\varphi) R \, d\varphi \qquad \text{with A being any local variable} \tag{5.4}$$

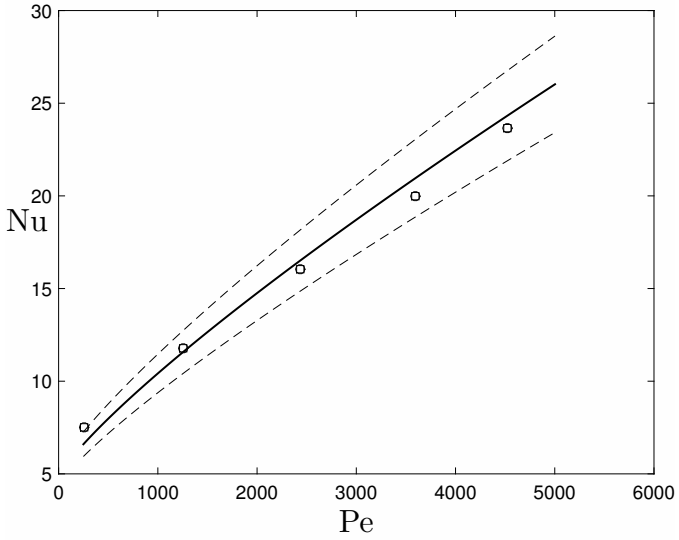

Figure 5.3: Comparison between Nusselt numbers from RANS simulation with AKN and the Manservisi k_θ-ε_θ models and imposed heat flux "A" (□), "B" (o) and from Skupinski correlation (solid line). Dashed lines are ±10% from Skupinsky correlation

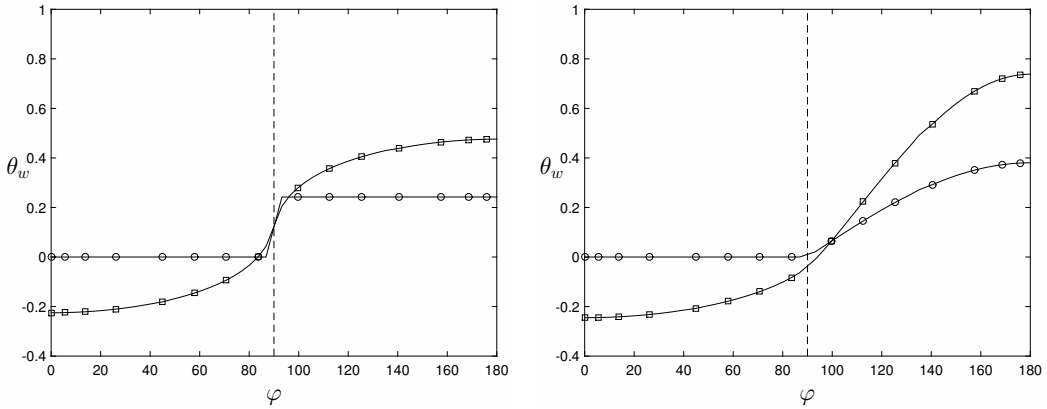

(a) *Boundary condition "A".* **(b)** *Boundary condition "B".*

Figure 5.4: Comparison between temperature profiles from RANS simulations (□) and from Eq.(5.7) with Nu provided by Skupinski correlation (o).

The values collapse together at all Peclét numbers and are within a ±10% range from the Skupinski correlation. It can be inferred that, as already shown in

literature for medium-to-high Prandtl number fluids, also for liquid metals Nusselt number correlations for fully developed flow in uniformly heated tubes can be applied to fully developed cases having a circumferentially non-uniform heat flux imposed.

Another important variable that is needed while designing a central receiver system is the wall temperature profile. In particular knowing the maximum value of the temperature at the wall is important in order to assure the structural integrity.

$$h(\varphi)\left(T_w(\varphi) - T_b\right) = q''_w(\varphi)$$

$$h(\varphi) = \frac{Nu(\varphi)\,\lambda}{D} \quad ; \quad \theta_w(\varphi) = \frac{(T_w(\varphi) - T_b)\,\lambda}{\langle q''_w \rangle\, R} \tag{5.5}$$

$$\theta_w(\varphi) = \frac{2\,q''(\varphi)_w}{Nu(\varphi)\,\langle q''_w \rangle} \tag{5.6}$$

$$\theta_w(\varphi) = \frac{2\,q''(\varphi)_w}{Nu_{Sk}\,\langle q''_w \rangle} \tag{5.7}$$

$$\langle \theta_w \rangle = \frac{2\,\langle q''_w \rangle}{Nu_{Sk}\,\langle q''_w \rangle} \tag{5.8}$$

$$\tag{5.9}$$

Usually the wall temperature is computed from the Nusselt number as in Eq.(5.6). Unfortunately the correlations do not provide a value for the local Nusselt number $Nu(\varphi)$. They provide only a constant value for Nu. Thus, when equation (5.6) is used together with the global Nusselt number provided by the Skupinski correlation becoming Eq.(5.7), the variability of $\theta_w(\varphi)$ is due only to the variability of the imposed heat flux. Where the imposed heat flux is zero, necessarily, even the non-dimensional temperature at the wall becomes zero.

Of course the value of θ_w that results from (5.7) cannot be exact, in fact, what can be precisely derived from Nu_{Sk} is only the circumferentially averaged value of θ_w through equation (5.8). Nevertheless during the design phase of a central receiver system, if CFD[1] simulations are not performed, there are no other means except from Eq.(5.7) to get a rough evaluation of the maximum temperature at the wall.

The other way of computing θ_w is using the temperature field calculated with the simulations. Using this way the non-dimensional wall temperature is not zero even where the imposed heat flux is zero. This because using the computed temperature field means that θ_w is calculated through the actual heat flux and not the imposed one and through the local Nusselt number. Where the actual heat flux tends to zero also the local Nusselt number will tend to zero, making the value of θ_w different from zero.

The non-dimensional wall temperature profiles (θ_w) resulting from the simulations at $Pe = 2435$ are compared with the ones calculated from the Nusselt number provided by the Skupinski correlation using Eq.(5.7) in Fig.5.4. This is useful in order to assess the error made by using correlations for the global Nusselt number to evaluate the circumferentially varying temperature at the wall.

[1] Computational Fluid Dynamic

The profiles differ considerably and the maximum wall temperature computed through the RANS simulations is quite higher that the one derived from Eq.(5.7). Even though the global Nusselt number is quite precisely predicted by the Skupinski correlation, the same correlation is not suited to compute the wall temperature. CFD analysis can then be useful while designing a central receiver system in order to precisely compute the thermal stresses of the pipes.

For the sake of completeness the non-dimensional wall temperature profiles (Fig.5.5) and the Nusselt numbers (Tab.5.1) resulting from simulations adopting the different thermal turbulence models presented in Sec.3.1.2 are reported. The simulations have been computed with $Pe = 2510$ and boundary condition "B" (5.2).

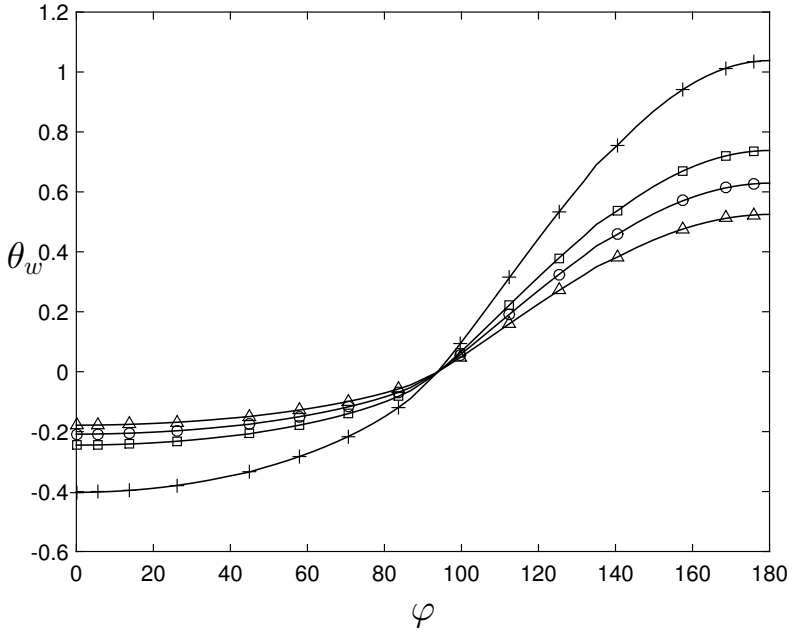

Figure 5.5: Non-dimensional temperature profiles from RANS simulation with $Pe = 2510$ and boundary condition "B" (5.2) adopting the Manservisi k_θ-ε_θ model (□), the Kays correlation (3.18) (o), $Pr_t = 0.85$ (△), Pr_t from Eq-(3.17) (+)

Table 5.1: Nusselt numbers obtained adopting different Pr_t models with $Pe = 2510$ and boundary condition "B" and percentual differences between them and the Nu_D resulting from simulations adopting Manservisi k_θ-ε_θ.

	k_θ-ε_θ	Eq. (3.18)	Eq. (3.17)	$Pr_t = 0.85$
$\langle Nu \rangle$	16,03	18,63	12,74	22,70
$\Delta Nu\%$ from k_θ-ε_θ	−−	16,22%	25,82%	41,61%

5.2 Longitudinally and circumferentially non-uniform heat flux

Within this section the complete analysis of a solar receiver tube operate with liquid metals undergoing to the boundary conditions presented in Sec.2.1 and summarized again in Fig.5.6, is presented.

The problem analyzed is a conjugate heat transfer problem. First of all in Sec.5.2.1 the parameters governing the temperature field are determined. A parametric study has been done for different combinations of the governing parameters and the results in term of wall and bulk temperatures, Pr_t and Nusselt numbers are finally presented in Sec.5.2.2.

It has to be noticed that, since the heat flux applied is non uniform in the axial direction, the temperature field cannot become fully developed from the thermal point of view or, at least, it will never reach a condition where $\partial T/\partial x = const$ and Nu_D is a function of only Re and Pr and not of the axial coordinate.

Thus, here the results in term of Nusselt numbers are compared with the one provided by a correlation in principle valid in the developing region for liquid metals undergoing to an uniform heat flux. This correlation is the Ching-Jen and Chiou correlation Eq.(5.14).

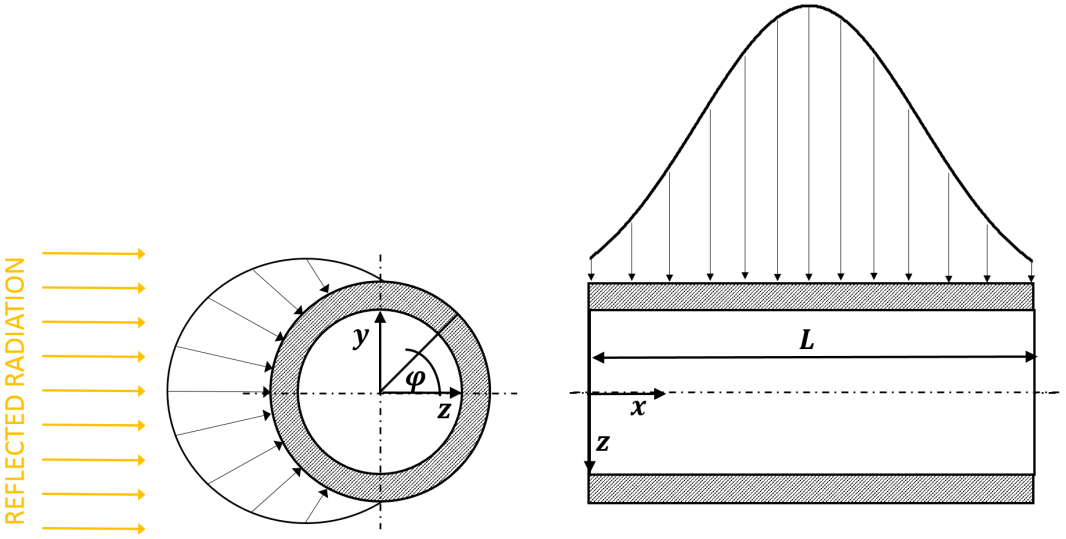

Figure 5.6: Heat flux variability over the length and the axial coordinate of the tube.

5.2.1 Governing parameters

The heat flux imposed on the external tube wall is strongly uneven both in the axial and in the circumferential direction (Fig.5.6). This makes important the analysis of the heat conduction inside the tube wall thickness, since it noticeably affects the temperature field.

The heat transfer inside the tube wall thickness is governed by Eq.5.10. The boundary conditions of this equation link the temperature field of the fluid inside the tube with the one present inside the solid.

There are two sub-domains, solid and fluid, where the temperature field is described by different differential equations, i.e. (2.18) and (5.10), at the interface temperature values and gradients must be consistent. This is a conductive-convective conjugate heat transfer problem.

$$\begin{cases} \dfrac{1}{r}\dfrac{\partial}{\partial r}\left(r\,\dfrac{\partial T}{\partial r}\right)+\dfrac{1}{r^2}\dfrac{\partial}{\partial \varphi}\left(\dfrac{\partial T}{\partial \varphi}\right)+\dfrac{\partial}{\partial x}\left(\dfrac{\partial T}{\partial x}\right)=0 \\ -q''_{max}\cdot\cos(\varphi)\cdot\exp\left[-\dfrac{1}{2}\left(\dfrac{x-L/2}{L/5}\right)^2\right]=-\lambda_s\left.\dfrac{\partial T}{\partial r}\right|_{r=R_o} \\ -\lambda_s\left.\dfrac{\partial T}{\partial r}\right|^{s}_{r=R_i}=-\lambda_f\left.\dfrac{\partial T}{\partial r}\right|^{f}_{r=R_i} \end{cases} \tag{5.10}$$

The system (5.10) can be non-dimensionalised in order to find the non-dimensional parameters affecting the temperature field. In order to do this R_i has been chosen as characteristic length and $(\langle q''_{wi}\rangle\, R_i/\lambda_f)$ as characteristic temperature difference.

The resulting non dimensional variables and equations are shown in (5.11), (5.13), (5.12).

$$\theta=\frac{(T-T_{b0})\,\lambda_f}{\langle q''_{wi}\rangle_L\,R_i}\quad;\quad r'=\frac{r}{R_i}\quad;\quad x'=\frac{x}{R_i} \tag{5.11}$$

$$\begin{cases} \dfrac{1}{r'}\dfrac{\partial}{\partial r'}\left(r'\,\dfrac{\partial \theta}{\partial r'}\right)+\dfrac{1}{(r')^2}\dfrac{\partial}{\partial \varphi}\left(\dfrac{\partial \theta}{\partial \varphi}\right)+\dfrac{\partial}{\partial x'}\left(\dfrac{\partial \theta}{\partial x'}\right)=0 \\ -\dfrac{q''_{max}}{\langle q''_{wi}\rangle_L}\cdot\cos(\varphi)\cdot\exp\left[-\dfrac{1}{2}\left(\dfrac{(R_i/L)\,x'-1/2}{1/5}\right)^2\right]=-\dfrac{\lambda_s}{\lambda_f}\left.\dfrac{\partial \theta}{\partial r'}\right|_{r'=R_o/R_i} \\ -\dfrac{\lambda_s}{\lambda_f}\left.\dfrac{\partial \theta}{\partial r'}\right|^{s}_{r'=1}=-\left.\dfrac{\partial \theta}{\partial r'}\right|^{f}_{r'=1} \end{cases} \tag{5.12}$$

Similarly to Eq.(5.12) even the differential equation Eq.(2.18) governing the temperature field of the fluid must be non-dimensionalized using the same characteristic length and temperature difference. Doing this, another parameter influencing the non-dimensional temperature field is found: the Peclét number. It can be deduced that the overall non-dimensional temperature field is dependent on the non-dimensional coordinates (r', x', φ) and the four non-dimensional parameters defined in Eq.(5.13).

$$r^*=\frac{R_o}{R_i}\quad,\quad \lambda^*=\frac{\lambda_s}{\lambda_f}\quad,\quad \frac{L}{D}\quad,\quad Pe=Re_D\cdot Pr \tag{5.13}$$

The study of the conjugate turbulent forced convection of a liquid metal flowing in a tube with circumferentially and longitudinally varying heat flux (2.1) has been conducted by running simulations for different combination of the governing parameters as listed in Table 5.2.

All the simulations have been performed adopting the AKN turbulence model to compute the flow field, which has been always considered as fully developed. The temperature field, instead, is obviously not fully developed and it has been computed adopting the Manservisi k_θ-ε_θ turbulence model.

Table 5.2: Governing parameters used for the parametric study

r^*	λ^*	L/D	Pe
1 / 1,2 / 1,5	0,88 / 1,4 / 5,5	10 / 30 / 50	1255 / 2510 / 3766 / 5021

The range of variability of the governing parameters has been chosen in order to be appropriate for engineering problems related to solar thermal receivers. In particular the range of variability of λ^* is restricted because both the fluid and the solid are metals, so their thermal conductivities are of the same magnitude.

In a central receivers L/D can be even much greater than 50, nevertheless since this work is addressed to the construction of SOMMER, the range of L/D studied is related to the dimensions of the facility.

5.2.2 Parametric study results

The final results are here presented in term of wall and bulk temperatures, Nusselt numbers and turbulent Prandtl numbers. The non-dimensional temperatures are evaluated as (5.11). The variables plotted are local, circumferentially averaged ($\langle\cdot\rangle$) (5.14) or circumferentially and longitudinally averaged ($\langle\cdot\rangle_L$) (5.15).

$$\langle A(\tilde{x})\rangle = \frac{1}{2\pi\, R}\int_{\varphi=0}^{\varphi=2\pi} A(\varphi) R\, d\varphi \tag{5.14}$$

$$\langle A\rangle_L = \frac{1}{L}\int_{\tilde{x}=0}^{\tilde{x}=1} \langle A\rangle\, d\tilde{x} \tag{5.15}$$

First the influence of a varying λ^* and r^* is analyzed. In Fig.5.7a the downstream variation of the dimensionless inner, outer and bulk fluid temperatures is shown by varying the solid-to-fluid thermal conductivity ratio, λ^*. In Fig.5.7b the same temperatures are plotted at different outer-to-inner radius ratio, r^*.

It can be seen that the profiles of θ_b and θ_{wi} are perfectly overlapping in both figures, showing no dependence on these parameters, at least for the specified range of λ^* and r^* here investigated.

Nevertheless, these parameters affect the wall thermal resistance per unit length that is defined as

$$R_{th} = \frac{\ln\left(r^*\right)}{2\pi\ \lambda_s} \quad \left[K/(W\, m)\right]$$

The wall thermal resistance has a damping effect on the heat flux distribution on the inner tube's surface. Conversely, θ_{ow} decreases by decreasing the wall thermal resistance, i.e by an increase of λ^* or a decrease of r^* as it can be seen respectively in Fig.5.7a and Fig.5.7b.

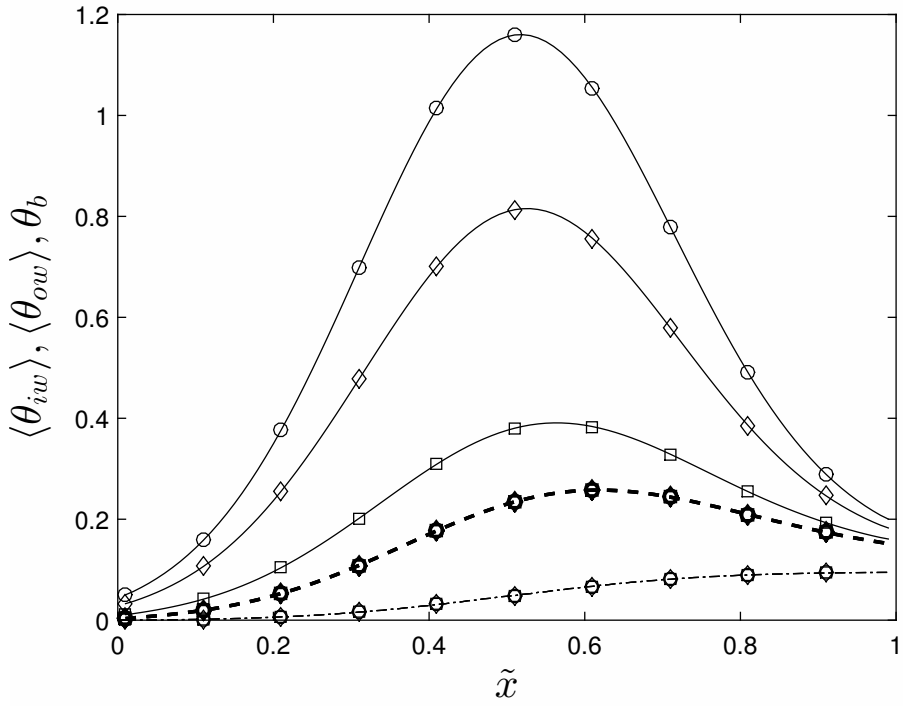

(a)

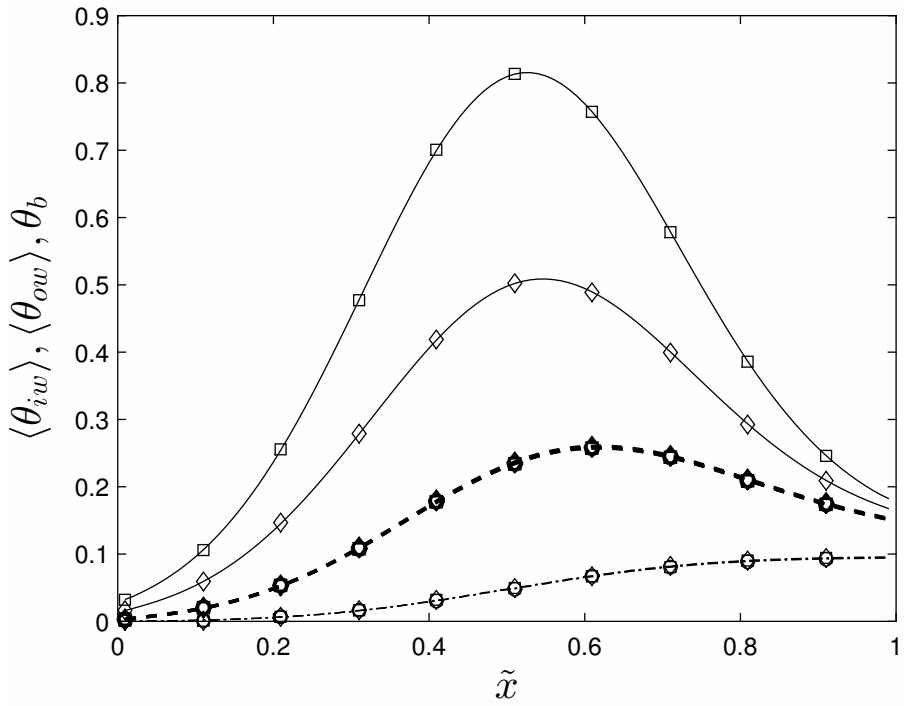

(b)

Figure 5.7: Profiles of θ_{ow} (solid line), θ_{iw} (thicker dashed line), θ_b (dahed-dotted) for $L/D = 30$, $Pe = 2510$ and
a) $r^* = 1.5$; $\lambda^* = 0.88$ (o), $\lambda^* = 1.4$ ($\diamond$), $\lambda^* = 5.5$ ($\square$)
b) $\lambda^* = 1.4$; $r^* = 1$ (o), $r^* = 1.2$ ($\diamond$), $r^* = 1.5$ ($\square$)

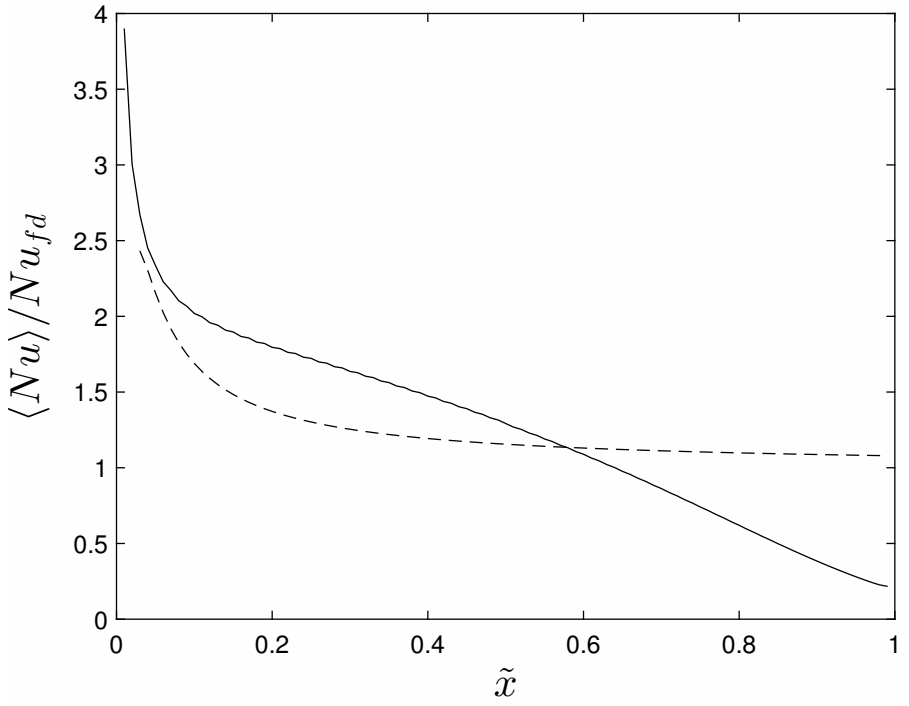

(a)

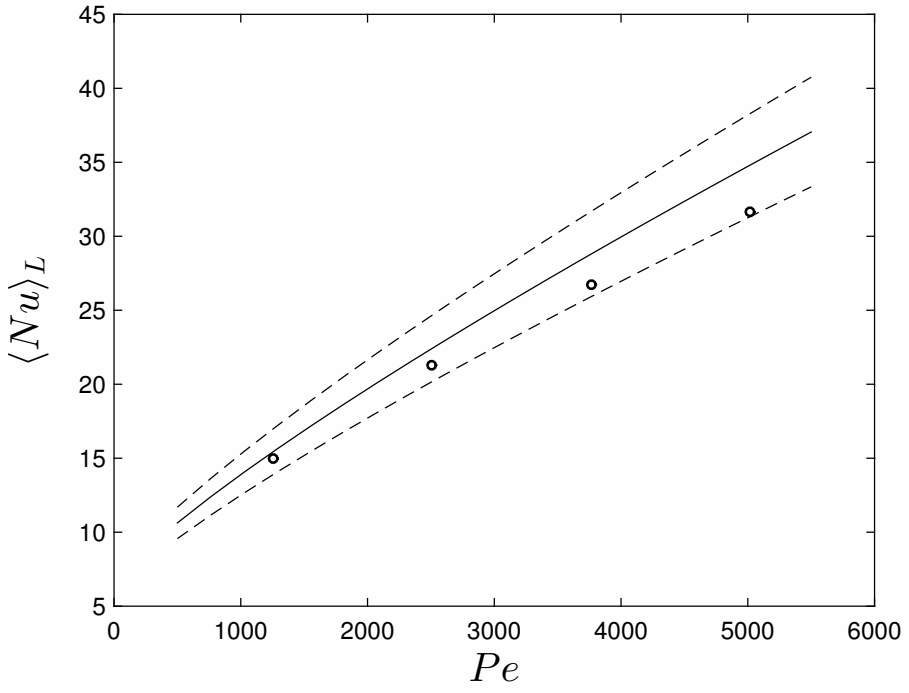

(b)

Figure 5.8: Profiles at $\lambda^* = 1.4$, $r^* = 1.5$, $L/D = 30$ of
a) $\langle Nu \rangle$ for $Pe = 2510$ from the RANS simulation with the k_θ-ε_θ model (solid line) and from the Ching-Jen and Chiou correlation Eq.(5.14) (dashed line)
b) $\langle Nu \rangle_L$ from the RANS simulations with the k_θ-ε_θ model (o) and from the Ching-Jen and Chiou correlation Eq.(5.15) (solid line). Dashed lines are ±10% from the correlation

One important peculiarity of the heat transfer problem here analyzed is that, because of the variability of the heat flux over the pipe length, the flow here will never tend to a fully developed condition characterized by (3.29).

This can already be noticed by observing that the bulk and the wall fluid temperatures in Fig.5.7 do not show a linear dependence on $\tilde{x}$. Moreover, it is interesting to analyze the profile of the circumferentially averaged Nusselt number.

When a developing pipe flow with a uniform imposed heat flux is analyzed the value of Nu_D tends toward the fully developed one as x increase. Correlations suitable for developing flows give the value of Nu_D at each value of the axial coordinate. For liquid metals an appropriate correlation belonging to this set is the Ching-Jen and Chiou correlation suggested in [39] that provides values for the local, Eq.(5.16), and the mean Nusselt number, Eq.(5.17), respectively.

$$\frac{\langle Nu \rangle}{Nu_{fd}} = 1 + \frac{2.4}{x/2r_i} - \frac{1}{(x/2r_i)^2} \tag{5.16}$$

$$\frac{\langle Nu \rangle_L}{Nu_{fd}} = 1 + \frac{7}{L/2r_i} + \frac{2.8}{L/2r_i} \ln\left(\frac{L/2r_i}{10}\right) \tag{5.17}$$

$$\tag{5.18}$$

The above equations holds for a uniformly heated duct at $Pr < 0.03$, $Pe > 500$, and $L/2ri > 2$. Nu_{fd} is the fully developed Nusselt number. that has been evaluated with the correlation of Skupinski [15] instead of using the one proposed by [39].

In Fig.5.8a the circumferentially averaged Nusselt numbers resulting from the simulation at $Pe = 2510$, $\lambda^* = 1.4$, $r^* = 1.5$ and $L/D = 30$ are compared with the local Nusselt numbers provided by the Ching-Jen and Chiou correlation. As it can be seen the two values are extremely different and, in particular, while the value computed from Eq.(5.16) is tending to the fully developed one, the circumferentially averaged Nusselt number of the simulation goes below the fully developed one and seems not to tend to any constant value.

This behavior is found again by analyzing the effect of the variability of Pe (Fig.5.9a) and L/D (Fig.5.9b) on the circumferentially averaged Nusselt number. Again in these figures it can be seen that the $\langle Nu \rangle$ becomes also lower than those for the fully developed flow, as already found for example by [40] for a sinusoidally heat flux distribution along a cylindrical fuel element.

Moreover, observing these figures it can be noticed that the Nusselt number increases with increasing Pe (Fig.5.9a), because of the enhanced turbulence intensity, and decreases with increasing L/D for the same Pe number because of the lower temperature gradients at the same $\tilde{x}$ (Fig.5.9b).

This last phenomenon is due to the fact that, when L is greater the same value of $\tilde{x}$ correspond to a bigger value of the dimensional axial coordinate x. Thus the fluid when L/D increase reach the same $\tilde{x}$ after having covered a bigger distance, thus having an increased available developing length. This effect is more accentuated at low L/D, while the curves tend to collapse together at higher length-to-diameter ratios.

Despite the fact that the circumferentially averaged Nusselt numbers resulting from the simulations with the non-uniform imposed heat flux (2.1) are quite different

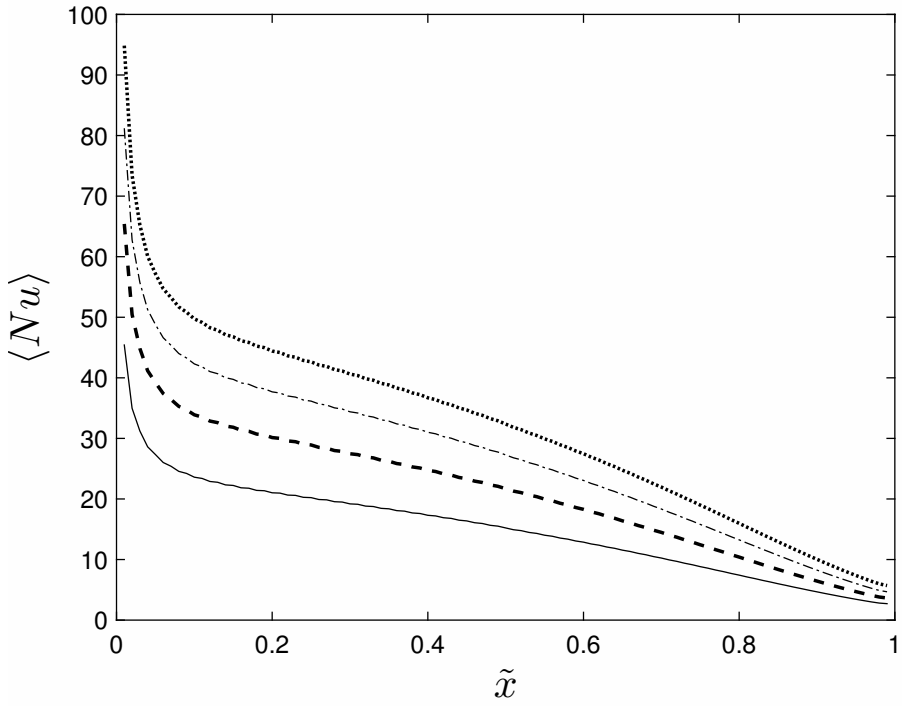

(a)

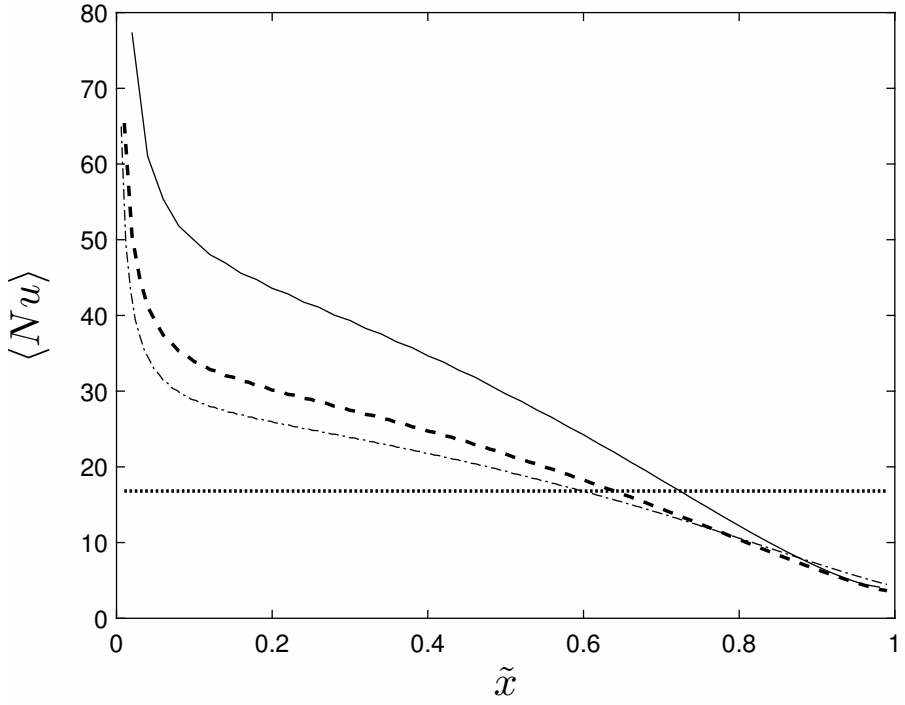

(b)

Figure 5.9: Profiles of $\langle Nu \rangle$ at $\lambda^* = 1.4$, $r^* = 1.5$ and
a) $L/D = 30$, $Pe = 1255$ (solid line), $Pe = 2510$ (thicker dashed line), $Pe = 3766$ (dashed-dotted), $Pe = 5021$ (dotted)
b) $Pe = 2510$, $L/D = 10$ (solid line), $L/D = 30$ (thicker dashed line), $L/D = 50$ (dashed-dotted), evaluated with Skupinski correlation (4.1) (dotted)

from the local Nusselt numbers derived from Eq.(5.16), the global Nusselt numbers resulting from the same simulations (Fig.5.8b) are within the range of ±10% of the correlation (5.17).

This is only due to the averaging procedure that flattens the local differences. Moreover, the error between the computed global Nu and the correlation increases with increasing Pe number and also with increasing L/D ratio (See Tab.5.3).

Keeping in mind that in a central receiver L/D can reach values up to 500, this phenomenon creates doubts about the applicability of the correlation. Indeed, as previously underlined all the available correlations for thermally developing temperature fields are based on the assumption that the flow will reach a fully developed condition as x increase. This is not true when a longitudinally varying heat flux is imposed.

The fully developed condition is supposed to be reached at lower x with increasing Pe and it is supposed to involve most of the pipe length with increasing L/D. Thus the difference between the global Nusselt number in a pipe with longitudinally varying imposed heat flux and the one predicted by the correlations is greater with increasing Pe number and also with increasing L/D ratio.

Table 5.3: Percentage error between the Nusselt numbers calculated with Eq.(5.15) and from the simulations with $Pe = 2510$, $\lambda^* = 1.4$, $r^* = 1.5$ and different L/D

$L/D = 10$	$L/D = 30$	$L/D = 50$
2,3%	5,4%	7,9%

Moving forward in the parametric analysis the influence of Pe on the dimensionless inner, outer and bulk fluid temperatures is shown in Fig.5.10a. The non-dimensional temperatures decrease with increasing Peclét numbers. The decrease is more pronounced at low Pe and the non-dimensional temperatures seem to tend to an asymptotic value with increasing Pe. This is always caused by the increase of turbulent mixing with Pe.

Indeed, in Fig.5.10b the variation of the cross-section averaged Pr_t along the axial coordinate at different Peclét numbers is shown and, as expected, Pr_t decreases with increasing Pe showing that α_t is increasing together with the turbulence mixing. Moreover, except for the lowest value of Pe, Pr_t almost attains a constant value over the tube's length and seems to tend to a common value with increasing Pe.

Fig.5.12 illustrates the profiles of the circumferentially averaged Pr_t versus the axial coordinate for different length-over-diameter ratios. The values decrease with increasing L/D. The decrease is more accentuated for low L/D. The values remain always higher than those for the fully developed case, i.e. for a longitudinally constant heat flux, except close to the outlet section, where, for high L/D ratios, they can go slightly beyond the fully developed ones.

Fig.5.11a shows the profiles of θ_{iw} and θ_{ow} along the tube's axis at different angular positions. The maximum temperature values can be seen for $\varphi = 180°$, i.e. where also the heat flux has its peak value, as shown in Fig.2.3a. Due to the decrease of the longitudinal applied heat flux, the temperatures also decrease starting from a certain axial position greater that $\tilde{x} = 0.5$. It is interesting to

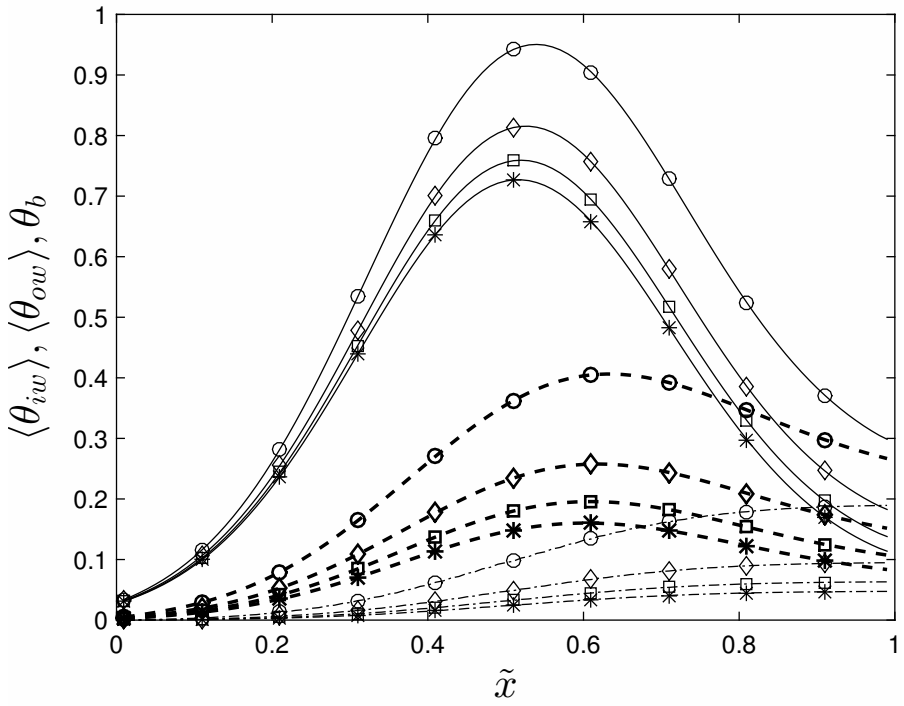

(a)

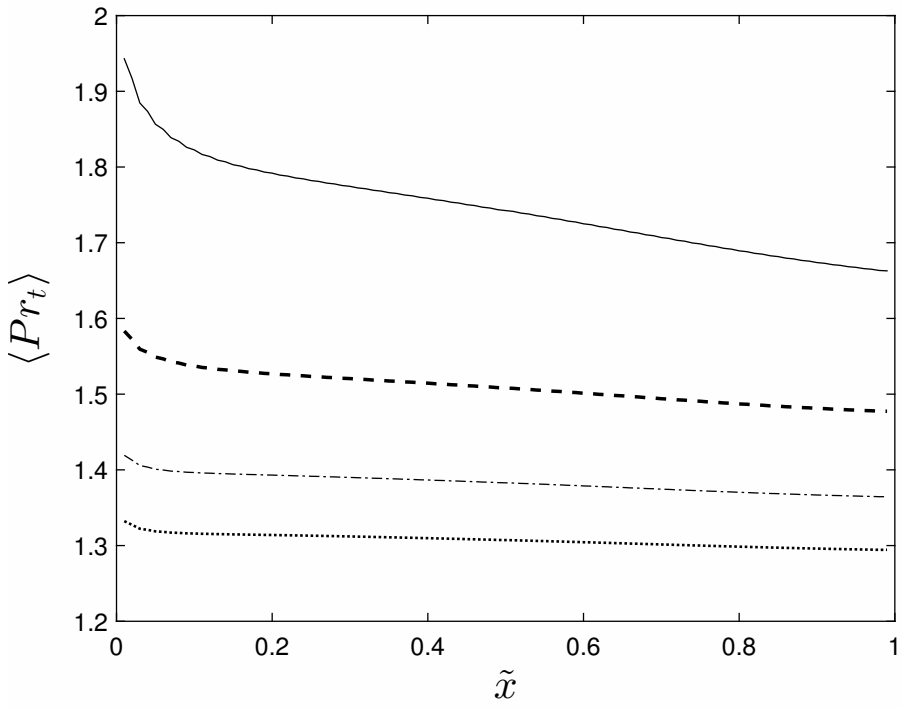

(b)

Figure 5.10: Results at $L/D = 30$, $\lambda^* = 1.4$, $r^* = 1.5$
a) Profiles of θ_{ow} (solid line), θ_{iw} (thicker dashed line), θ_b (dashed-dotted) at $Pe = 1255$ (o), $Pe = 2510$ ($\diamond$), $Pe = 3766$ ($\square$), $Pe = 5021$ ($*$)
b) Profiles of Pr_t at $Pe = 1255$ (solid line), $Pe = 2510$ (thicker dashed line), $Pe = 3766$ (dashed-dotted), $Pe = 5021$ (dotted)

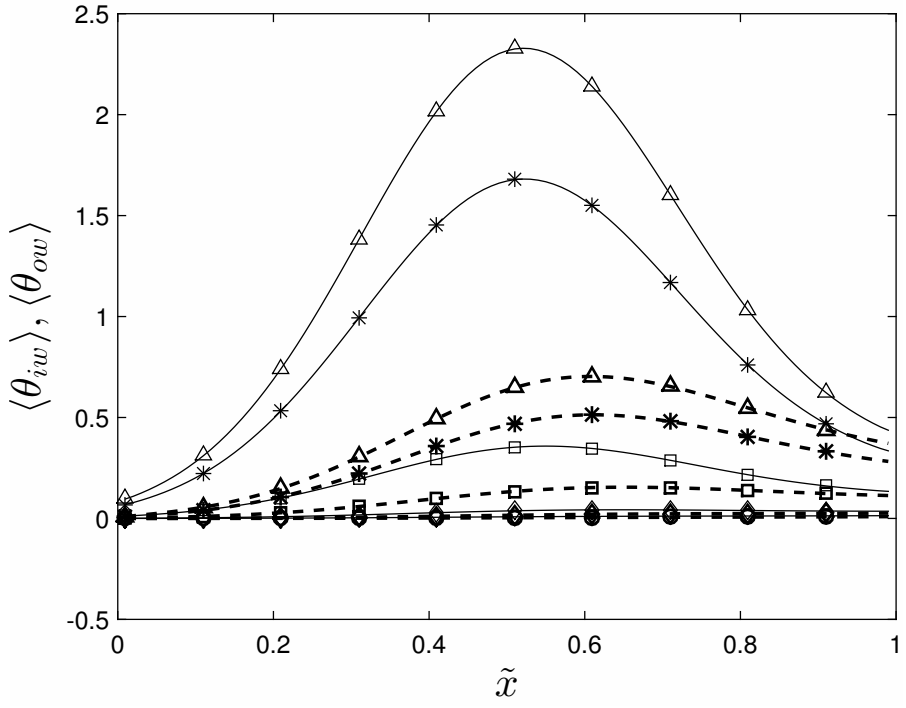

(a)

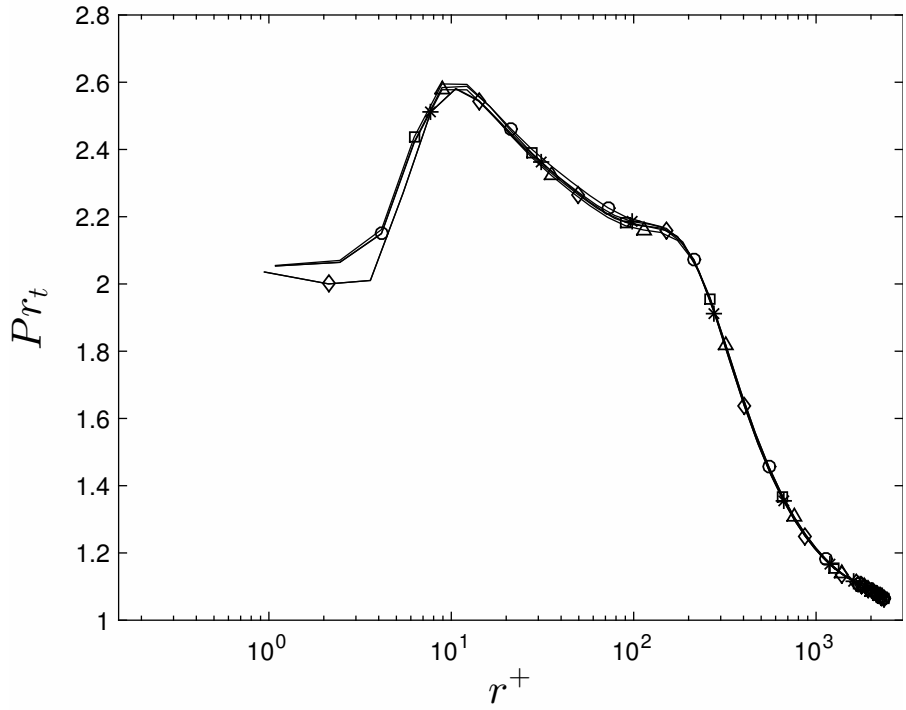

(b)

Figure 5.11: Results at $\lambda^* = 1.4$, $r^* = 1.5$, $L/D = 30$ and $Pe = 2510$ for different φ; $\varphi = 0°$ (o), $\varphi = 45°$ ($\diamond$), $\varphi = 90°$ ($\square$), $\varphi = 135°$ ($*$), $\varphi = 180°$ ($\triangle$)
a) Profiles of θ_{ow} (solid line), θ_{iw} (thicker dashed line), θ_b (dashed-dotted)
b) Profiles of Pr_t

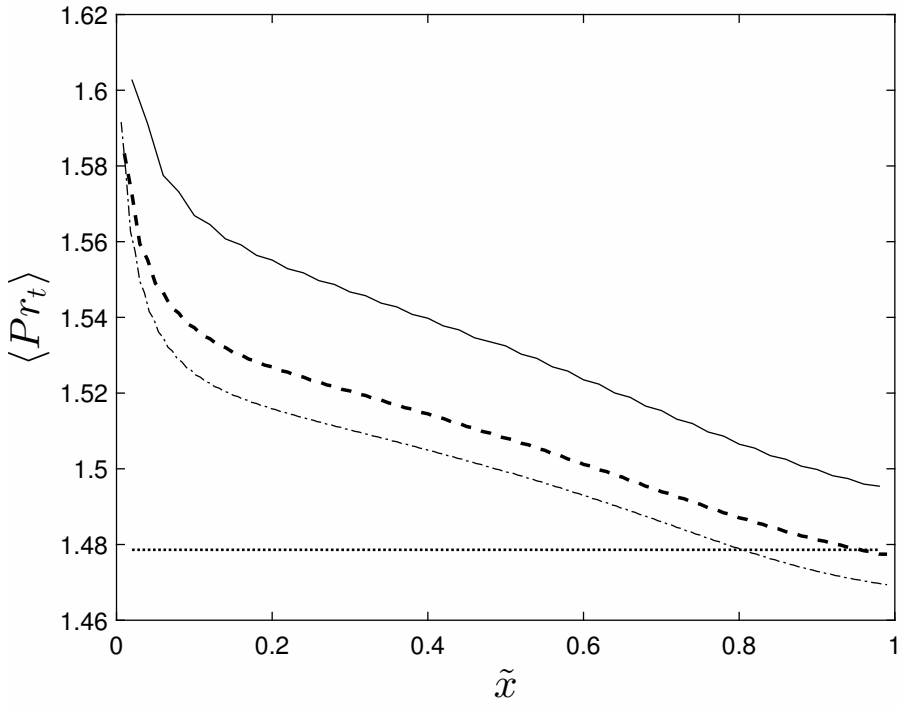

Figure 5.12: Profiles of Pr_t for $\lambda^* = 1.4$, $r^* = 1.5$, $Pe = 2510$ and $L/D = 10$ (solid line), $L/D = 30$ (thicker dashed line), $L/D = 50$ (dashed-dotted), thermally fully developed flow with circumferentially uneven imposed heat flux "B" (dotted)

noticed that at $\varphi = 0°$ and $\varphi = 45°$ the decrease of the temperature is not present. Here, where the outer wall is adiabatic, the temperatures always slightly increase due to the circumferential conduction in the wall and in the fluid.

From Fig.5.11b, which shows the profiles of Pr_t at different angular coordinates on a section along the tube's axis, it can be noticed how the values calculated with the k_θ-ε_θ model are almost independent from the angular position. This behavior is not surprising since it has been already detected in Sec.5.1 Fig.4.9.

Considering the results found within Chapter 4 the Manservisi k_θ-ε_θ model is the more reliable one for computing the temperature field of liquid metals in a turbulent pipe, thus all the conclusions deduced within this section are referred to simulations computed adopting this model.

However, simulations with $Pe = 2510$, $\lambda^* = 1.4$, $r^* = 1.5$ and $L/D = 30$ have been done adopting the different approaches to compute the turbulent Prandtl number presented in Sec.3.1.2, in order to assess the variability of the results with the model adopted.

Fig.5.13 shows a comparison between the calculated values of Pr_t using the Manservisi k_θ-ε_θ model, the Kays correlation (3.18) and the Cheng and Tak correlation (3.17). As expected Eq.(3.17) strongly overestimates the value of the turbulent Prandtl number with respect to the others while a constant Pr_t of 0.85 is very low if compared with the others.

The dimensionless inner, outer and bulk fluid temperatures (Fig5.14a) and the circumferentially averaged Nusselts (Fig.5.14b) are dependent on the value of Pr_t, a greater Pr_t means higher dimensionless temperatures and lower Nusselts. This

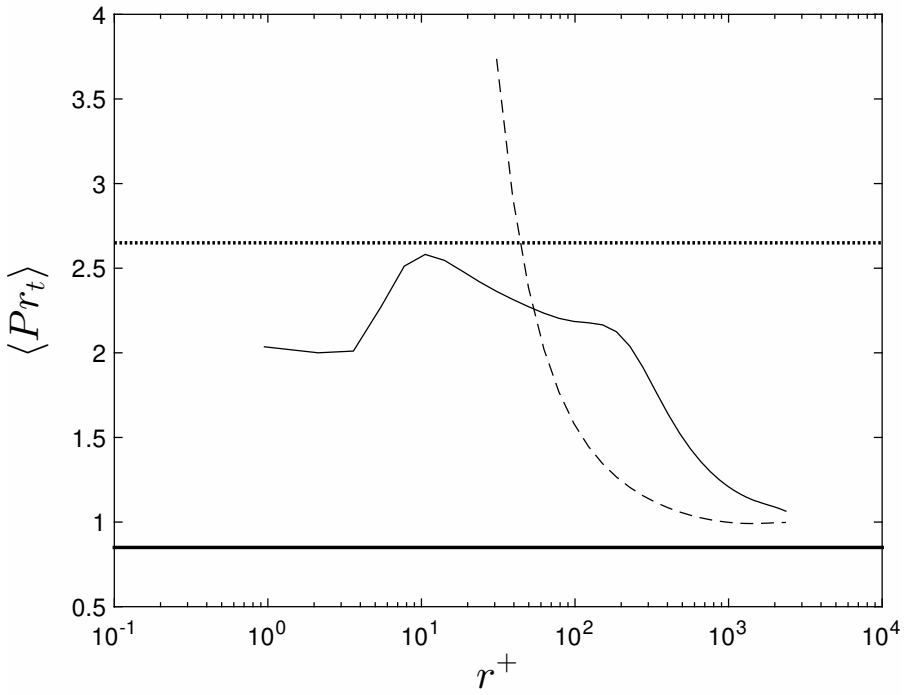

Figure 5.13: Profiles of Pr_t for $\lambda^* = 1.4$, $r^* = 1.5$, $Pe = 2510$, $L/D = 30$, $\tilde{x} = 0.5$ computed with k_θ-ε_θ (solid line), Kays correlation Eq.(3.18) (dashed line), Chang and Tak correlation Eq.(3.17) (dotted), $Pr_t = 0.85$ (thicker solid line)

follows exactly what was found while assessing the performances of the different thermal turbulence models in Chapter 4.

In Tab.5.4 Nusselt numbers from the simulations adopting different thermal turbulence models are reported together with their percentage difference from the Nusselt number resulting from the simulation adopting the Manservisi k_θ-ε_θ model. The variability of Nusselt numbers with changing models increases with $\tilde{x}$, this is partially due to the fact that Nu is lowering thus the same absolute differences between the values represent bigger percentages at higher $\tilde{x}$.

The values of $\Delta\langle Nu \rangle_L\%$ can be compared with the one reported in Tab.5.1 referring to simulations at the same Pe but with a longitudinally constant and circumferentially varying imposed heat flux. It can be noticed that here (Tab.5.4) the value computed adopting k_θ-ε_θ model is closer to the one computed through the Chang and Tak correlation than to the one computed adopting the Kays correlation. This is in contrast with the results found in Tab.5.1.

The reason has to be found in the fact that the Pr_t computed by the k_θ-ε_θ is on average greater here where a developing temperature field with a longitudinally and circumferentially uneven imposed heat flux is considered, with respect to the one calculated for a developed temperature field with a heat flux variable over the circumferential direction. Thus, the greater Pr_t happens to be closer to the very high one provided by the Cheng and Tak correlation.

In conclusion the main key points that can be deduced from the results illustrated are:

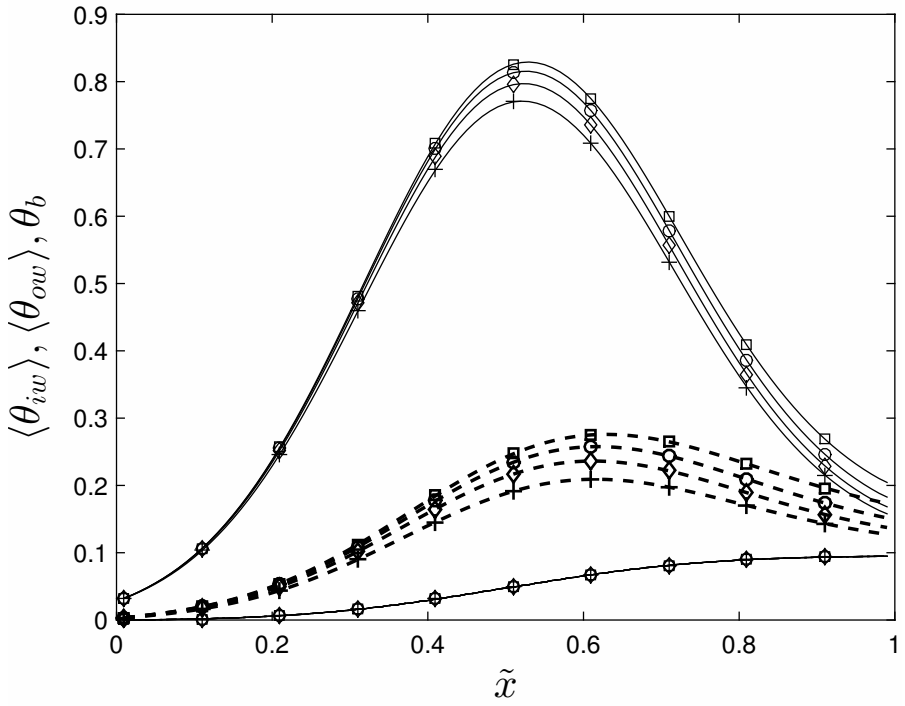

(a)

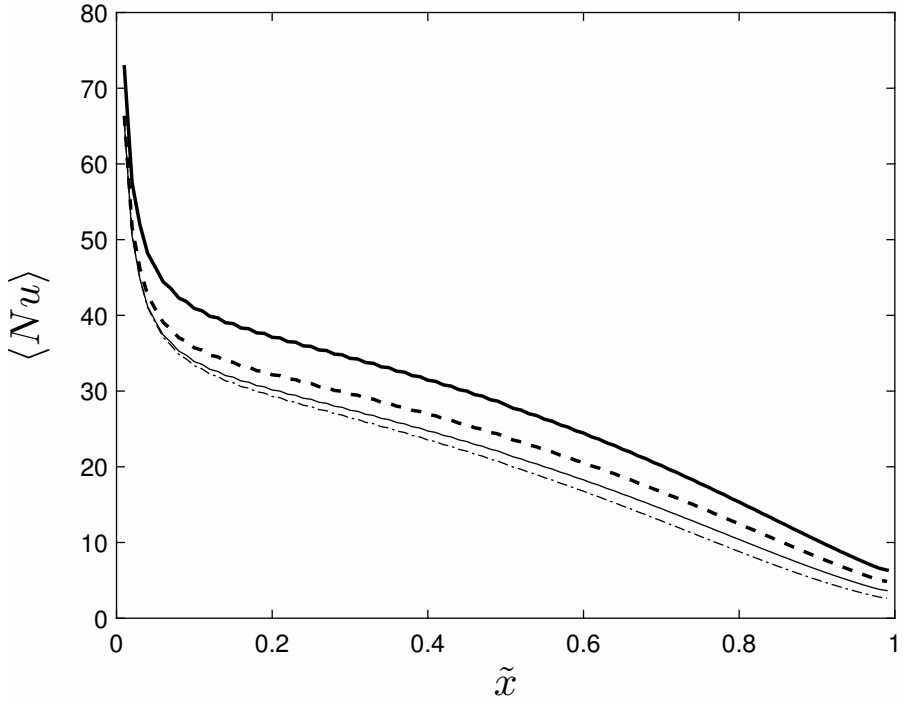

(b)

Figure 5.14: Profiles at $\lambda^* = 1.4$, $r^* = 1.5$, $Pe = 2510$, $L/D = 30$ of
a) θ_{ow} (solid line), θ_{iw} (thicker dashed line) and θ_b (dashed-dotted) computed with k_θ-ε_θ (o), Kays correlation Eq.(3.18) ($\diamond$), Chang and Tak correlation Eq.(3.17) ($\square$), $Pr_t = 0.85$ (+)
b) $\langle Nu\rangle$ computed with k_θ-ε_θ (solid line), Kays correlation Eq.(3.18) (thicker dashed line), Chang and Tak correlation Eq.(3.17) (dashed-dotted), $Pr_t = 0.85$ (thicker solid line)

- The peculiar profile of the heat flux presents on a central receiver tube prevents the flow inside from reaching the standard thermally fully developed condition with the implications of Eq.3.29. Thus, the local Nusselt number provided by suitable correlations is different from the circumferentially averaged one computed from the simulations.
- It seems that global correlations are, however, suitable to predict a quite accurate value for the global Nusselt number. Even though it has to be noticed that the percentage error between the global Nusselt numbers computed from the correlation and from the simulations increased with Pe and L/D.
- The dimensionless outer wall fluid temperature is affected by Pe, λ^* and r^* while the dimensionless inner and bulk fluid temperatures are affected by Pe and not by λ^* or r^*, at list for the range here investigated.

Table 5.4: Nusselt numbers obtained adopting different Pr_t models with $\lambda^* = 1.4$, $r^* = 1.5$, $Pe = 2510$, $L/D = 30$ and percentual differences between them and the Nu_D resulting from simulations adopting Manservisi k_θ-ε_θ.

	k_θ-ε_θ	Eq. (3.18)	Eq. (3.17)	$Pr_t = 0.85$
$\langle Nu \rangle$ at $\tilde{x} = 0,25$	28,92	31,00	27,97	35,91
$\Delta Nu\%$ from k_θ-ε_θ	−−	7,20%	3,40%	24,17%
$\langle Nu \rangle$ at $\tilde{x} = 0,50$	21,69	23,93	20,35	28,18
$\Delta Nu\%$ from k_θ-ε_θ	−−	10,33%	6,59%	29,94%
$\langle Nu \rangle$ at $\tilde{x} = 0,75$	12,44	14,59	10,81	17,77
$\Delta Nu\%$ from k_θ-ε_θ	−−	17,28%	15,08%	42,85%
$\langle Nu \rangle_L$	21,30	23,30	20,14	27,29
$\Delta Nu\%$ from k_θ-ε_θ	−−	9,39%	5,76%	28,12%

5.3 Discretization errors assessment

The Grid Convergence Index GCI method [41] has been used to quantify the numerical discretization errors. The method has been used referring to a representative case computed through AKN and k_θ-ε_θ models with $Pe = 2510$, $\lambda^* = 1.4$, $r^* = 1.5$, $L/D = 30$ and the longitudinally and circumferentially uneven imposed heat flux (2.1).

The solution has been computed for three different grids with a refinement ratio $r_{ij} = h_i/h_j$ of approximately 1.3. Two characteristic variables, namely the circumferentially and longitudinally averaged Nusselt number and the friction factor have been selected as representative variables for the problem under consideration.

Table 5.5: Discretization errors using the GCI method. The results refer to simulations computed with AKN and k_θ-ε_θ models, $Pe = 2510$, $\lambda^* = 1.4$, $r^* = 1.5$, $L/D = 30$, longitudinally and circumferentially uneven imposed heat flux from Eq.(2.1).

$N_1,\ N_2,\ N_3$	1 274 400 ; 579908 ; 267628	
	$\langle Nu \rangle_L$	C_f
ϕ_1	21,3128	$4{,}6691 \cdot 10^{-3}$
ϕ_2	21,2984	$4{,}6697 \cdot 10^{-3}$
ϕ_3	21,2929	$4{,}6720 \cdot 10^{-3}$
p	3,53	5,73
ϕ_{ext}^{21}	21,322	$4{,}669 \cdot 10^{-3}$
e_{ext}^{21}	0,44%	0,011%
GCI_{fine}^{21}	0,055%	0,004%

$$h = \left[\frac{1}{N} \sum_{i=1}^{N} (\Delta V_i) \right]^{1/3}$$

$$p = \frac{1}{\ln(r_{21})} \left| \ln \left| \frac{\phi_3 - \phi_2}{\phi_2 - \phi_1} \right| + q(p) \right|$$

$$q(p) = \ln \left(\frac{r_{21}^p - s}{r_{32}^p - s} \right) \quad ; \quad s = 1 \cdot sgn \left(\frac{\phi_3 - \phi_2}{\phi_2 - \phi_1} \right)$$

The detailed algorithm to compute the GCI is reported in [41], the resulting values are summarized in Table 5.5. The quantity ϕ_i refers to the calculated variable value, while the index $i = 1; 2; 3$ refers to the fine, medium and coarse grid respectively.

The apparent order of the discretization method is denoted with p. The quantities ϕ_{ext}^{21} and e_{ext}^{21} indicates the extrapolated values from the medium and fine grids of the calculated variable and the error, respectively.

$$\phi_{ext}^{ij} = \frac{r_{ij}^p \phi_j - \phi_i}{r_{ij}^p - 1}$$

$$e_a^{ij} = \left| \frac{\phi_j - \phi_i}{\phi_j} \right| \quad ; \quad e_{ext}^{ij} = \left| \frac{\phi_{ext}^{ji} - \phi_i}{\phi_{ext}^{ji}} \right|$$

$$GCI_{fine}^{21} = \frac{1.25\, e_a^{21}}{r_{21}^p - 1}$$

Both $\langle Nu \rangle_L$ and C_f show monotonic convergence. The numerical uncertainty in the fine-grid solution is given by the GCI_{fine}^{21} values and is therefore very small.

Chapter 6

Conclusions

The heat transfer in a central solar receiver tube operated with a liquid metal having a representative Prandtl number of 0.025 has been numerically analyzed.

First of all the operation of a central receiver system have been outlined (Sec.1.2), in particular the heat flux imposed on the receiver surface has been analyzed (Sec.2.1) deriving a function modeling the imposed heat flux on a single tube (Eq.(2.1)).

Since the resulting heat flux distribution is strongly uneven both circumferentially and longitudinally, the applicability of Nusselt correlations derived for a uniform thermal boundary condition is questionable.

The analysis has been then focused on comparisons between the numerical data computed with uneven imposed heat flux and the data derived from the correlations suitable for liquid metals, i.e. the Skupinski correlation for fully developed flows Eq.(4.1) and the Ching-Jen and Chiou correlation for developing flows Eq.(5.14).

Because the Reynolds analogy, that assumes a constant turbulent Prandtl number close to unity, does not apply to liquid metals, a crucial point for the RANS analysis has been to follow a suitable approach of computing the turbulent heat flux.

Different approaches have been analyzed (Sec.3.1.2) and assessed, in particular a recently proposed k_θ-ε_θ model specifically calibrated for liquid metals has been implemented and coupled to the solver (FLUENT v.15). Besides the equations for the turbulent kinetic energy and its dissipation rate, two additional ones, namely for the temperature variance and its dissipation rate, have been solved, in order to locally calculate the turbulent thermal diffusivity.

The performances of the different approaches of computing the turbulent heat flux have been evaluated by comparisons against DNS data (Sec.4.1), suitable Nusselt correlations (Sec.4.2), semi-analytical solutions founded in [6], [7] (Sec.4.3).

The k_θ-ε_θ model shows a better agreement with the DNS data and the Skupinski correlation with respect to the other followed approaches, i.e. the Kays correlation (3.18), the Cheng and Tak correlation (3.17) and a fixed $Pr_t = 0.85$. Therefore it has been chosen to compute the simulations presented in Chapter 5.

Simulations with a circumferentially uneven and longitudinally constant heat flux have been performed and the results have been presented in Sec.5.1. From the results it can be inferred that, as already shown in literature for medium-to-high Prandtl number fluids, also for liquid metals Nusselt number correlations for fully developed flow in uniformly heated tubes can be applied to fully developed cases

having a circumferentially non-uniform heat flux imposed. However, it must be emphasized that these correlations are not suited to evaluate the wall temperature.

Finally in Sec.5.2, the conjugate heat transfer in a solar tower receiver tube operated with liquid metals has been analyzed for different values of the governing parameters, i.e. the solid-to-fluid thermal conductivity, the wall thickness ratio, the Peclét number and the diameter-to-length ratio.

The values have been chosen such as to be useful for engineering applications. Detailed results for the inner and outer wall temperature, fluid bulk temperature, Pr_t and Nusselt number have been reported.

The circumferentially averaged Nusselt numbers along the tube's axis and the circumferentially and longitudinally averaged ones have been compared to those obtained with a correlation valid for developing flows within a uniformly heated pipe; Eq.(5.14),(5.15).

Although the

first differ substantially from the correlation's ones, the second are within a $\pm 10\%$ range of the correlation. This is, however, only due to the averaging procedure that cancels out the local differences.

In particular it must be noticed that the difference between the global Nusselt number computed from the simulations and the one provided by the correlation increases with Pe and L/D.

This work has been carried out in collaboration with the KALLA team of the Institute for Nuclear and Energy Technologies IKET at KIT[1], where the SOMMER facility is under construction. Speaking of the design of SOMMER it can be concluded that on one hand the wall temperature cannot be derived from the available correlations.

On the other hand Eq.(5.15) can be adopted to evaluate the overall heat transfer coefficient in the receiver tubes. This might not be true when the design of a bigger central receiver system is carried on. In this case L/D can be greater than the range here analyzed and further simulations are needed to investigate the influence of this parameter in a broader range.

Future works must focus on carrying on experiments where an uneven heat flux is imposed on a liquid metal pipe flow. This would be useful in order to get data to better assess the performance of the Manservisi k_θ-ε_θ model in simulating these kind of flows.

[1]Karlsruhe Institute of Technology

Appendix A

Attached listings

Listing A.1: UDF function for the heat flux boundary condition.

```
#include <udf.h>
#include <math.h>

DEFINE_PROFILE(HEAT_FLUX_GAUSS05, t, i)
{
face_t f;
real x[ND_ND];
real z;
real ax;
real qmax = 3.8764E5; /* Maximum Heat Flux */
real R = 0.0075; /* Radius of the pipe */
real L = 0.30 /* Length of the pipe */
real sigmaG = L/5;
real nuG = L/2;

begin_f_loop(f,t)
{
F_CENTROID(x,f,t);
z=x[2];
ax = x[0];
F_PROFILE(f,t,i) = -((qmax/(sigmaG*sqrt(2*PI)))*exp(-SQR
   (ax-nuG)/(2*SQR(sigmaG))))*(z/R);
}
end_f_loop(f,t)
} /* end of function */
```

Listing A.2: UDF function of Kays Pr_t correlation.

```
#include "udf.h"

real ni(cell_t c, Thread *t)
{ return C_MU_L(c,t)/C_R(c,t); }

real alpha(cell_t c, Thread *t)
{ return C_K_L(c,t)/(C_R(c,t)*C_CP(c,t)); }

real Pr(cell_t c, Thread *t)
{ return ni(c,t)/alpha(c,t); }

DEFINE_PRANDTL_T(pr_t_KAYS,c,t)
{ return 0.85+0.7/(Pr(c,t)*C_MU_T(c,t)/C_MU_L(c,t)); }
```

Listing A.3: UDFs to couple to FLUENT v.15 in order to make available the implementation of Manservisi k_θ-ε_θ turbulence model

```
1  /*
2   * UDF for the turbulence model of Manservisi-Menghini
       according to the following papers:
3   * [1] Abe K., Kondoh T., Nagano Y. (1994) A new
       turbulence model for predicting fluid flow and heat
       transfer in separating and reattaching flows - I.
       Flow field calculations, Int. J. Heat Mass Transfer,
        37(1), 139-151
4   * [2] Abe K., Kondoh T., Nagano Y. (1995) A new
       turbulence model for predicting fluid flow and heat
       transfer in separating and reattaching flows - I.
       Thermal field calculations, Int. J. Heat Mass
       Transfer, 38(8), 1467-1481
5   * [3] Manservisi S. Menghini F. (2014) A CFD four
       parameter heat transfer turbulence model for
       engineering applications in HLM, In. Jou. of Heat
       and Mass Transfer, 69, 312-326
6   * [4] Manservisi S. Menghini F. (2014) Triangular rod
       bundle simulations of a CFD k-e-kt-et heat transfer
       turbulence model for heavy liquid metals, Nuclear
       engineering and Design 273 (2014) 251-270
7  */
8
9  /*  This is the implementation for ANSYS Fluent of the
      turbulent heat transfer model presented in article
      [3] and [4].
10   This implementation concerns only the thermal field,
       you can use it with any k-e model.
11   However the constants are setted for Pr=0.025 starting
        from a flow field computed using the turbulence
       model (AKN) presented in article [1].
12   Thus the results obtained using a flow field computed
       using other turbulence models might be not
       trustworthy.
13  */
14
15 /* Loading flow specification */
16 #include <udf.h>
17 #include <math.h>
18
19 /* Turbulence model constants for K_t and TDR_t*/
20 #define SIG_KT 1.4
21 #define SIG_DT 1.4
22 #define Cp1 0.925
23 #define Cp2 0.9
```

```
24 #define Cd1 1
25 #define C_EMME 0.3
26 #define C_LAMBDA 0.1
27 #define Prt_inf 0.9
28
29 typedef enum
30 {
31  KT = 0,
32  TDR_KT = 1,
33  N_REQUIRED_UDS
34 }UDS_Scalars;
35
36 typedef enum
37 {
38  TAU_U = 0,
39  TAU_T = 1,
40  P_KT = 2,
41  ALPHA_T = 3,
42  PR_T = 4,
43  P_TKE = 5,
44  SOURCE_Kt = 6,
45  SOURCE_TDR_KT = 7,
46  MUt = 8,
47  tau_lT = 9,
48  N_REQUIRED_UDM
49 }UDM_Memory;
50
51 #define C_Kt(c,t) C_UDSI(c,t,KT)
52 #define C_TDR_KT(c,t) C_UDSI(c,t,TDR_KT)
53 #define C_PKT(c,t) C_UDMI(c,t,P_KT)
54
55 /*
    **********************************************************************

56          DEFINITIONS USEFUL QUANTITIES
57 **********************************************************************
    */
58
59 real ni(cell_t c, Thread *t)
60 { return C_MU_L(c,t)/C_R(c,t); }
61
62 real alpha(cell_t c, Thread *t)
63 { return C_K_L(c,t)/(C_R(c,t)*C_CP(c,t)); }
64
65 real Pr(cell_t c, Thread *t)
66 { return ni(c,t)/alpha(c,t); }
67
```

```
68 real Re_d(cell_t c, Thread *t)
69 { return C_WALL_DIST(c,t)*pow(C_D(c,t)*ni(c,t),0.25)/ni(
     c,t); }
70
71 real Re_t(cell_t c, Thread *t)
72 { return SQR(C_K(c,t))/(ni(c,t)*C_D(c,t)); }
73
74 real tau_u(cell_t c, Thread *t)
75 { return C_K(c,t)/C_D(c,t); }
76
77 real tau_t(cell_t c, Thread *t)
78 { return C_Kt(c,t)/C_TDR_KT(c,t); }
79
80 real R(cell_t c, Thread *t)
81 { return tau_t(c,t)/tau_u(c,t); }
82
83 real C_PTKE(cell_t c, Thread *t)
84 { return C_UDMI(c,t,MUt)/C_R(c,t) * SQR(
     C_STRAIN_RATE_MAG(c,t)); }
85
86 /*
     ************************************************************

87         DAMPING FUNCTIONS
88 ************************************************************
     */
89
90 real f_1a(cell_t c, Thread *t)
91 { return (1.0-exp(-0.0714*Re_d(c,t))); }
92
93 real f_2a(cell_t c, Thread *t)
94 { return (1.0-exp(-(0.0526*Re_d(c,t))*sqrt(Pr(c,t)))); }
95
96 real f1t(cell_t c, Thread *t)
97 { return (f_1a(c,t)*f_2a(c,t)); }
98
99 real B1t(cell_t c, Thread *t)
100 { return (tau_u(c,t)*Prt_inf); }
101
102 real f_2ao(cell_t c, Thread *t)
103 { return (f1t(c,t)*exp(-4E-6*SQR(Re_t(c,t)))); }
104
105 real f_2bo(cell_t c, Thread *t)
106 { return (f1t(c,t)*exp(-2.5E-5*SQR(Re_t(c,t)))); }
107
108 real f2tB2t(cell_t c, Thread *t)
109 { return tau_u(c,t)*(f_2ao(c,t)*(2.0*R(c,t)/(R(c,t)+
```

```
   C_EMME))+f_2bo(c,t)*sqrt(2*R(c,t)/Pr(c,t))*(1.3/(sqrt
   (Pr(c,t))*pow(Re_t(c,t),0.75)))); }
110
111 real Cd2(cell_t c, Thread *t)
112 { return SQR(1-exp(-0.1754*Re_d(c,t)))*(1.9*(1-0.3*exp
   (-0.0237*SQR(Re_t(c,t))))-1); }
113
114 /*
   ************************************************************

115         DEFINE UDS SOURCES
116 ************************************************************
   */
117
118 DEFINE_SOURCE(KT_src,c,t,dS,eqn)
119 {
120  real source = C_R(c,t) * (C_PKT(c,t) - C_TDR_KT(c,t));
121  C_UDMI(c,t,SOURCE_Kt)=source;
122  dS[eqn] = 0;
123  return source;
124 }
125
126
127 DEFINE_SOURCE(TDR_KT_src_mans,c,t,dS,eqn)
128 {
129  real source1 = (C_TDR_KT(c,t)/C_Kt(c,t))*(Cp1*C_PKT(c,t
   )-Cd1*C_TDR_KT(c,t));
130  real source2 = (C_TDR_KT(c,t)/C_K(c,t))*(Cp2*C_PTKE(c,t
   )-Cd2(c,t)*C_D(c,t));
131  real source = C_R(c,t)*(source1 + source2);
132  C_UDMI(c,t,SOURCE_TDR_KT)=source;
133  dS[eqn] = C_R(c,t)*((Cp2*C_PTKE(c,t)-Cd2(c,t)*C_D(c,t))
   /C_K(c,t)+(Cp1*C_PKT(c,t))/C_Kt(c,t)-2.0*C_TDR_KT(c,
   t)*(Cd1/C_Kt(c,t)));
134  return source;
135 }
136
137 /*
   ************************************************************

138       DEFINE UDS FLUXES AND DIFFUSIVITY
139  ************************************************************
   */
140 DEFINE_DIFFUSIVITY(keMANS_diffusivity,c,t,eqn)
141 {
142   switch(eqn)
143   {
```

```
144     case KT:  return C_R(c,t)*(C_UDMI(c,t,ALPHA_T)/
           SIG_KT + alpha(c,t)); break;
145     case TDR_KT:  return C_R(c,t)*(C_UDMI(c,t,ALPHA_T)/
           SIG_DT + alpha(c,t)); break;
146     default: return 0;
147   }
148 }
149
150 DEFINE_UDS_FLUX(UDS_flux_keMANS, f, t, eqn)
151 {
152   switch(eqn)
153     {
154     case KT: return F_FLUX(f,t); break;
155     case TDR_KT: return F_FLUX(f,t); break;
156     default: return 0;
157     }
158 }
159
160 /*
    ************************************************************

161         ADJUST FUNCTIONS
162 ************************************************************
    */
163
164 DEFINE_ADJUST(adjust_keMANS,d)
165 {
166   Thread *t;
167   cell_t c;
168   real tau_lu, tau_lt;
169   real term1, term2, term3;
170
171   thread_loop_c(t,d)
172     if (FLUID_THREAD_P(t))
173     {
174       begin_c_loop(c,t)
175         {
176           C_UDMI(c,t,TAU_U) = tau_u(c,t);
177           C_UDMI(c,t,TAU_T) = tau_t(c,t);
178           tau_lt = f1t(c,t)*B1t(c,t) + f2tB2t(c,t);
179           C_UDMI(c,t,tau_lT)=tau_lt;
180           C_UDMI(c,t,ALPHA_T) = C_LAMBDA*C_K(c,t)*tau_lt
                ;
181           C_UDMI(c,t,P_TKE) = C_PTKE(c,t);
182
183           if ( NULL != THREAD_STORAGE(t,SV_T_G) )
184             { C_UDMI(c,t,P_KT) = C_UDMI(c,t,ALPHA_T) *
```

```
                NV_MAG2(C_T_G(c,t)); }
185           else
186           {
187             Message("\nAllocated temperature gradients!\
                  n");
188             MD_Alloc_Storage_Vars(d, SV_T_RG, SV_T_G,
                  SV_NULL);
189             C_UDMI(c,t,P_KT) = C_UDMI(c,t,ALPHA_T) *
                  NV_MAG2(C_T_G(c,t));
190           }
191           C_UDMI(c,t,PR_T) = C_UDMI(c,t,MUt)/C_R(c,t)/
                C_UDMI(c,t,ALPHA_T);
192         }
193       end_c_loop(c,t)
194       }
195 }/* end of function */
196
197 /*
    ***************************************************************

198         DEFINE TURBULENT PRANDTL NUMBER
199 ***************************************************************
    */
200
201 DEFINE_PRANDTL_T(pr_t_MANS,c,t)
202 { return C_UDMI(c,t,PR_T); }
203
204
205 /*
    ***************************************************************

206          BOUNDARY CONDITIONS
207 ***************************************************************
    */
208
209 DEFINE_PROFILE(TDR_KT_BC_CHF, t, i)
210 {
211 face_t f;
212 cell_t c0;
213 Thread *t0;
214
215 begin_f_loop(f,t)
216   {
217     t0 = THREAD_T0(t);
218     c0 = F_C0(f,t);
219     F_PROFILE(f,t,i) = 2.0*alpha(c0,t0)*C_Kt(c0,t0)/SQR(
          C_WALL_DIST(c0,t0));
```

```
220   }
221 end_f_loop(f,t)
222 } /* end of function */
223
224 /*
      **********************************************************************

225           DEFINE ON DEMAND FUNCTIONS
226 **********************************************************************
      */
227
228 DEFINE_ON_DEMAND(check_UDS_UDM)
229 {
230 /*  Domain *d = Get_Domain(1);*/
231   check_uds_udm();
232 }/* end of function */
233
234
235 /*  The thermal field must be computed performing few
      iteration with a model already
236   implemented in Fluent. Then this function is needed to
          initialise all the quantities
237   in order to perform the first iteration. */
238
239 DEFINE_ON_DEMAND(interpolation_energy)
240 {
241 Domain *d = Get_Domain(1);
242 Thread *t;
243 cell_t c;
244 real tau_lt;
245 real term1, term2;
246
247 thread_loop_c(t,d)
248   {
249     if (FLUID_THREAD_P(t))
250     { begin_c_loop(c,t)
251       {
252         C_UDSI(c,t,KT) = C_K(c,t);
253         C_UDSI(c,t,TDR_KT)=C_D(c,t);
254         C_UDMI(c,t,TAU_U) = tau_u(c,t);
255         C_UDMI(c,t,TAU_T) = tau_t(c,t);
256         C_UDMI(c,t,ALPHA_T) = C_R(c,t)*C_UDMI(c,t,MUt)
              /0.85;
257         if ( NULL != THREAD_STORAGE(t,SV_T_G) )
258         {   C_UDMI(c,t,P_KT) = C_UDMI(c,t,ALPHA_T) *
              NV_MAG2(C_T_G(c,t)); }
259         else
```

```
260         {
261           Message("\nAllocated temperature gradients!\n"
                 );
262           MD_Alloc_Storage_Vars(d, SV_T_RG, SV_T_G,
                 SV_NULL);
263           C_UDMI(c,t,P_KT) = C_UDMI(c,t,ALPHA_T) *
                 NV_MAG2(C_T_G(c,t));
264
265         }
266           C_UDMI(c,t,PR_T) = C_UDMI(c,t,MUt)/C_R(c,t)/
                 C_UDMI(c,t,ALPHA_T);
267       }
268     end_c_loop(c,t)
269     }
270   } /* end of thread_loop_c */
271
272  Message("\nInterpolation successfully executed\n");
273 } /* end of function */
274
275 /*
    ************************************************************

276 **                          AUXILIARY FUNCTIONS
          **
277 ************************************************************
    */
278
279 void check_uds_udm(void)
280 {
281 /* Check for minimum defined UDS and UDM */
282
283   if (n_uds < N_REQUIRED_UDS || n_udm < N_REQUIRED_UDM)
284   {
285       Message("nERROR: You must define at least %d UDS
             and %d UDM\n", N_REQUIRED_UDS, N_REQUIRED_UDM);
286       Internal_Error("Not enough UDSs defined\n");
287   }
288   else
289   { Message("\nCheck completed succesfully.\nEnough UDS
       and/or UDM allocated!\n"); }
290
291 } /* end of check_uds_udm */
```

List of Figures

List of Tables

Listings

Acronyms

CSP Concetrating Solar Power

HTF Heat Transfer Fluid

It is the fluid used to transfer heat. In this context it transfers the heat produced concetrating the solar power from the receiver to the power block or the thermal storage system.

WF Working Fluid

It is the fluid used in the power block. It goes through the thermodynamic cycle.

TSF Thermal Storage Fluid

It is the fluid used in the thermal storage system.

LCOE Levelised Cost of Energy

It is an economic indicator representing the price of electricity required for a project where revenues would equal costs, including making a return on the capital invested equal to the discount rate. Power plants using new renewable technologies are competitive with traditional ones only when their LCOE are comparable.

USC Ultrasupercritical Steam Cycles

It is a Rankine thermodynamic cycle operating at supercritical pressure.

LBE Lead-Bismut (Pb- Bi) Eutectic

It is an alloy of lead composed by $44.5wt.\%$ Pb + $55.5wt.\%$ Bi.

Hitec Trade name of a ternary molten salt

It is a ternary molten salt composed by $53\%\, KNO_3$, $40\%\, NaNO_2$, $7\%\, NaNO_3$.

SOMMER SOlar Molten MEtal Receiver

Experimental facility at Karlsruhe Institute of Technology.

KALLA KArlsruhe Liquid Metal Laboratory

Team researching liquid metals heat transfer potentialities at IKET.

IKET Institute for Nuclear and Energy Technologies

Department at KIT.

KIT Karlsruhe Institute of Technology

UDF User Defined Functions

It is a C function that can be dynamically loaded with the ANSYS FLUENT solver to enhance its standard features.

RANS Reynolds Averaged Navier Stokes

This acronym is used to identify the time averaged form of the conservation equations (see Eq. 2.16, 2.17, 2.18)

AKN Abe Kondoh Nagano

K. Abe, T. Kondoh and Y. Nagano are the authors of the AKN turbulence model (Ref. [22], [28])

DNS Direct Numerical Simulation

is a simulation in computational fluid dynamics in which the conservation equations are numerically solved without any turbulence model. This means that the whole range of spatial and temporal scales of the turbulence must be resolved.

CFD Computational Fluid Dynamic

Bibliography

[1] O. Behar, A. Khellaf, and K. Mohammedi. "A review of studies on central receiver solar thermal power plants". In: *Renewable and Sustainable Energy Reviews* 23 (2013), pp. 12 –39 (cit. on pp. vii, x, 2–4).

[2] IRENA Secretariat, ed. *Concetrating Solar Power*. Renewable Energy Technologies: Cost Analysis Series. International Renewable Energy Agency (IRENA), 2012 (cit. on pp. vii, x, 2–4, 6).

[3] N. Boerema et al. "Liquid sodium versus Hitec as a heat transfer fluid in solar thermal central receiver systems". In: *Solar Energy* 86 (2012), pp. 2293 –2305 (cit. on pp. vii, x).

[4] J. Pacio et al. "Liquid metals as efficient coolant for high-intensity point-focus receivers: implications to the design and performance of next generation CSP systems". In: *Energy Procedia* 49 (2014), pp. 647 –655 (cit. on pp. vii, x, 4, 7).

[5] J. Flesch et al. "Construction of a test facility for demonstration of a liquid lead-bismuth-cooled 10kW thermal receiver in a solar furnace arrangement - SOMMER". In: *Energy Procedia* 69 (2015) (cit. on pp. vii, x, 7).

[6] W. C. Reynolds. "Turbulent heat transfer in a circular tube with variable circumferential heat flux". In: *International Journal of Heat and Mass Transfer* 6 (1963), pp. 445–454 (cit. on pp. vii, xi, 8, 44–47, 49, 71).

[7] D. Gärtner, K. Johannsen, and H. Ramm. "Turbulent heat transfer in a circular tube with circumferentially varying thermal boundary conditions". In: *International Journal of Heat and Mass Transfer* 17 (1974), pp. 1003–1018 (cit. on pp. vii, xi, 8, 44–49, 71).

[8] S. Manservisi and F. Menghini. "A CFD four parameter heat transfer turbulence model for engineering applications in heavy liquid metals". In: *International Journal of Heat and Mass Transfer* 69 (2014), pp. 312 –326 (cit. on pp. vii, ix, xi, 22, 27, 29, 40).

[9] C. Singer et al. "Assessment of Solar Power Tower Driven Ultrasupercritical Steam Cycles Applying Tubular Central Receivers With Varied Heat Transfer Media". In: *Solar Energy Engineering* 132 (2010) (cit. on pp. x, 4, 7).

[10] Giampaolo Manzolini and Paolo Silva. "Solar Energy Sciences and Engineering Applications". In: ed. by Napoleon Enteria and Aliakbar Akbarzadeh. CRC Press, 2013. Chap. 14, pp. 413–485 (cit. on p. 2).

[11] J. Pacio and Th. Wetzel. "Assessment of liquid metal technology status and research paths for their use as efficient heat transfer fluids in solar central receiver systems". In: *Solar Energy* 93 (2013), pp. 11 –22 (cit. on pp. 4, 7).

[12] J. Pacio et al. “Thermodynamic evaluation of liquid metals as heat transfer fluids in concentrated solar power plants”. In: *Applied Thermal Engineering* 60 (2013), pp. 295 –302 (cit. on pp. 4, 7).

[13] Paul Kesselring and Clifford Selvage. *The IEA/SSPS Solar Thermal Power Plants — Facts and Figures — Final Report of the International Test and Evaluation Team (ITET): Volume 1 Central Receiver Systems (CRS)*. Heidelberg: Springer-Verlag, 1986 (cit. on p. 6).

[14] R. Pitz-Paal, J. Dersch, and B. Milow. *ECOSTAR European Concentrated Solar Thermal Road-Mapping, Technical Report*. Tech. rep. German Areospace Center (DLR), 2003 (cit. on p. 7).

[15] Julio Pacio, Luca Marocco, and Thomas Wetzel. “Review of the data and correlations for turbulent forced convective heat transfer of liquid metals in pipes”. In: *International Journal of Heat and Mass Transfer* 51 (2015) (cit. on pp. xi, 8, 42, 61).

[16] Germain Augsburger and Daniel Favrat. “Modelling of the receiver transient flux distribution due to cloud passages on a solar tower thermal power plant”. In: *Solar Energy* 87 (2013), pp. 42 –52 (cit. on pp. 9, 10).

[17] R. Stieglitz. “Low prandtl number thermal hydrualics”. In: *Handbook on Lead-bismth Eutectic Alloy and Lead Properties, Material Compatibility, Thermal-hydraulics and Technologies*. Ed. by NEA Nuclear Energy Agency. OECD Organisation for Economic Co.Operation and Development, 2007. Chap. 10, pp. 399–478 (cit. on p. 12).

[18] G. Grötzbach. “Challenges in low-Prandtl number heat transfer simulation and modeling”. In: *Nuclear Engineering and Design* 264 (2013), pp. 41 –55 (cit. on pp. 16, 17).

[19] M. Duponcheel et al. “Assessment of RANS and improved near-wall modeling for forced convection at low Prandtl numbers based on LES up to $Re_\tau = 2000$”. In: *International Journal of Heat and Mass Transfer* 75 (2014), pp. 470 –482 (cit. on pp. 16, 17, 24, 28).

[20] Stephen B. Pope. *Turbulent Flows*. Cambridge: Cambridge University Press, 2011 (cit. on pp. 16, 21).

[21] William M. Kays. “Turbulent Prandtl Number: Where Are We?” In: *Journal of Heat Transfer* 116 (1994), pp. 284 –295 (cit. on pp. 22, 27, 28).

[22] K. Abe, T. Kondoh, and Y. Nagano. “A new turbulence model for predictiong fluid flow and heat transfer in separating and reattaching flows - I. Flow field calculations”. In: *International Journal of Heat and Mass Transfer* 37 (1994), pp. 139 –151 (cit. on pp. 22, 25, 26, 90).

[23] H. Kawamura et al. “DNS of turbulent heat transfer in channel flow with low to medium-high Prandtl number fluids”. In: *International Journal of Heat and Fluid Flow* 19 (1998), pp. 482 –491 (cit. on pp. 23, 24).

[24] H. Kawamura, H. Abe, and Y. Matsuo. "DNS of turbulent heat transfer in channel flow with respect to reynolds and Prandtl number effects". In: *International Journal of Heat and Fluid Flow* 20 (1999), pp. 196 –207 (cit. on pp. 23, 24, 37–39, 41).

[25] ANSYS. *Fluent Manual v.15*. 2014 (cit. on pp. 26, 32, 34).

[26] Xu Cheng and Nam-il Tak. "Investigation on turbulent heat transfer to lead–bismuth eutectic flows in circular tubes for nuclear applications". In: *Nuclear Engineering and Design* 236 (2006), pp. 385 –393 (cit. on p. 27).

[27] V. Yakhot, S. A. Orszag, and A. Yakhot. "Heat trasfer in turbulent fluids-I. Pipe flow". In: *International Journal of Heat and Mass Transfer* 30 (1987), pp. 15 –22 (cit. on p. 28).

[28] K. Abe, T. Kondoh, and Y. Nagano. "A new turbulence model for predictiong fluid flow and heat transfer in separating and reattaching flows - II. Thermal field calculations". In: *International Journal of Heat and Mass Transfer* 38 (1995), pp. 1467–1481 (cit. on pp. 29, 90).

[29] Y. Nagano and M. Shimada. "Development of a two-equation heat transfer model based on direct simulations of turbulent flows with different Prandtl numbers". In: *Physics of Fluids* 8 (1996), pp. 3379 –3402 (cit. on p. 29).

[30] John H. V Lienhard and IV Lienhard John H. *A Heat Transfer Textbook IV Edition*. Mineola, New York: Dover Publications, Inc, 2011 (cit. on pp. 31, 32).

[31] J. Ferziger and M. Peric. *Computational methods for fluid dynamics*. Berlin Heidelberg: Springer, 2001 (cit. on p. 34).

[32] NASA Ames Research center. *The design and application of upwind schemes on unstructured meshes*. technical Report 89-0366. Moffet Field, CA, United States: AIAA PAPER, 1989 (cit. on p. 34).

[33] NASA Ames Research center. *A Numerical Study of the Turbulent Flow Past an Isolated Airfoil With Trailing Edge Separation*. technical Report 82-0998. Moffet Field, CA, United States: AIAA PAPER, 1982 (cit. on p. 34).

[34] L. Redjem-Saad, M. Ould-Rouiss, and G. Lauriat. "Direct numerical simulation of turbulent heat transfer in pipe flows: Effect of Prandtl number". In: *International Journal of Heat and Fluid Flow* 28 (2007), pp. 847 –861 (cit. on pp. 37, 40, 42).

[35] E. Skupinski, J. Tortel, and L. Vautrey. "Determination des coefficients de convection d'un alliage sodium-potassium dans un tube circulaire". In: *International Journal of Heat and Mass Transfer* 8 (1965), pp. 937–951 (cit. on pp. 42, 43).

[36] A. Black and E. Sparrow. "Experiments on turbulent heat transfer in a tube with circumferentially varying thermal boundary conditions". In: *Journal of Heat Transfer* 89 (1967), pp. 258–268 (cit. on p. 44).

[37] C. Chang, X. Li, and Q. Zhang. "Experimental and numerical study of the heat transfer characteristics in solar thermal absorbertubes with circumferentially non-uniform heat flux". In: *Proceedings of the SolarPACES 2013 International Conference*. 49. 2014, pp. 305–313 (cit. on p. 44).

[38] X. Yang et al. "Numerical simulation study on the heat transfer characteristics of the tube receiver of the solar thermal power tower". In: *Energy Solutions for a Sustainable World, Special Issue of International Conference of Applied Energy*. 90. 2012, pp. 142–147 (cit. on p. 44).

[39] S. Kakac, R. K. Shah, and W. Aung, eds. *Handbook of single-phase convective heat transfer*. John Wiley & Sons, Inc, 1987 (cit. on pp. 46, 61).

[40] W. Hall and P. Price. "The effect of a longitudinally varying heat flux on the heat transfer coefficient for turbulent flow in a pipe". In: *International Heat Transfer Conference*. 1961 (cit. on p. 61).

[41] I. Celik et al. "Procedure for estimation and reporting of uncertainty due to discretization in CFD applications". In: *Journal of Fluids Engineering* 130 (7) (2008) (cit. on pp. 69, 70).